A study of the spatio-temporal behaviour of bed load transport rate fluctuations

THÈSE N^{O} 6256 (2014)

PRÉSENTÉE LE 10 OCTOBRE 2014

LA FACULTÉ DE L'ENVIRONNEMENT NATUREL, ARCHITECTURAL ET CONSTRUIT
LABORATOIRE D'HYDRAULIQUE ENVIRONNEMENTALE
PROGRAMME DOCTORAL EN MÉCANIQUE

ÉCOLE POLYTECHNIQUE FÉDÉRALE DE LAUSANNE

POUR L'OBTENTION DU GRADE DE DOCTEUR ÈS SCIENCES

PAR

Joris HEYMAN

acceptée sur proposition du jury:

Prof. F. Gallaire, président du jury
Prof. C. Ancey, directeur de thèse
Prof. F. Charru, rapporteur
Prof. A. C. Davison, rapporteur
Prof. A. Radice, rapporteur

ÉCOLE POLYTECHNIQUE
FÉDÉRALE DE LAUSANNE

Suisse
2014

“La science ne se produit pas de façon plus scientifique que la technique de manière technique, que l’organisation de manière organisée ou l’économie de manière économique. ”
—*Nous n’avons jamais été modernes*, Bruno Latour

“denn nicht wollt ihr mit feiger Hand einem Faden nachtasten ;
und, wo ihr erraten könnt, da hasst ihr es, zu erschliessen.”

"car vous ne voulez pas tâtonner d’une main lâche à la recherche d’un fil :
et là où vous pouvez deviner, vous avez horreur de déduire"
—*also sprach Zarathustra*, Friedrisch Nietzsche

À *mon* famille, ces gros cailloux sur qui je peux toujours compter.

Remerciements

Faire une thèse sur les “Rolling Stones” est une entreprise bien étrange, qui peut paraître un peu absurde au premier abord. Au fond, elle l’est sûrement un peu. Néanmoins, à l’aire de la rentabilité sauvage, du rendement spéculatif, du terrorisme d’état et de la consommation de masse, il est assez relaxant de compter les petits cailloux qui roulent dans les rivières.

Mais faire une thèse, c’est aussi long et dur, surtout vers la fin. Je remercie donc tous ceux qui m’ont soutenu, de près ou de loin, pendant ces quatre années.

Je remercie tout d’abord mon directeur de thèse, le professeur Christophe Ancey, pour m’avoir donné la possibilité et les moyens de travailler dans son laboratoire ainsi que pour la liberté et la confiance qu’il m’a accordé. Son expertise scientifique fût d’une grande aide tout au long de ma thèse.

Je remercie tous mes camarades de travail, collègues de jour, et/ou amis de la nuit. Nicolas et Gaël, vieux sages et modèles de vie, toujours prompt à refaire le monde à Satellite. François, fidèle compagnon des virées au Zélig et initiateur hors pair aux joies de la peau de phoque. HongBo, le plus simpa de tout les chinois, sans qui ce travail aurait une tout autre couleur. Belinda, qui célèbre l’anniversaire de la Reine environ trois fois par semaine. Blaise, copain des dernières heures, à qui je souhaite bien du courage. Kasper pour sa générosité naissante. Bob, avec qui travailler fût toujours un plaisir. Barbara, toujours gentille et attentive à nos petits bobos. Le génial professeur Blanckaert, pour ses corrections mais surtout pour sa joie de vivre, son énergie communicatrice et sa jeunesse d’esprit.

Enfin et surtout, je remercie mes 3 collocs, mes 158 amis que j’aime même sans Facebook et ma famille, à qui je dois tout. La conclusion de cette thèse pourrait tout compte fait se résumer ainsi : “Tout ce qui compte, dans la vie comme dans les rivières, ce sont les gros cailloux ! ”. Alors, à tout mes gros cailloux : merci pour tout, et roulez aussi loin que vous le pouvez !

Lausanne, le 2 Juillet 2014, J. H.

Abstract

This thesis addresses the problem of a statistical description of the transport of sediment as bed load. It highlights the role of fluctuations arising during the transport process, and their impact on macroscopic averages. The results presented here are based on four experimental studies. Two of them were published recently by Böhm *et al.* [2004] and Roseberry *et al.* [2012] while the other two were carried out during the thesis. In particular, two high speed cameras were used to automatically reconstruct particle trajectories over a window of approximately 1 m length, continuously over a few minutes. This constitutes, at the time of writing, one of the largest sets of experimental particle trajectory data available.

Based on these experiments, two probabilistic models are proposed. The first one offers a macroscopic picture of the fluctuations of particle activity (concentration of moving particles). Based on a model recently proposed by Ancey *et al.* [2008], it allows for the accurate prediction of the fluctuations observed in the bed load flux. A new formula for the probability density function of the volume-averaged bed load flux is derived and compared to experimental data as well as to existing theory. By slightly modifying the original model, it was also possible to derive the probability density function of the inter-arrival time of particles. The latter shows an unusual bimodal shape due to the effect of collective entrainment. This phenomenon is referred to as the "separation of time scales" [Heyman *et al.*, 2013].

Although providing an accurate picture of the macroscopic fluctuations arising in bed load transport, the first model does not gather information about the spatial behaviour of the bed load flux fluctuations. To remedy this, a new probabilistic model, able to locally describe the transport process, is proposed. This model lies in-between a kinetic description of the transport process and the macroscopic model proposed by Ancey *et al.* [2008]. In this regard, only the particle positions are treated as random variables, while particle velocities are assumed to be close to the Maxwellian equilibrium distribution.

By a careful analysis of first and second moments, in both spatial and temporal dimensions, I prove the occurrence of large correlated structures that strongly perturb the average equilibrium, while not fundamentally modifying it. Moreover, I show that the validity of Taylor's frozen flow hypothesis for bed load transport is severely called into question by the experimental data, proving the peculiar behaviour of those structures during transport by the mean

fluid flow.
Finally, a discussion about scales of fluctuations is provided. It follows from experimental results, as well as from theoretical predictions, that local fluctuations may play an important role in both an experimental setup and natural rivers. Indeed, the saturation and the correlation lengths are often so large that fluctuations may interact in a non-trivial way with the boundaries of the system, precluding the use of macroscopic average equations. Finally, this thesis suggests that the inherent fluctuations of bed load transport rates may need to be taken into account in numerical simulations in order to accurately describe the transport process.

Keywords: bed load, fluctuations, sediment transport, stochastic models.

Résumé

Cette thèse a pour objet la description statistique du transport solide par charriage. Plus précisément, elle s'intéresse au rôle qu'ont les fluctuations dans le processus de transport, ainsi qu'à leur impact sur les équations moyennées. Les résultats présentés dans cette thèse reposent sur quatre études expérimentales. Deux d'entre elles ont été récemment publiées par Böhm *et al.* [2004] et Roseberry *et al.* [2012], tandis que les deux autres ont été conçues spécialement lors de cette thèse. En outre, deux caméras ultra rapides ont été utilisées afin de reconstituer de façon automatique les trajectoires de particules solides sur une longueur totale d'environ un mètre, durant des périodes de quelques minutes.

Grâce aux observations expérimentales, deux modèles probabilistes sont présentés. Le premier est une caractérisation macroscopique de l'activité solide, ou concentration de particules en mouvement. Basé sur un modèle récemment proposé par Ancey *et al.* [2008], il permet de caractériser précisément les fluctuations du débit solide. En outre, la densité de probabilité du débit solide est obtenue analytiquement à partir du modèle et est comparée aux résultats expérimentaux ainsi qu'à d'autres formules existantes dans la littérature. Grâce à une modification du modèle original, la densité de probabilité du temps d'arrivée des particules a aussi pu être obtenue de façon analytique. La forme de celle-ci présente deux modes distincts, dus à l'entraînement collectif des particules. Ce phénomène a été dénommé "séparation des échelles temporelles". Bien que les fluctuations macroscopiques soient correctement représentées par le modèle, ce dernier ne donne aucune information sur leur répartition dans l'espace.

De fait, un nouveau modèle probabiliste, capable de décrire localement le processus de transport est proposé. Ce modèle se situe entre une description cinétique complète du processus de transport et l'approche macroscopique proposée par Ancey *et al.* [2008]. En effet, seules les positions des particules sont considérées dans le modèle comme des variables aléatoires. Au contraire, les vitesses des particules, qui, bien que fluctuantes, sont considérées proches de l'équilibre Maxwellien, et donc indépendantes de leurs positions.

Par une analyse détaillée des moments spatio-temporels de premier et second ordres, il est démontré que des structures cohérentes se développent et perturbent l'équilibre macroscopique, sans toutefois le modifier. L'hypothèse de "frozen flow" proposée par Taylor est testée sur la

base du modèle, mais sa validité dans le cas du transport solide par charriage est sérieusement mise en question par les résultats expérimentaux, prouvant le caractère particulier du transport des structures cohérentes.
En dernier lieu, les échelles spatiales et temporelles sur lesquelles les fluctuations se produisent sont discutées. Les résultats expérimentaux, ainsi que les prédictions théoriques s'accordent à dire que les fluctuations locales peuvent avoir un rôle important, tant à l'échelle du laboratoire qu'à celle de la rivière. En effet, les longueurs de saturation et de corrélation sont souvent si grandes que les fluctuations doivent probablement interagir de manière complexe avec les conditions aux limites du système. Pour conclure, cette thèse prouve que les fluctuations inhérentes au transport solide par charriage doivent être prises en compte dans la modélisation numérique pour une description précise du phénomène.

Mots clefs : charriage, fluctuations, modèles stochastiques, transport de sédiment.

Contents

Remerciements **v**

Abstract (English/Français) **vii**

List of figures **xiii**

List of tables **xvi**

Glossary **xx**

Nomenclature **xxiii**

I Introduction **1**

1 Context 1
2 Motivation 3
3 Thesis contributions and layout 4

II State of the art **7**

1 Hundred years of research 7
2 Definition(s) of bed load flux 9
3 Erosion, transport and deposition 12
3.1 Particle entrainment 12
3.2 Particle transport 14
3.3 Particle deposition 15
3.4 Birth-death Markov process 15

III Theory **17**

1 Physics of bed load transport 17
2 Ancey *et al.*'s [2008] model 18
2.1 Physical space and assumptions 18
2.2 Master equation and steady state behaviour 19
2.3 Recasting the problem into Poisson representation 20

3 Ancey & Heyman's [2014] local model . . . 21
3.1 Particle transport . . . 22
3.2 Master equation . . . 26
3.3 Poisson representation . . . 27
3.4 First moment . . . 29
3.5 Second moments . . . 32
4 Summary . . . 36
4.1 Local model key-points . . . 36
4.2 Model limits . . . 37

IV Experiments **39**
1 Setups . . . 40
1.1 B experiment . . . 40
1.2 R experiment . . . 40
1.3 J experiments . . . 41
1.4 H experiments . . . 43
1.5 Turbulence characteristics and particle dynamics . . . 44
2 Experimental data . . . 45
2.1 Experiments B, R and J . . . 45
2.2 Experiments H . . . 47
2.3 Averages . . . 47
3 Particle transport and deposition . . . 51
3.1 Deposition rate . . . 51
3.2 Particle transport . . . 52
4 Statistics of the bed load flux . . . 55
4.1 Volume average bed load flux . . . 55
4.2 Surface average bed load flux . . . 58
5 Fluctuations of the particle activity . . . 64
5.1 Spatial average . . . 64
5.2 Temporal average . . . 70
6 Summary . . . 73

V Conclusion **75**
1 Summary of results . . . 75
2 Perspectives . . . 77

A Theory **79**
A.1 Poisson representation . . . 79
A.1.1 Principle . . . 79
A.1.2 Derivation of a Fokker–Planck equation for $f(a,t)$ . . . 80
A.1.3 Steady state solution . . . 82
A.1.4 Langevin representation . . . 84
A.1.5 Advantage of the Poisson representation . . . 85

A.2 Link to the BCRE model 86
A.3 Point process 87
A.4 Average behavior 88
A.5 Spatial correlation function 89
A.6 Spatio-temporal correlation function 90
A.7 Equivalence between spatial and temporal correlations at large $\mathscr{P}_e$ 92

B Experiments **95**
B.1 Velocity threshold 95
B.2 An album of particle motions 97
B.3 Derivation of the probability function of the inter-arrival time of particles 104
B.4 Spatial fluctuations of the particle activity 107

Bibliography **116**

Curriculum Vitae **117**

List of Figures

1.1 Sediment transport by bed load 1
1.2 Two pictures of the same river reach taken at a year interval. Navisence river (Switzerland). 3

2.1 Ensemble average procedure of Furbish *et al.* [2012*a*] to get the solid flux through a surface. 11

3.1 Flow configuration. 17
3.2 Configuration of the birth-death model. 19
3.3 Physical space and variables for the local model. 22
3.4 Relaxation of particle activity 30
3.5 Relaxation length and spread of a sediment pulse 31
3.6 Principle of the K-function for a two-dimensional point process. 34
3.7 Contour plot of the spatio-temporal correlation function. 35

4.1 B experiment 41
4.2 Map view of R experiments 42
4.3 J experiments 42
4.4 H experiments 43
4.5 Sample of particle trajectories in the time-space plane (experiment J). 46
4.6 Solid discharge in H experiment 47
4.7 Surface flux 48
4.8 Volume average. 49
4.9 Instantaneous volume average flux through time depending on the volume size Δx. 50
4.10 Estimating the deposition rate σ 52
4.11 Probability density functions of particle velocities 53
4.12 P-P plots for normal and exponentially distributed particle velocities. 53
4.13 Mean squared displacement of particles 54
4.14 Theoretical probability density function of the bed load flux for various parameters. 57

4.15 Probability distribution of the particle flux of experiments J. 59
4.16 Theoretical probability density function (Eq. (4.4.13)) for the waiting time between particle arrivals. 62
4.17 Experimental and theoretical probability density functions of the inter-arrival time of particles for experiments H. 63
4.18 Example of a realization of point positions in a two-dimensional space depending on the value of the dispersion index 65
4.19 Spatial fluctuations of the number of moving particles 66
4.20 Experimental dispersion index 67
4.21 Experimental K-function 68
4.22 Frozen particle flow hypothesis 71
4.23 Comparison with accelerometer data 72
4.24 A summary of the time scales involved. 73

A.1 Time evolution of $f(a,t)$ for $\mu = 0$ (Eq (A.1.14)) 83
A.2 Simulation of the Poisson rate process. 88

B.1 Sensibility to the velocity threshold 96
B.2 Particle trajectories in experiment J5-1. Colours encode velocity (in m/s). 98
B.3 Particle trajectories in experiment J3-1. Colours encode velocity (in m/s). 99
B.4 Particle trajectories in experiment J4-1 (second run). Colours encode velocity (in m/s). 100
B.5 Particle trajectories in experiment J4-1 (fourth run). Colours encode velocity (in m/s). 101
B.6 Particle trajectories in experiment B10-5. Colours encode velocity (in m/s). . . . 102
B.7 Particle trajectories in experiment R0-79. Colours encode velocity (in m/s). . . . 103

List of Tables

4.1 Experimental parameters. 40
4.2 Transport and deposition of particles. 51
4.3 Estimates of the local model parameters 69

Glossary

adiabatic elimination The adiabatic elimination technique consists in removing from a coupled system of equations the variables that evolve a lot faster than the dynamics of interest, in order to simplify the system. 24, 25

birth-death A birth-death Markov process is a discrete-state continuous-time stochastic process where the random variable evolves by unitary jumps of ± 1. It is referred to as "birth-death" since it has extensively been used to study the evolution of living population of bacteria, animals. 5, 16, 19, 21, 22, 25, 60, 87

Euler–Maruyama scheme The Euler–Maruyama scheme is a method for the approximate numerical solution of a stochastic differential equation. It is a simple generalization of the explicit Euler method for ordinary differential equations to stochastic differential equations. 87

Fokker–Planck equation The Fokker–Planck equation is a partial differential equation that describes the time evolution of the probability density function of a random variable. It was named after Adriaan Fokker and Max Planck and is also known as the Kolmogorov forward equation. 23, 25, 27, 28, 80, 82, 84, 85

generating function Probability generating functions are used to transform a discrete space of probabilities into a continuous one. When introduced into a master equation, these functions allow in some cases the exact calculation of the probability density function. 84, 106

Langevin The Langevin equation is a special form of stochastic differential equation named after Paul Langevin, who studied Brownian motion. In this form, the evolution of the stochastic process is separated into two parts: a deterministic evolution term (also called drift) and a noise term. The latter is often represented as increments of a Gaussian noise process $\xi(t)$ or equivalently as the derivative of the Wiener process $\mathrm{d}W(t)$. It is uncorrelated in time, so that it is often referred to as "white noise". 5, 28, 37, 84

likelihood function A likelihood function is a function of the parameters of a statistical model. The likelihood of a set of parameter values of a stochastic model, given experimental outcomes, is equal to the probability (given by the stochastic model) of observing all those outcomes given the choice of parameter values. Likelihood functions play a key role in statistical inference, especially methods of estimating a parameter from a set of statistics. The best set of parameters is found by maximising the likelihood function. 77

Markov process A Markov process is a stochastic process that satisfies the Markov property, also known as the "memoryless" property. Loosely speaking, a process satisfies the Markov property if one can make predictions for the future of the process based solely on its present state, independently of the process past history. 16, 19, 25, 27, 87, 106

master equation A master equation describe the temporal evolution of a probability function. It is in general impossible to solve directly, as it involves discrete and delayed variables. A usual procedure is to transform it into a Fokker–Planck equation, via Van Kampen's expansion. 19, 25, 27, 37, 85, 87

Monte Carlo simulations Monte Carlo simulation methods are a broad class of computational algorithms that rely on repeated random sampling to obtain numerical results when analytical solutions are not known. Typically, computers simulations are run many times over in order to obtain the distribution of the unknown probabilistic entity. They are algorithmically cheap, but computationally expensive. 60, 77

Poisson representation Similar to Laplace or Fourier transform, or even to generating functions, the Poisson representation transforms a discrete probability space into a continuous one by assuming that the discrete random variable can be well represented by a superposition of Poisson distributions whose rates have to be determined. It is used to simplify and solve a master equation. 5, 21, 27–29, 33, 37, 80, 84–87

system-size expansion The system size expansion, also known as van Kampen's expansion, allows one to find an approximate solution of a non-linear master equation by only retaining the leading order term of a linear noise approximation. The system size expansion allows one to obtain an approximate statistical description that can be solved much more easily than the master equation but that relies on the assumption of large system size (e.g.: when the noise is small compared to the average behaviour). 85

Wiener process The Wiener process is a continuous-time stochastic process named in honour of Norbert Wiener. It is also called standard Brownian motion and occurs frequently in pure and applied mathematics, economics, quantitative finance and physics. It is constituted by a sum of random and independent increments, drawn according to the normal distribution. 28, 29, 84

Nomenclature

CONSTANTS

Symbol	Description	Units
$\mathscr{L}$	Measurement length	m
$\mathscr{T}$	Measurement time	s
μ_f	Dynamic fluid viscosity	Pa.s
θ	Mean bed slope	$\circ$
ϱ	Fluid density	kg.m^{-3}
ϱ_s	Particle density	kg.m^{-3}
v_s	Particle mean volume	m^3
B	Flume width	m
d_{50}	Particle mean diameter	m
h	Water Depth	m
k_B	Boltzmann constant	m^2.kg.s^{-2}.K^{-1}
m	Particle mass	kg
v	Depth average flow velocity	m.s^{-1}

FUNCTIONS

Symbol	Description	Units
f	Pseudo density function of the Poisson variable	-
$G(x,t)$	Spatio-temporal correlation function of the particle activity	particles^2.m^{-2}
$g(x,x',t)$	Spatial correlation function of the Poisson activity	particles^2.m^{-2}
$h(x-x')$	Conditional intensity of the point process	particles.m^{-1}
I	Dispersion index	-

$K(x)$	Ripley's K-function	m
y_b	Bed elevation	m

NOTATIONS

Symbol	Description	Units
$\bar{x}$	Spatial or temporal average of the random variable x.	
$\langle \bullet, \bullet \rangle$	Covariance of two random variables. For instance, $\langle X, X \rangle = \langle XX \rangle - \langle X \rangle^2$	
$\langle \bullet \rangle$	Ensemble average.	
$\langle \bullet \rangle_s$	Ensemble average in stationary and homogeneous conditions.	

RANDOM VARIABLES

Symbol	Description	Units
$\beta(x,t)$	Poisson representation of the density of particles in the bed	particles.m^{-1}
$\boldsymbol{a}$	Vector of all a_i.	particles
$\boldsymbol{n}$	Vector of all n_i.	particles
$\eta(x,t)$	Poisson activity	particles.m^{-1}
γ	Particle activity	particles.m^{-1}
a	Poisson rate of the number of moving particle in an observation window.	particles
a_i	Poisson rate of the number of moving particles in cell i.	particles
$b(x,t)$	Density of particles in the bed	particles.m^{-1}
N/n	Random variable/number of moving particles in a observation window	particles
N_i/n_i	Random variable/number of moving particles in the cell i.	particles
q_s	Solid flux	m^3.s^{-1}
u	Particle instantaneous velocity	m.s^{-1}

SCALARS

Symbol	Description	Units
Δx	Length of an observation window/of a lattice cell	m
λ	Entrainment rate	particles.m^{-1}.s^{-1}
ℓ_c	Correlation length	m
ℓ_{sat}	Saturation length	m
$\mathcal{Q}_s$	Cumulative solid flux	m^3

μ	Collective entrainment rate	s^{-1}
$\mathscr{P}_e$	Local Péclet number	-
σ	Deposition rate	s^{-1}
σ_u	Standard deviation of particle velocity	$m.s^{-1}$
$\tilde{L}$	Dimensionless length of an observation window (L/ℓ_c)	-
$\langle u \rangle$	Ensemble average of particle velocities	$m.s^{-1}$
$\bar{u}$	Time average of particle velocities	$m.s^{-1}$
ζ	Viscous drag coefficient	$kg.s^{-1}$
D	Particle diffusivity	$m^2.s^{-1}$
L	Length of an observation window	m
T	Temperature	K
t_λ	Entrainment time scale	s
t_μ	Collective entrainment time scale	s
t_σ	Deposition time	s
t_c	Correlation time in the frozen-flow hypothesis	s
t_r	Velocity relaxation time	s
Pe	Péclet number	-
St	Particle Stokes number	-

I Introduction

1 Context

From the mountains to the seas, the transport of sediment is reshaping the surface of our planet. Grain after grain, stone after stone, the slow but unstoppable work of the wind and water is continually changing the landscape: digging or filling rivers, displacing beaches, moving dunes, covering villages, and demanding the respect of humans.

More discrete and insidious than its cousins, debris flows and avalanches, bed load transport remains nonetheless a vicious child. As its name suggests, "bed load" describes the transport of particles, from sand to boulders, by a fluid running along a granular bed. Particles being fairly heavy, the fluid (air or water) is not able to sustain their motion for long periods as in the case of smaller materials, transported as suspension or wash load. Instead, like a player kicking a ball, the fluid flow intermittently dislodges particles from the bed, forcing them to slide, roll or jump further downstream where they stop again. The particles are thus almost always in contact with the bed, forming a dynamic "load" (Fig. 1.1).

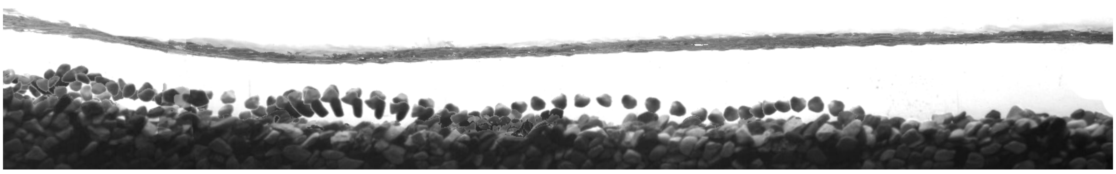

Figure 1.1: Sediment transport by bed load. Frame superposition of an high speed film. Flow is from left to right. Particle size $\simeq 8$ mm.

Bed load is one of the most important actors in sediment transport, but also perhaps one of the least understood. Human activities are directly impacted by bed load, while a lot of economic sectors depend critically on the mastery of sediment transport. For instance, in desert areas, roads and fields are continuously disappearing under sand dunes. In marine environments, harbours and waterways are threatened with sediment accumulation, while famous world heritage sites such as Venezia's lagoon or Mont-Saint-Michel's bay require a miracle not to be buried under sand. Beaches are moving, and with them tourists, rivers are meandering and changing constantly their path, threatening houses.

Switzerland is particularly concerned with bed load transport by water, which each year moves billions of tons of rocks from the high Alpine mountains to the lowland valleys via a connected network of torrents and rivers. Dams, bridges and embankments have major consequences for bed load transport as they locally break up sediment continuity and modify the flow. For instance, it is common to see a net erosion of the river bed behind a dam, because no more sediment is delivered from the upstream valley. Embankments and bridges, for their part, may accelerate or decelerate locally the flow and lead to erosion or deposition respectively. Although the channelling of rivers surely benefited the economic development of valleys in the past, the ecological impacts caused by the modification of the sediment transport process are more uncertain. This is evidenced by the recent projects planned to restore rivers –the Rhône river for instance– to their initial braided patterns.

Although the frequency and strength of heavy sediment transport events has not noticeably changed during the last century in Switzerland, the vulnerability of constructions has dramatically increased. Thus, there is a real need to predict more precisely the regions of potential risk, in the short and long term. This, however, could be realised only if a better picture of the transport process can be drawn. Until now, models predicting bed load transport perform poorly, even at short term. Discrepancies between predictions and observations as large as 3 to 4 orders of magnitude are commonly reported in the literature [Recking *et al.*, 2012]. Meanwhile, bed load transport rates are seen to fluctuate significantly, even under relatively constant flow and bed conditions, calling into question the feasibility of long term sediment budget predictions.

The well known example of atmospheric convection may be worth recalling here. Indeed, it has been shown that some extremely simplified non-linear deterministic systems evolve in such a way that the prediction of their behaviour in the long term is impossible, as an infinitesimal error in the initial conditions will always grow exponentially. This phenomena is known as "deterministic chaos" and conditions atmospheric convection models —one reason why people will never stop complaining about the quality of weather forecasts. Interestingly enough, bed load transport may share some similarities with those systems, first of which is the non-linearity arising from the coupling between the fluid flow and the sediment phase via the erodible bed. In contrast to the well established Navier–Stokes equations for the atmospheric boundary layer, no universal equation exists for sediment transport and mathematical evidence for the presence of "deterministic chaos" in sediment transport systems has not

Figure 1.2: Two pictures of the same river reach taken at a year interval. Navisence river (Switzerland).

been found yet.

The apparent fluctuations of bed load rates in most Swiss rivers suggests the presence of dynamic processes constantly evolving, maintaining the overall system far from a traditional stable equilibrium (Fig. 1.2). The role of noise in such an environment is crucial in driving the system from one state to another. Noise is intrinsically present in sediment transport. First, because bed particles are discrete elements of various shapes, sizes and densities, their motion down the river will be extremely more random than a viscous oil flowing down a plate, for example. Second, noise exists because river flows are highly turbulent, especially in mountain rivers, and flow turbulence has been proved to be a chaotic deterministic system.

2 Motivation

The problem arising in any system subject to noise at the micro-scale is the calculation of consistent average values, or relationships, that can be used to describe its macroscopic behaviour. For instance, for systems in thermodynamic equilibrium, such as inert gas in a box, statistical mechanics tells us that macroscopic variables, such as pressure and temperature, derive from the microscopic random motion of molecules.

Another instructive example can be found in the Reynolds-average Navier-Stokes equations. This set of equations is obtained after decomposing the instantaneous velocity of the flow into a constant and a fluctuating part, $\boldsymbol{u} = \bar{\boldsymbol{u}} + \boldsymbol{u}'$, and averaging the whole equations. The averaged equations reveal an extra contributing factor $\overline{\boldsymbol{u}'_i \boldsymbol{u}'_j}$, called the Reynolds stress tensor. This term typically expresses the fact that fluctuations play a non-negligible role in the macroscopic average, so that they cannot be simply ignored.

In a similar manner, this thesis addresses the possible link between the microscopic stochastic motion of bed load particles under water and macroscopic variables, such as the average bed load flux (see the definition in section 2). In other words, how is individual particle motion reflected through larger scale transport relations? More precisely, how does noise, intrinsically present at small scales, modify the equilibrium and the average macroscopic equations? Until now, the variability of bed load has been deliberately ignored in most bed load transport models. Is this approximation physically justified or, on the contrary, do the macroscopic averaged equations include additional terms similar to Reynolds stresses ?

This thesis aims thus at studying the physics of bed load transport to understand and quantify the fluctuations observed in the solid flux.

3 Thesis contributions and layout

There are two major contributions in this thesis:

1. It pushes forward Böhm *et al.*'s [2004] and Ancey *et al.*'s [2006] studies, as well as Ancey *et al.*'s [2008] stochastic model by highlighting several new applications of the theory. First, various statistics of the bed load flux according to Ancey *et al.*'s [2008] model are derived [Heyman *et al.*, 2013]. Second, we explore the potential applications of [Ancey & Heyman, 2014] stochastic model to characterise spatio-temporal correlation structures in the particle activity. Those structures are shown to span over large scales, suggesting their non-linear interactions with Exner and Saint-Venant equations.
2. The theoretical predictions are supported by a large set of experimental data. Among others, two experiments, denoted by H and J, were carried out to precisely measure the bed load transport process. They show that the proposed model for bed load transport is capable of reproducing many of the features of the fluctuations of transport rates. Notably, the scale dependence of fluctuations is well reproduced by the generalized model of Ancey & Heyman [2014].

Theoretically, the approach adopted in this thesis is the one adopted by Ancey *et al.* [2008], that is, the use of Markov processes to model the random motion of bed load particles. This framework allows to predict the behaviour of the temporal and spatial evolution of the solid flux based on microscopic particle motions. Experimentally, this thesis provides high quality data, in an amount sufficient to obtain unbiased statistical results. Modern signal processing techniques as well as cutting-edge image analysis techniques, borrowed from computer vision science, were used to automatized the treatment of raw experimental data.

This thesis is divided in three main chapters. In the first chapter, I review some of the existing bed load transport models by focusing particularly on contributions to the stochastic framework. Being the corner-stone of any sediment transport theory, the definitions of the solid flux found in the literature are then reviewed in a critical way. Finally, the literature about the physics of the entrainment, the deposition and the transport of bed load particles is reviewed.

The second chapter is dedicated to theoretical developments. I first review the birth-death Markov model of particle exchanges proposed by Ancey *et al.* [2008]. Then, I present Ancey & Heyman's [2014] extension of the latter model to a spatial dimension: after deriving the master equation that governs moving particles locally, a transformation called Poisson representation is used to obtain a Langevin-like [1] stochastic partial differential equation. First and second moments of this equation are analytically derived for some simple cases.

The third chapter is entirely dedicated to experimental comparisons. After presenting the various experiments, the processing techniques as well as the averaging methods, I compare some of the theoretical predictions of Ancey *et al.*'s [2008] model to experimental data. Then, I compare the spatial and the temporal behaviour of the fluctuations of particle activity predicted by the generalized model of Ancey & Heyman [2014] with experimental data. Finally, by comparing spatial and temporal fluctuations of the particle activity, I test the validity of the frozen flow hypothesis in the case of bed load transport.

Finally, I conclude this thesis with a discussion about the importance of taking into account fluctuations of the concentration of moving particles while modelling bed load transport.

1. Most of the stochastic terms used are defined in the glossary, at the beginning of the thesis.

II State of the art

1 Hundred years of research

The sediment transport problem aimed originally at estimating the quantity of solid matter that can be transported by a fluid flow, depending on the strength of the latter.

In the late XIX-th century, du Boys [du Boys, 1879] proposed the first modern formula relating solid flux q_s (see possible definitions in section 2) to the flow shear stress τ [1] acting on the bed as well as the critical shear stress τ_c needed for sediment to start moving. On the basis of this early attempt, several empirical or semi-empirical relationships have been proposed. Surprisingly enough, they often share the same form as the original Du Boy's equation. Among others, the empirical formula of Meyer-Peter & Muller [1948], dating from 1948, is still largely used today by engineers:

$$q_s \propto \sqrt{\tau}(\tau - \tau_c), \tag{2.1.1}$$

A review of the applicability of such formula and the experimental studies that support them is given in Graf [1971].

Apart from such empirical work, a few studies have also succeeded in describing the sediment transport process with the help of physically based arguments. Shields [1936], for instance, recognized in the different variables playing a role in the transport process, that the flow shear

1. In open-channel flow in homogeneous steady conditions, $\tau = \varrho g h \sin\theta$, with ϱ the water density, g the gravity acceleration, h the water depth and θ the bed slope. More generally, $\tau = \varrho (v^*)^2$, where v^* is the shear flow velocity.

stress could be non-dimensionalized with respect to gravity, sediment density and diameter [2]. The "Shields" stress has become today a quantity of reference.

A pioneer in the physics of granular media, from suspension, saltation in air, to bed load transport in water, can be found in the personality of Ralph A. Bagnold. Bagnold was originally a commander of the British Army's Long Range Desert Group during World War II and he published a substantial amount of experimental and theoretical work on sediment transport. By assuming the equilibrium between stream power and bed load layer dissipation, he provided physically based arguments for the dependence of solid flux on shear stress at the power 3/2 [Bagnold, 1956, 1973].

Hans A. Einstein, the first son of Albert Einstein, recognized the intermittent and random behaviour of the transport of bed load particles under water [Ettema & Mutel, 2004]. In 1937, he proposed a probabilistic framework that described the random motion of bed load particles [Einstein, 1937]. His subsequent research, ingeniously relating flow turbulence and sediment load, lead to a statistically based formula [Einstein, 1950]. The latter relates the dimensionless Shields stress to a dimensionless particle flux, through an integral relationship representing the exceedance probability of the instantaneous flow shear stress above a threshold value. Since then, several stochastic formulas have been proposed based on this concept [Bridge & Bennett, 1992; Cao, 1997; Kleinhans & van Rijn, 2002; Van Prooijen & Winterwerp, 2010].

Since Einstein's effort, some researchers have seen the probabilistic framework as a powerful tool to analyse and describe particle motion. By observing the motion of bedforms, Hamamori [1962] proposed an explicit formula for the density probability of the observed bed load flux. The highest fluctuations were found to reach four times the mean bed load flux. Sun & Donahue [2000] proposed a two-state Markov model suggesting that bed load transport rates would follow a binomial distribution. Parker *et al.* [2000] recast the sediment continuity Exner equation into a stochastic equation by considering an active layer of random height. Wu & Chou [2003] considered the rolling and lifting probabilities of particles in a turbulent stream while Wu & Yang [2004] proposed a stochastic partial transport model for mixed size sediments. On the other hand, Turowski [2010] suggested that the shape of the probability distribution of the bed load flux was a function of the inter-arrival time of particles. More recently, in four companion papers, Furbish *et al.* [2012*a*] provided further insights into particle random motion and its consequences on macroscopic conservation equations (see section 2). They based their theoretical analysis on a large set of experimental particle trajectories.

The common development and migration of bed morphology such as ripples, dunes, antidunes or bars [Best, 2005] in streams subject to bed load transport also calls into question the equilibrium hypothesis between the flow and the sediment phase. Interestingly, the length taken for the sediment phase to adapt to a change in the flow conditions (also called saturation length) has been proven to play a fundamental role in the initial growth of instabilities [An-

2. The dimensionless Shields stress, $\tau_s = \tau/((\varrho - \varrho_s) g d_{50})$, with ϱ and ϱ_s the water and sediment density respectively, g the gravity acceleration and $d_5 0$ the mean sediment diameter

dreotti *et al.*, 2012, 2010; Parker, 1975]. On the other hand, Coleman & Nikora [2011] suggested that the presence of random bed patches reflecting the passage of turbulent events may also be involved in the early bedform development stage. Recent statistical studies of bed load time series over a fully developed dune field also showed non-trivial fractal properties of the bed load rates, suggesting a complex interaction between the fluctuations and the mean driving processes [Singh *et al.*, 2009]. Concerning bed forms, Jerolmack & Mohrig [2005] demonstrated how the development and migration of bed forms may be well described by adding a noise term in the sediment continuity equation. Radice *et al.* [2013] showed that the moving particle concentration was strongly correlated to sweeps events at low transport rates, confirming the observations of Drake *et al.* [1988].

The stochastic framework has two advantages compared to classical sediment transport descriptions: (i) it allows the derivation of macroscopic conservation laws from microscopic considerations and (ii) fluctuations of the variables may also be predicted. The latter is particularly suited for bed load transport rates, which are known to show fluctuations that are often larger than the mean [Ancey *et al.*, 2006; Drake *et al.*, 1988; Hoey, 1992; Kuhnle & Southard, 1988; Singh *et al.*, 2009]. Surprisingly, stochastic approaches remain an exception in the bulk of the literature on bed load transport and are mainly absent from practical engineering applications. Besides the relative mathematical difficulties presupposed by such framework, the principal reason for such an absence may be that the acquisition of highly resolved experimental data, mandatory for any statistical analysis, is a difficult, if not impossible, task in the field as well as in the laboratory. Meanwhile, the bed of a river reach or an experimental flume often evolves so quickly (with the migration of bedform for instance) that the sampling of long time series under steady transport conditions is rarely possible.

An increasing number of experiments use high-speed films of particle motion to study bed load transport. Together with extensive numerical treatment, this data provides ground-breaking precision in the description of sediment particles dynamics [Ancey *et al.*, 2006; Campagnol *et al.*, 2013; Martin *et al.*, 2012; Nikora *et al.*, 2002; Radice *et al.*, 2006; Roseberry *et al.*, 2012]. This may allow to recast the sediment transport problem into a more general physical framework. The cornerstone of such a universal framework is the definition of the solid flux, which is reviewed in the following section.

2 Definition(s) of bed load flux

Detailed reviews of the possible definitions of bed load flux can be found in [Ancey, 2010; Furbish *et al.*, 2012*a*]. The natural definition of the vertically integrated flux on a surface A_0 yields

$$q_s = \int_A \vec{u} \cdot \vec{n} \quad \mathrm{d}A, \qquad [\mathrm{m}^3\mathrm{s}^{-1}] \tag{2.2.1}$$

where A is the portion of surface A_0 occupied by a particle, $\vec{u}$ the velocity vector of that particle and $\vec{n}$ the normal to A_0. Similar definitions involve clipping functions (i.e., a function that equals 1 inside a particle and 0 outside) [Radice *et al.*, 2010]. As pointed out by Furbish *et al.* [2012*a*], this definition is impractical due to the experimental precision it requires to be quantified.

In equilibrium and homogeneous conditions and for particles of equal sizes, the solid flux per unit width through a facet normal to the particle velocity is often expressed as

$$\bar{q}_s = \frac{v_s}{B}\bar{u}\bar{\gamma}, \qquad [\mathrm{m}^2\mathrm{s}^{-1}] \tag{2.2.2}$$

where v_s [m^3] is the volume of a particle, B is the flume width, $\bar{u}$ [m.s^{-1}] is the mean particle velocity and $\bar{\gamma}$ [particles.m^{-1}] is the mean particle activity, or concentration of moving particles per meter length. The upper bar denotes either spatial, temporal averaging, or both. Alternatively, an entrainment form of the solid flux has been popularised by Einstein [1950] and reads

$$\bar{q}_s = \frac{v_s}{B}\bar{\lambda}\bar{L}_j, \qquad [\mathrm{m}^2\mathrm{s}^{-1}] \tag{2.2.3}$$

where $\bar{\lambda}$ [particles.m^{-1}.s^{-1}] is the mean particle entrainment rate per meter length and $\bar{L}_j$ [m] is the mean particle jump length. The equivalence between Eq.(2.2.3) and Eq.(2.2.2) is shown in section 4.1.

As pointed out by several authors [Ancey, 2010; Coleman & Nikora, 2009; Furbish *et al.*, 2012*a*], these two last definitions only hold as a macroscopic average for *continuous* fields. However, bed load transport at low to moderate transport rates is known to be highly intermittent [Cao, 1997; Drake *et al.*, 1988] so that the details of the averaging procedure (temporal or spatial average) may influence the measured flux. A careful analysis of the averaging procedure can reveal additional terms in the macroscopic average (see for instance [Coleman & Nikora, 2009] for the Exner equation).

To avoid these undesired properties of averaging procedures, ensemble averaging [3] has been proposed, notably in the theory of granular suspensions. As pointed out by Herczynski & Pienkowska [1980]: "The main advantage of ensemble averaging (in contrast to volume averaging) is that the operations of differentiation and ensemble averaging commute". For instance, Ancey *et al.* [2008] provided a possible definition of an ensemble average bed load flux. However, the complexity of such a definition of the flux makes it of little use in practice.

Furbish *et al.* [2012*a*] also proposed an ensemble average [4] procedure that leads to a slightly different form of the bed load flux. By considering the joint density function of particle activity

3. Here, ensemble averaging has to be understood in the sense, average over the ensemble of particle phase-space configurations, that is over all couples $(\boldsymbol{x}_i, \boldsymbol{u}_i)$.

4. In that case, ensemble averaging stands for an average over all the possible states of any random variable(s). This is a more general definition found in stochastic textbooks Gillespie [1991].

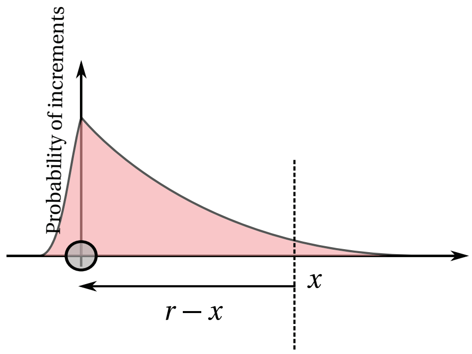

Figure 2.1 – Ensemble average procedure of Furbish *et al.* [2012*a*] to get the solid flux through a surface.

flux. However, the complexity of such a definition of the flux makes it of little use in practice.

Furbish *et al.* [2012*a*] also proposed an ensemble average [4] procedure that leads to a slightly different form of the bed load flux. By considering the joint density function of particle activity (γ) and the particle position increments inside a given region of bed area $\mathrm{d}B$ and during a small time interval $\mathrm{d}t$, they derived a master equation describing the solid volume passing through a point x during $\mathrm{d}t$. By expanding it by powers of $x-r$, the distance to that point (Fig. 2.1), they obtained at first order that the ensemble averaged solid flux is

$$\langle q_s \rangle = \frac{v_s}{B}\left(\langle \gamma u \rangle + \frac{\partial}{\partial x}\langle \kappa \gamma \rangle\right), \qquad [\mathrm{m^2 s^{-1}}] \tag{2.2.4}$$

where κ [$\mathrm{m^2.s^{-1}}$] is a diffusivity constant. The notation $\langle \bullet \rangle$ denotes ensemble average. The ensemble average flux (2.2.4), in contrast to Eq. (2.2.2) includes a diffusive term that is positive when particle activity is varying through space.

Despite being a powerful theoretical tool, ensemble averaging is of little help for experimentalists, doomed to measure only spatial or temporal averages. Meanwhile, there is an issue in determining the required experimental time and space resolution of measurements in order to obtain unbiased estimates of averages [Bunte & Abt, 2005; Singh *et al.*, 2009]. Ergodicity, defined as the equivalence between time/space average and ensemble average [5], is a seriously questionable assumption in the case of bed load transport and will be carefully

[4] In that case, ensemble averaging stands for an average over all the possible states of any random variable(s). This is a more general definition found in stochastic textbooks Gillespie [1991].

[5] A different but equivalent definition of an ergodic system is its ability, in finite time (or space), to explore all of its possible states [Gillespie, 1991]. This definition clearly relates time (in the exploration process) and the ensemble of all possible states.

3 Erosion, transport and deposition

Most of the formula stating the equilibrium between the flow and the solid flux fail to reproduce the behaviour of sediment transport near the threshold of motion, particularly in steep mountainous streams [Nitsche *et al.*, 2011; Recking *et al.*, 2012]. Notably, the high fluctuations observed may partially originate from temporary disequilibriums between erosion and deposition rates. In this spirit, Lajeunesse *et al.* [2010] described the transport of particles by a turbulent flow based on the erosion/deposition model of Charru [2006]; Charru & Hinch [2006]. Ancey *et al.* [2008] proposed an erosion/deposition model describing the fluctuation of the number of moving particles in an observation window, based upon their observations of a highly simplified particle flow experiment.

The main idea behind those models is that particle motions can be broken down into three independent phases: particle entrainment, particle transport and particle deposition. The physics of those are reviewed below.

3.1 Particle entrainment

The entrainment of a resting particle by a fluid flow has been extensively studied and its random character is now widely accepted [Celik *et al.*, 2010; Detert *et al.*, 2010; Dwivedi *et al.*, 2011; Einstein, 1950; Papanicolaou *et al.*, 2002; Schmeeckle *et al.*, 2007; Valyrakis *et al.*, 2010; Wu & Chou, 2003]. At low to moderate flows, entrainment is a discrete process: a single particle lying at the bed surface is entrained if the forces exerted by the surrounding fluid are sufficiently large to dislodge it. The force impulse —the time integral of the force exerted on the particle— has been proven to be of primary importance for particle entrainment. Celik *et al.* [2010] proposed that entrainment would only occur if the force impulse on a particle exceeded a certain impulse threshold depending on particle diameter and bed packing conditions.

Meanwhile, the mean return time of such an event can be accurately described by extreme value theory. Valyrakis *et al.* [2011] suggests that the survival function of a particle resting at the surface the bed is closely approached by an exponential distribution at low flow rates. The latter is a one-parameter distribution and is characteristic of memoryless (uncorrelated) processes. In other words, the time between entrainment events being exponentially distributed, a particle lying on the bed surface has always the same chance to be entrained, regardless of past flow behaviour.

The inter-arrival time of particle entrainment can thus be fully defined by an average particle entrainment rate λ' [s^{-1}]. Equivalently, an entrainment time scale is defined as $t_{\lambda'} = 1/\lambda'$ [s]. Assuming that the bed surface has a constant density of apparent particles ψ_s [6] [particles/m^2], the average entrainment rate per meter flume length is $\lambda = \lambda' B \psi_s$ [particles.m^{-1}s^{-1}], B being

6. $\psi_s = d^{-2}\pi/4 \sim 0.78 d^{-2}$ [particles/m^2] for a squared packing of sphere of diameter d and $\psi_s = d^{-2}\pi/(2\sqrt{3}) \sim 0.91 d^{-2}$ for a triangular packing.

the flume width. In other words, given a flume reach of Δx meters and during a short time interval Δt, there is a probability $\lambda \Delta x \Delta t \ll 1$ that a single particle is entrained in the reach.

Experiments suggest that the entrainment rate λ is linearly related to flow shear stress beyond a critical threshold [Charru, 2006; Lajeunesse *et al.*, 2010]. λ may also be parametrized as a smooth function of shear stress, tending quickly to zero when the shear stress becomes smaller than the critical stress for incipient motion. Equivalently, the entrainment time scale t_λ becomes infinitely large as the shear stress decreases, so that the sediment transport may be considered "frozen" for observation times smaller than t_λ.

There is evidence that other entrainment mechanisms exist, such as simultaneous entrainment of multiple particles by a coherent flow structure [Dinehart, 1999; Drake *et al.*, 1988], impact and destabilization by moving particles [Heyman *et al.*, 2013; Schmeeckle *et al.*, 2001], or local rearrangements of the granular bed. These mechanisms cannot be strictly described by the entrainment time scale t_λ defined previously, the latter involving particles entrained independently of others. On the contrary, these types of entrainment involve particles that are "collectively" entrained, breaking the assumption of independence. A nice illustration of these phenomena can be seen in the detail of Fig. 4.5, which shows a typical tree-like structure indicating correlation in particle entrainment. Ancey *et al.* [2008] used the term "collective entrainment" to describe them.

Several causes for correlated entrainment of particles can be distinguished in the case of bed load transport occurring under water:

1. The critical angle of stability for grains sheared by a fluid flow is known to be significantly reduced [Loiseleux *et al.*, 2005]. As avalanche precursors might happen below the critical angle of stability [Kiesgen de Richter *et al.*, 2012; Staron *et al.*, 2006], small avalanches, or local rearrangements, triggered by the entrainment of a particle, are likely to occur when the local bed slope is sufficiently steep.

2. When the bed shear stress is close to particle incipient motion, small disturbances may initiate particle motion. This is true for turbulent eddies that locally dislodge particles [Papanicolaou *et al.*, 2002] (see also point 4 below). Fast-moving particles that settle on the bed may also potentially disturb resting particles. Particle momentum grows as d^3 and drag force as d^2 so that beyond a critical diameter, particle-particle interactions should become more important than flow-particle interactions. As steep slope streams generally convey large particles, particle-particle interactions may be an important mode of entrainment.

3. The dynamics of impacts has a strong importance in the transmission of momentum from moving particles to the bed [Schmeeckle *et al.*, 2007]. During an impact involving one moving particle and one resting bed particle, the viscous fluid trapped between the two particles strongly damps the contact and dissipates most of the momentum. The coefficient of restitution (the ratio of momentum effectively transmitted) is known to be

a function of the particle Stokes number at impact [7] which compares particle inertia to viscous forces induced by the fluid drainage [Joseph *et al.*, 2001; Legendre *et al.*, 2005]: for St$< 10^1$, the impact is completely damped (the restitution coefficient is null) while for St$> 10^2$ the coefficient of restitution is greater than 0.8. Thus, in air, for sand particles (d$\sim$ 1mm) of moderate velocities 0.5m/s, St$\sim 10^5$. In water, for similar sand particles moving at an intermediate velocity $\langle u \rangle = 0.05$m/s (experiment R), St$\sim 7 \cdot 10^0$ while for gravel particles comparable to those used in experiment B and J, St$\sim 6 \cdot 10^2$. These values suggest that the momentum transfer during particle collisions can be important even under water. Thus collective entrainment by impact destabilization is likely to occur for large and fast enough particles. It is best apprehended by looking at the trajectories of particles in the time-space plane (Fig. 4.5). The tree-like structures observable are typical of “explosive” chain reactions: a particle starts moving, entrains another, which entrains another, etc.

4. Turbulent eddies are spatially correlated, and thus may dislodge several particles simultaneously, leading to “clouds” of moving particles. Drake *et al.* [1988] described them as "sweep-transport" events, that occur only about 9% of the time but still account for 90% of the cumulative load, highlighting thus their importance.

Ancey *et al.* [2008] suggested that all these mechanisms can be described, as a rough approximation, by a positive feedback effect of moving particles on the entrainment of new particles. As done for the particle entrainment rate, a collective entrainment rate μ [s^{-1}], or equivalently a collective particle time scale as $t_\mu = 1/\mu$ [s] may be defined. t_μ is thus the average time for a moving particle to destabilize and entrain another particle. Equivalently, there is a probability $\mu \Delta t \ll 1$ that a moving particle entrains another one during the small time interval Δt.

It is worth pointing out that the separation of the particle entrainment process into two additive and independent processes (namely entrainment and collective entrainment with rate λ and μ) is only a working hypothesis which is not physically justified. In fact, both processes are hardly differentiable, and are likely to simultaneously play a role in the entrainment of new particles.

3.2 Particle transport

Once in motion, particles are advected by the fluid flow. Starting from rest, an entrained particle accelerates to its maximum velocity. Its velocity will be frequently altered due to repeated impacts on the bed as well as by fluctuations of the turbulent drag. Several cycles of acceleration and deceleration are repetitively observed before a particle stops. Meanwhile, there is evidence that particles undergo diffusion during their motion, so that an initial cloud of moving particles will spread through space over short time periods [Hill *et al.*, 2010; Nikora *et al.*, 2002]. This behaviour is mainly explained by the fluctuations of particle velocities. Re-

7. St$= Re_p \rho_s / (9 \rho_f)$, with $Re_p = \langle u \rangle d_{50} / \nu_f$ the particle Reynolds number and ρ_f the fluid density. Note that some authors also includes the effect of the added mass of fluid moving with the particle.

cent experimental studies suggested that particle velocities follow an exponential distribution [Lajeunesse *et al.*, 2010; Roseberry *et al.*, 2012].

Mechanistic models have been proposed to describe particle saltation and rolling motion [Sekine & Kikkawa, 1992]. Stochastic models were also proposed to take into account the random forces involved during particle transport (collisions, flow drag...), assuming that the evolution of the velocity of a particle follows a Langevin equation [Ancey & Heyman, 2014; Fan *et al.*, 2014; Furbish *et al.*, 2012*b*].

3.3 Particle deposition

After being entrained, a particle is dragged by the flow for a certain time before depositing onto the bed. Deposition occurs when two conditions are met: (i) the particle velocity is not large enough to maintain the motion and (ii) the particle is trapped into a sufficiently deep bed asperity [Quartier *et al.*, 2000; Riguidel *et al.*, 1994]. A myriad of factors can affect the deposition of particles. First, as we will see in the next section, particle velocity is a fluctuating quantity. Second, particles are (in general) not spherical so that the contact dynamics between moving particles and the bed are complex [Schmeeckle *et al.*, 2001]. Third, the bed surface, made of an ensemble of different particle shapes and sizes, is highly irregular so that asperities are randomly distributed on its surface.

In this regard, deposition may also be envisioned as a random process. t_σ [s] is then defined as the mean time taken for a moving particle to deposit. Assuming the deposition process to be memoryless (i.e., a particle has always the same chance to deposit), the deposition time of a single particle is exponentially distributed with mean t_σ. Equivalently, a deposition rate $\sigma = t_\sigma^{-1}$ [s^{-1}] can be defined, such that for each small time interval Δt, a moving particle has a probability $\sigma \Delta t \ll 1$ to deposit.

The mean deposition time may scale on particle settling time, that is

$$t_\sigma \propto \frac{d_{50}}{u_s}, \tag{2.3.1}$$

with u_s the settling velocity of particles, and d_{50} the mean particle diameter [Charru, 2006].

3.4 Birth-death Markov process

To understand the coupled and simultaneous effect of entrainment, transport and deposition of particles, Ancey *et al.* [2008] modelled the temporal evolution of the number of moving particles within a control volume $\mathscr{V}$. The number of moving particles $N(t)$ varies with time as a result of particle exchanges with bed such as deposition and entrainment, as seen previously. Ancey *et al.* [2008] found that $N(t)$ follows a negative Binomial distribution, explaining thus the relatively large fluctuations of $N(t)$ compared to its mean.

As shown by Ancey *et al.*'s [2008] model, birth-death Markov processes are particularly interesting to simply characterize particle dynamics and to derive stochastic equations for the bulk solid phase, based on particle microscopic motions. It is thus the framework adopted in this thesis.

III Theory

1 Physics of bed load transport

Bed load transport occurs on the surface of a granular bed sheared by a fluid. In mountainous areas, sand, gravel and pebbles are transported in mildly sloping torrents by shallow water flows. It is often possible to consider that the river (or equivalently the experimental channel) has an infinite width and is transporting water and sediments in a unique direction (taken to be $\vec{x}$) as shown in Fig. 3.1.

For uni-directional problems, the simplest morphodynamic model that can be envisioned comprises the shallow-water (Saint-Venant) equations for the conservation of mass and

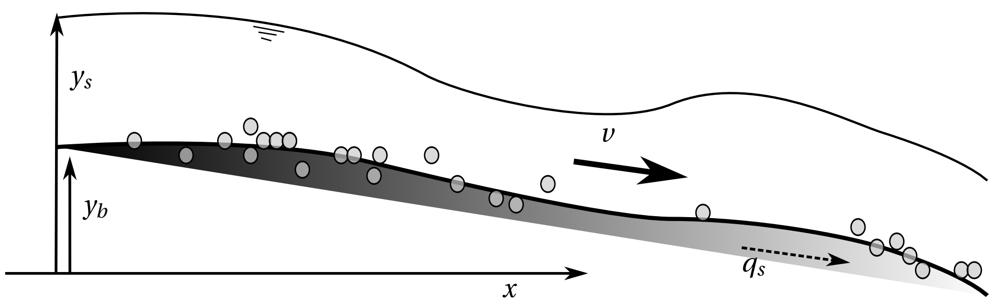

Figure 3.1: Flow configuration.

momentum of the water phase and the Exner equation for the continuity equation of the bed:

$$\frac{\partial h}{\partial t}+\frac{\partial hv}{\partial x} = 0, \tag{3.1.1}$$

$$\frac{\partial hv}{\partial t}+\frac{\partial hv^2}{\partial x}+gh\cos\theta\frac{\partial h}{\partial x} = gh\sin\theta-\frac{\tau}{\varrho}, \tag{3.1.2}$$

$$(1-\zeta_b)\frac{\partial y_b}{\partial t} = -\frac{\partial q_s}{\partial x}=D-E, \tag{3.1.3}$$

in which $h = y_s - y_b$ denotes the flow depth, y_b and y_s the positions of the bed and water surfaces, v the depth-averaged velocity, ϱ the water density, τ is the bottom shear stress, ζ_b the bed porosity, q_s the solid flux, and D and E represent the deposition and entrainment rates. The bed slope is defined as $\tan\theta = \partial_x y_b$. In most models based on (3.1.1)–(3.1.3), the governing equations are closed by empirical relationships for the flow resistance τ [Ferguson, 2007, 2012; Katul *et al.*, 2002; Morvan *et al.*, 2008] and sediment transport rate q_s [Fredsoe, 2012; Graf & Altinakar, 2005], both being functions of the flow variables v and h, and additional parameters (e.g., bed roughness and slope).

The water flow is characterized by its depth-averaged velocity v and flow depth h, which are assumed to be prescribed and independent of the sediment transport. The water flow is turbulent, but the details of the turbulence and velocity field are ignored. Turbulence dissipation and flow resistance due to the particles are entirely encoded in the $\tau_b(v,h)$ expression, which will not be studied here. I only focus on the sedimentary part of the coupled system, that is the evolution of the solid flux q_s (or alternatively, the evolution of the deposition and entrainment rate, D and E respectively). A solution of the coupled system (3.1.1)–(3.1.3) can only be obtained through numerical simulation [Cao *et al.*, 2004; Cordier *et al.*, 2011] and is thus not adequate for analytical results.

2 Ancey *et al.*'s [2008] model

Being the basis of all the results of this thesis, the model of Ancey *et al.* [2008], as well as the principal theoretical results, are briefly reviewed in the following.

2.1 Physical space and assumptions

Ancey *et al.* [2008] modelled the temporal evolution of $N(t)$ moving particles within a control volume $\mathscr{V}$ (Fig. 3.2). The number of moving particles varies with time as a result of particle exchanges with bed such as deposition and entrainment. The volume is taken to be infinitely long, so that fluxes through volume boundaries could be neglected. Thus, in this model, the transport of particles by the flow does not play any role in the variation of N.

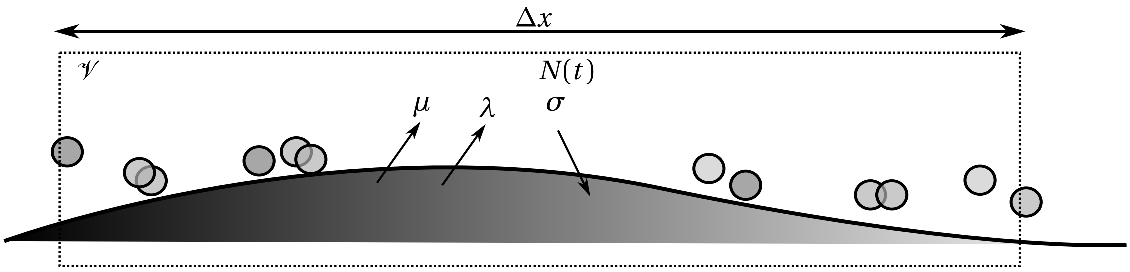

Figure 3.2: Configuration of the birth-death model.

A convenient framework to investigate the statistics of these exchanges is the theory of birth-death Markov processes, widely used in population-dynamics models or chemical kinetics [Gillespie, 1977]. The resulting governing equation is the so-called master equation that describes the time variations of $P(n,t)$, the probability of observing n moving particles within the cell at time t. The model of Ancey *et al.* [2008] belongs to the class of Markov processes with discrete states in continuous time. Indeed, $N(t)$ is an integer-valued random variable as there is a countable number of moving particles in the volume.

2.2 Master equation and steady state behaviour

The exchange probabilities are considered over an infinitesimal time increment Δt, which is assumed to be sufficiently small that at most one exchange occurs in the interval $(t, t+\Delta t)$. The probability of entrainment (birth) is

$$P(n \to n+1, \Delta t) = (\lambda \Delta x + \mu n)\Delta t + o(\Delta t), \tag{3.2.1}$$

with λ the mean entrainment rate per meter length, and μ the collective entrainment rate. The transition probability of deposition is

$$P(n \to n-1, \Delta t) = n\sigma\Delta t + o(\Delta t), \tag{3.2.2}$$

with σ the mean deposition rate.

Given this transition probabilities, Ancey *et al.* [2008] obtained the master equation governing the time evolution of the probability function of $N(t)$,

$$\begin{aligned}
\frac{\partial}{\partial t}P(n,t) &= (n+1)\sigma P(n+1,t) + \big(\lambda\Delta x + (n-1)\mu\big)\,P(n-1,t) && (3.2.3)\\
&\quad - \big(\lambda\Delta x + n(\sigma+\mu)\big)\,P(n,t), \qquad n>0 &&\\
\frac{\partial}{\partial t}P(0,t) &= \sigma P(1,t) - \lambda\Delta x P(0,t). && (3.2.4)
\end{aligned}$$

Using generating functions, Ancey *et al.* [2008] found that the stationary probability function of $N(t)$ is negative Binomial for $\mu > 0$

$$P_s(n) = \mathrm{NegBin}(n; r, p) = \frac{\Gamma(r+n)}{\Gamma(r)n!} p^r (1-p)^n, \qquad n \geq 0, \tag{3.2.5}$$

with parameters $r = \lambda \Delta x/\mu$ and $p = 1 - \mu/\sigma$, and where Γ denotes the gamma function. The mean is

$$\langle N \rangle = \frac{\lambda \Delta x}{\sigma - \mu}, \tag{3.2.6}$$

and the variance is

$$\mathrm{Var}(N) = \frac{\lambda \Delta x \sigma}{(\sigma - \mu)^2}. \tag{3.2.7}$$

For $\mu = 0$, Ancey *et al.* [2008] found that $N(t)$ follows a Poisson distribution of rate $r_p = \lambda \Delta x/\sigma$„

$$P_s(n) = \frac{(r_p)^n}{n!} \mathrm{e}^{-r_p}, \qquad n \geq 0, \tag{3.2.8}$$

with mean and variance equal to $\lambda \Delta x/\sigma$.

Ancey *et al.*'s [2008] model allows thus to model the fluctuations of the erosion and deposition rates E and D, found in the Exner equation (3.1.3), through the fluctuation of $N(t)$:

$$\begin{aligned} E(t) &\simeq \lambda + \mu N(t), \\ D(t) &\simeq \sigma N(t). \end{aligned} \tag{3.2.9}$$

2.3 Recasting the problem into Poisson representation

It is worth noting that despite appearances, the solutions corresponding to the $\mu > 0$ and the $\mu = 0$ cases are connected. Indeed, the negative binomial distribution can be interpreted as a compound probability distribution (e.g., the probability distribution function of a random variable whose parameters are themselves random variables) of a Poisson distributed random variable with a rate a following a gamma distribution

$$P_s(n) = \int_a \frac{e^{-a} a^n}{n!} \mathrm{Ga}(a; \alpha, \beta) \mathrm{d}a = \mathrm{NegBin}(n, r, p) = \frac{\Gamma[r+n]}{\Gamma[r]} p^r (1-p)^n, \tag{3.2.10}$$

with $\alpha = r = \lambda\Delta x/\mu$ and $\beta = 1/p - 1 = \mu/(\sigma - \mu)$. So, interestingly, the Poisson distribution is retrieved even in the case $\mu > 0$, but hidden behind the stochastic variations of its rate a. A physical interpretation can then be put forward. In the absence of collective entrainment ($\mu = 0$), the behaviour is Poissonian with a fixed rate $r_p = a = \lambda\Delta x/\sigma$ dictated by entrainment and deposition of individual particles. When collective entrainment occurs ($\mu > 0$), the behaviour can still be seen as Poissonian, but with a random rate [Ancey *et al.*, 2006]. This random rate follows a gamma distribution, whose parameters are greatly influenced by μ, especially when $\mu \to \sigma$ ($\beta \to \infty$). It is shown in Appendix A.1 that a generalized solution to the forward master equation (3.2.4) can be found in the form of a Poisson representation. This transformation, in a similar manner to Fourier and Laplace transforms or generating functions, greatly simplifies the solutions of birth-death processes.

3 Ancey & Heyman's [2014] local model

Ancey & Heyman [2014] proposed a local description of the sediment transport process, based on Ancey *et al.*'s [2008] model. This local description is recalled in the following section.

A complete local description of the process would require a phase-space description of the bed load particles, so that both position and momentum of individual particles would be regarded as random variables. This is the basis of kinetic theory. However, such a system requires closure equations (for instance a collision operator), which, if tractable in ideal gases or fluids, remain unknown in the case of bed load transport. Alternatively, instead of working in the full phase-space domain, it is often possible to reduce the problem's dimensionality to a simpler "concentration space", where particles are defined uniquely by their positions (and no longer by their momentum). In such a representation, particles are still moving, but their velocities evolve randomly and independently of their position. In the language of statistical mechanics, the particles are supposed to be close to the Maxwellian equilibrium state [Böhm *et al.*, 2004; Nicolis & Prigogine, 1977]. This approximation requires that the relaxation time of particle velocity is much smaller than any other characteristic times (for instance t_σ, t_μ, t_λ, ...).

The physical space is divided into a regular lattice, composed of cells of volume $\Delta\mathscr{V}$. Typically, a cell has a fixed width (the flume width B) and depth (flow depth h) so that the only important length is Δx, the length of the cell parallel to the mean particle flow [1]. Let N_i to denote the random variable of the number of particles in motion in cell i, whose centres are located at x_i (Fig. 3.3). $\boldsymbol{n} = (n_0, n_1, n_2, \ldots, n_m)$ is the vector of the number of moving particles in all cells.

1. In contrast to Ancey *et al.*'s [2008] model, Δx does not need to be large.

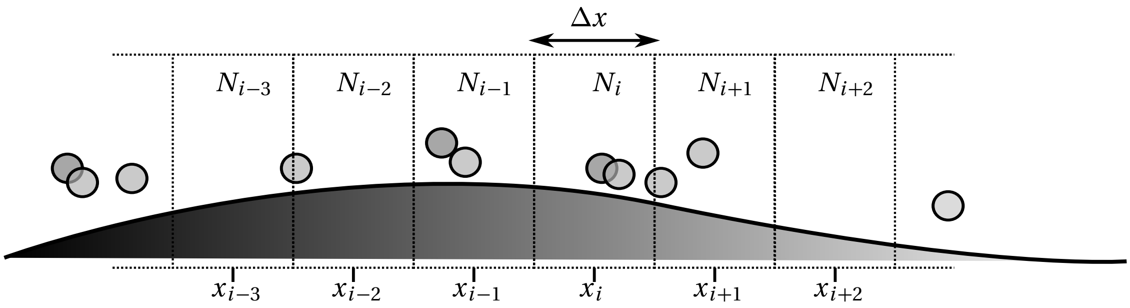

Figure 3.3: Physical space and variables for the local model.

3.1 Particle transport

In this section, we will see how Ancey & Heyman [2014] take into account particle transport in the birth-death formalism.

Mechanistic Langevin equation

The position of a bed load particle during its transport by the flow can be reconstructed with the help of Newton's second law. However, most of the forces acting on a single particles (flow drag, collisions,...) are fluctuating quantities. Thus, it is tempting to compare the motion of a bed load particle to Brownian motion [2] in a potential (also called correlated random walk). In this spirit, the motion of a bed load particle may be described by a Langevin equation in phase-space [Uhlenbeck & Ornstein, 1930]

$$\frac{\mathrm{d}x}{\mathrm{d}t} = u, \tag{3.3.1}$$

$$m\frac{\mathrm{d}u}{\mathrm{d}t} = -\zeta(u-\langle u\rangle)+\sqrt{2k_BT\zeta}\,\xi(t), \tag{3.3.2}$$

where x [m] is the abscissa of the centre of mass of a moving particle, u [m.s^{-1}] denotes its velocity, m [kg] the immersed mass of the particle, ζ [kg.s^{-1}] a (viscous) drag coefficient [3], $\langle u\rangle$ the mean particle velocity, k_B [m^2.kg.s^{-2}.K^{-1}] the Boltzmann constant and T [K] the "temperature" [4] of the medium where the particle evolves. $\xi(t)$ is a white noise term.

In essence, (3.3.2) is nothing but Newton's second law applied to a particle when both a deterministic and a random force exist. The deterministic force is comparable with the mean

2. Keeping in mind that Brownian particles are much smaller than bed load particles so that the microscopic forces involved are certainly different but can still be approximated by similar stochastic laws.

3. The Stokes law for a sphere of diameter d gives $\zeta = 3\pi\mu_f d$, where μ_f [Pa.s] is the dynamic fluid viscosity.

4. Note that in our case, it makes no sense to define a macroscopic "temperature", as the local mixing results from various phenomena such as turbulent diffusion and particle impacts. Thus, k_B and T are only used in analogy with the Brownian motion.

(viscous) flow drag while the random force originates from the frequent impacts on the bed and the fluctuations of turbulent flow drag.

The stochastic equations (3.3.1) and (3.3.2) are equivalent to the Fokker–Planck equation for the (Lagrangian) distribution function of particle position and velocity $P(x,u,t)$:

$$\frac{\partial P}{\partial t} = -\frac{\partial}{\partial x}(uP) + \frac{\partial}{\partial u}\left(\frac{\zeta}{m}(u-\bar{u}_s)P\right) + \frac{\partial^2}{\partial u^2}\left(\frac{k_B T\zeta}{m^2}P\right). \tag{3.3.3}$$

The marginal probability density function of particle velocities P_u in stationary ($t \to \infty$) homogeneous conditions derives straightforwardly from the Fokker–Planck equation (3.3.3):

$$P_u(u, t \to \infty) = \frac{1}{\sigma_u\sqrt{2\pi}}\exp\left(-\frac{(u-\langle u\rangle)^2}{2\sigma_u^2}\right), \tag{3.3.4}$$

where $\sigma_u^2 = k_B T/m$. This is a Gaussian distribution of mean $\langle u\rangle$ and variance σ_u^2, often referred to as Maxwell–Boltzmann distribution. Note that, in this model, nothing precludes u from being negative.

The mean squared displacement (MSD) through time of a particle is a quantity of particular interest, since it can be easily measured experimentally. Uhlenbeck & Ornstein [1930] gave the expression of the MSD for the Brownian motion in a potential (3.3.1)–(3.3.2):

$$\mathrm{MSD} = \left\langle (X(t) - \langle X(t)\rangle)^2 \right\rangle = \frac{2k_B T m}{\zeta^2}\left[e^{-\zeta|t|/m} - 1 + \frac{\zeta|t|}{m}\right]. \tag{3.3.5}$$

At large times, $t \to \infty$, the MSD tends to $2k_B T|t|/\zeta$. This linear dependence in time is the classical scaling of a pure Brownian motion. At small times $t \to 0$, the MSD is proportional to $k_B T t^2/m$. The dependence on t^2 suggests the ballistic limit of particle trajectories at small time scales due to time correlations in particle velocity.

In the limit of large ζ/m, Eq.(3.3.2) should relax rapidly to a quasi-stationary state in which $\mathrm{d}u/\mathrm{d}t \to 0$. In that case, an adiabatic elimination of the fast variable can be achieved and leads to the marginal distribution function for the particle position $P_x(x,t)$ [Gardiner, 2002]:

$$\frac{\partial P_x(x,t)}{\partial t} = -\frac{\partial}{\partial x}(\langle u\rangle P_x(x,t)) + \frac{\partial^2}{\partial x^2}\left(\frac{k_B T}{\zeta}P_x(x,t)\right). \tag{3.3.6}$$

Using the equivalence between the probability density function of particle positions (Lagrangian) and the particle concentration $\gamma(x,t)$ [particles.m^{-1}] (Eulerian)[Gardiner, 2002], the latter follows

$$\frac{\partial \gamma(x,t)}{\partial t} = -\frac{\partial \langle u \rangle \gamma(x,t)}{\partial x} + \frac{\partial^2 D\gamma(x,t)}{\partial x^2}. \tag{3.3.7}$$

Thus, at equilibrium, the motion of a cloud of particles can be approximated by the sum of an advective and a diffusive term. The apparent diffusivity coefficient is $D = k_B T/\zeta = \sigma_u^2 t_r$, where $t_r = \zeta/m$ is the relaxation time of particle velocities.

To summarize, three temporal scales are involved in particle transport: $t_r = m/\zeta$, the relaxation time of particle velocities; $t_a = \Delta x/\langle u \rangle$, an advection time scale; and $t_d = \Delta x^2/D$, a diffusion time scale. Δx is the characteristic length scale of the problem. The adiabatic elimination procedure relies on the assumption that $t_r \ll (t_a, t_d)$. In this limit, the MSD scales linearly with time.

Particle diffusion as a jump process

We saw that, according to the transport model (3.3.2), the time evolution of the probability density function of the position of a moving particle can be broken down, at large time ($t > t_r$), into advection (with velocity $\langle u \rangle$) and diffusive spreading (at rate D).

Advection can be considered to be a purely deterministic process (it only results in a drift term in the Fokker–Planck equation (3.3.3)) and therefore does not cause any stochastic fluctuations. On the contrary, diffusion itself can be locally described by a birth-death Markov process [Ancey & Heyman, 2014]:

$$\begin{aligned} &P(n_i \to n_i - 1, n_{i+1} \to n_{i+1} + 1 | t) = d\, n_i \Delta t + o(\Delta t), \\ &P(n_i \to n_i - 1, n_{i-1} \to n_{i-1} + 1 | t) = d\, n_i \Delta t + o(\Delta t), \end{aligned} \tag{3.3.8}$$

and are associated to the multivariate master equation

$$\frac{\partial}{\partial t} P(\boldsymbol{n}, t) = \sum_i d \left\{ (n_i + 1) \left(P(\boldsymbol{n} + \boldsymbol{r}_i^+ + \boldsymbol{r}_{i+1}^-, t) + P(\boldsymbol{n} + \boldsymbol{r}_i^+ + \boldsymbol{r}_{i-1}^-, t) \right) - 2 n_i P(\boldsymbol{n}, t) \right\}, \tag{3.3.9}$$

where $\boldsymbol{r}_i^{\pm}$ is a vector whose elements are all 0 excepted its i-th value: $r_i = \pm 1$, $r_k = 0$ for $k \neq i$. $P(\boldsymbol{n} + \boldsymbol{r}_i^+ + \boldsymbol{r}_{i-1}^-, t)$ is thus the probability of observing the system in the state $\boldsymbol{n}' = (n_1, n_2, \ldots, n_{i-1} - 1, n_i + 1, n_{i+1}, \ldots)$. The average behaviour is readily obtained from (3.3.9)

[Gillespie, 1991] and reads

$$\frac{\partial \langle N_i \rangle}{\partial t} = d\left(\langle N_{i-1} \rangle + \langle N_{i+1} \rangle - 2\langle N_i \rangle\right). \tag{3.3.10}$$

The particle activity (the concentration in moving particles) is defined by $\langle \gamma(x_i) \rangle = \langle N_i \rangle / \Delta x$ and letting $\Delta x \to 0$, Eq. (3.3.10) transforms to

$$\frac{\partial \langle \gamma \rangle}{\partial t} = D \frac{\partial^2 \langle \gamma \rangle}{\partial x^2}, \tag{3.3.11}$$

with $D = d\Delta x^2$ held constant. Recall that a frame of reference moving at the constant speed $\langle u \rangle$ was used. Thus, in the static frame of reference, $\langle \gamma \rangle$ should follow

$$\frac{\partial \langle \gamma \rangle}{\partial t} - \langle u \rangle \frac{\partial \langle \gamma \rangle}{\partial x} = D \frac{\partial^2 \langle \gamma \rangle}{\partial x^2}. \tag{3.3.12}$$

Note that Eq. (3.3.12) is very close to the limiting behaviour of Eq. (3.3.7). The difference is that D and $\langle u \rangle$ comes up as a weighting parameter of the diffusion term $\partial^2 \langle \gamma \rangle / \partial x^2$ and the advective term $\partial \langle \gamma \rangle / \partial x$ respectively while they act directly on the flux terms in Eq. (3.3.7). In practice, for constant diffusivity D and constant average particle velocity $\langle u \rangle$, Eq. (3.3.12) and Eq. (3.3.7) are equivalent. It is worth noting that the change of referential (a lattice moving at the velocity $\langle u \rangle$) is only valid in the case of a constant average particle velocity. If $\langle u \rangle$ is changing through space and time, this approach cannot be used [5].

The approximation of particle transport as a local jump process at the micro-scale relies on strong simplifying hypothesis. First, the limiting diffusive behaviour supposes that the time scale is sufficiently large for Eq. (3.3.7) to be valid [Othmer *et al.*, 1988]. Indeed, the particle transport process shows some non-vanishing correlation and thus pure diffusion is only observed for $t \gg t_r$, where t_r is the relaxation time of particle velocity. On the contrary, when studying the local jump process on a lattice, the probabilities are considered over infinitesimal time increments. Thus, at these small time scales, the diffusion approximation may not be valid. Second, the local jump process was assumed to have the same rate in both forward and backward directions. This may not be true at small time in the case of an asymmetric distribution of particle velocities [6] Third, diffusive models suffer from the deficiency of the linear heat equation, that is the possibility of infinitely fast propagation of particles [Müller &

5. As particle concentration can be interpreted as a compressible medium, an equation of mass conservation for compressible flows may be more appropriate to describe the transport of particles when their average velocity is changing in time or space.

6. It can be shown that if the second moment of the particle velocities exists, the distribution of the sum of many small particle displacements will always converge to a symmetric Gaussian distribution, leading to a a symmetric jump process at large time. At small time, the shape of the distribution of the particle velocities may have a strong impact on the symmetry of the jump process.

Hillen, 1998].

Several models have been proposed to overcome the limitations created by the diffusion approximation. Those take into account the fact that the transport of a particle is appropriately modelled by a correlated random walk [Goldstein, 1951](in contrast to the pure Brownian motion which is uncorrelated [Einstein, 1906]). Among them, the so called velocity jump process [Müller & Hillen, 1998; Othmer *et al.*, 1988] succeeds in describing the random walk of biological organisms (cells, bacteria...). This process is shown to be governed by a well known linear equation: the telegraph equation. At infinite time, the diffusion limit is retrieved. Inserting reactions (birth and death of particles for instance) into this framework is not obvious and non-linear terms might complicate the equation [Müller & Hillen, 1998].

Though questionable at the micro-scale (for small time intervals), the diffusion approximation will be used in the following. Indeed, together with the Poisson represention (Appendix A.1), the approximation of particle transport as a local jump Markov process allows to study the coupled effects of entrainment, deposition and transport of particles locally. In other words, it is a minimum price to pay to continue the analysis and achieve analytical results.

3.2 Master equation

In their birth-death model, Ancey *et al.* [2008] introduced the probability rates of particle exchanges with the bed, namely the particle mean entrainment rate λ, particle mean collective entrainment rate μ and particle mean deposition rate σ. Together with these exchanges, the local model allows particles to migrate locally from one cell to another with rate d.

In the following, the rate coefficients λ, σ, μ and d are assumed to be constant in space and time. This leads us to focus on fluctuations that originate from the randomness of particle motions rather than fluctuations arising because of local changes in flow or bed slope — which would in turn modify the rate coefficients, when bedforms are present for instance. The transition probabilities of particle exchanges with the bed, as well as the local diffusion process form the elementary rules governing the evolution of a multivariate birth-death Markov process. From these simple rules, a multivariate master equation describing the temporal evolution of $P(\boldsymbol{n}, t)$ can be derived:

$$\begin{aligned}\frac{\partial P(\boldsymbol{n},t)}{\partial t} = \sum_i \quad & d(n_i+1)\left(P(\boldsymbol{n}+\boldsymbol{r}_i^+ + \boldsymbol{r}_{i+1}^-, t) + P(\boldsymbol{n}+\boldsymbol{r}_i^+ + \boldsymbol{r}_{i-1}^-, t)\right) \\ + \quad & (n_i+1)\sigma P(\boldsymbol{n}+\boldsymbol{r}_i^+, t) + \left(\lambda\Delta x + (n_i-1)\mu\right) P(\boldsymbol{n}+\boldsymbol{r}_i^-, t) \\ - \quad & \left(\lambda\Delta x + n_i(\sigma+\mu) + 2d\,n_i\right) P(\boldsymbol{n}, t),\end{aligned} \tag{3.3.13}$$

Unlike (3.2.4), there is no easy way to solve (3.3.13) by generating functions because of the coupling that arises between cells. However, in Appendix A.1, it was shown that the Poisson representation transforms a discrete master equation into a continuous Fokker–Planck equation. Moreover, in the Poisson representation, uni-molecular reactions —entrainment, deposition and diffusion— only result in drift terms in the Fokker–Planck equation [Chaturvedi & Gardiner, 1978; Gardiner & Chaturvedi, 1977]. In the following, the multivariate Poisson representation is thus used to solve (3.3.13).

3.3 Poisson representation

Fokker–Planck equation

The multivariate Poisson representation of an array of discrete random variables $\boldsymbol{n} = (n_1, n_2, \ldots, n_m)$ is defined as:

$$P(\boldsymbol{n}, t) = \prod_i \int_{\mathbb{R}^+} \frac{e^{-a_i} a_i^n}{n!} f(\boldsymbol{a}, t) \mathrm{d}\boldsymbol{a}, \tag{3.3.14}$$

where $\boldsymbol{a} = (a_1, a_2, \ldots, a_m)$ and $f(\boldsymbol{a}, t)$ is a multivariate pseudo-probability density function. Here, in contrast with the univariate case, f is called a pseudo-probability as it cannot be taken for granted that f is positive at any time [Gardiner & Chaturvedi, 1977]. The rules of transformation being the same as those used in Appendix A.1, a governing equation for $f(\boldsymbol{a}, t)$ —$\boldsymbol{a}$ being the vector of all a_i— generalizing (A.1.13) is readily obtained:

$$\frac{\partial}{\partial t} f(\boldsymbol{a}, t) = \sum_i \mu \frac{\partial^2 a_i f}{\partial a_i^2} + \frac{\partial}{\partial a_i} \left\{ \left[d(a_{i+1} + a_{i-1} - 2a_i) + \lambda \Delta x - a_i(\sigma - \mu) \right] f \right\}. \tag{3.3.15}$$

As noted earlier, only the collective entrainment results in a diffusive term in the Fokker–Planck equation for $f(\boldsymbol{a}, t)$.

Langevin stochastic equation

The Langevin form of the stochastic equation equivalent to (3.3.15) is

$$\mathrm{d}a_i(t) = \big(d(a_{i+1} + a_{i-1} - 2a_i) + \lambda \Delta x - a_i(\sigma - \mu) \big) \mathrm{d}t + \sqrt{2\mu a_i}\, \mathrm{d}W_i(t), \tag{3.3.16}$$

which holds for $i = 2, 3 \ldots$ and where $\mathrm{d}W_i$ is the time derivative of a Wiener process for cell i (a white noise). In a similar manner as for Eq. (A.1.24), the noise term of Eq. (3.3.16) is said to be multiplicative since its amplitude is modulated by the random variable a_i.

In a similar way as for the definition of the particle activity $\gamma(x, t)$, let $\eta(x, t)$ denote the Poisson density variable, or Poisson activity:

$$\eta(x_i, t) = a_i(t)/\Delta x. \tag{3.3.17}$$

Using equations (3.3.16)-(3.3.17) and letting $\Delta x \to 0$, the Langevin stochastic partial differential equation in the Poisson density variable is obtained:

$$\mathrm{d}\eta(x,t) = \left[D\nabla^2\eta(x,t) + (\mu - \sigma)\eta(x,t) + \lambda\right]\mathrm{d}t + \sqrt{2\mu\eta(x,t)}\,\mathrm{d}W(x,t), \tag{3.3.18}$$

where $W(x,t)$ is now a spatial Wiener process with the correlation function

$$\mathrm{d}W(x,t)\mathrm{d}W(x',t) = \delta(x - x')\mathrm{d}t.$$

The multiplicative noise term arising in Eq. (3.3.18) is perfectly uncorrelated in time and space.

In a similar manner as in eq. (3.3.12), the local jump process transforms into a diffusion process in the continuum limit of the Poisson representation, with diffusivity $D = d\Delta x^2$.

Thanks to the overall linearity of the deterministic part of Eq. (3.3.18), the deterministic advection flux can be reintroduced in the stochastic equation (3.3.18):

$$\mathrm{d}\eta(x,t) = \left[-\langle u\rangle\nabla\eta(x,t) + D\nabla^2\eta(x,t) - (\sigma - \mu)\eta(x,t) + \lambda\right]\mathrm{d}t + \sqrt{2\mu\eta(x,t)}\,\mathrm{d}W(x,t) \tag{3.3.19}$$

Eq. (3.3.19) thus models the stochastic evolution of the rate (per unit length) of the Poisson distribution followed by $N_i(t)$. It is shown in Appendix A.3 how Eq. (3.3.19) can be solved numerically and how it can be related to the point process framework [Cox & Isham, 1980].

Eq. (3.3.19) also shares interesting similarities with the BCRE model of dry granular avalanches of Bouchaud *et al.* [1995]. In appendix A.2, I show how Eq. (3.3.19) may be used as a stochastic version of the BCRE model in order to characterize spatial correlations in some dry granular flows.

It has been shown in equation (A.1.2) that the p-factorial moment of N equals the p-moment of a. Similar relationships are found between spatial moments of $\eta(x,t)$ and $\gamma(x,t)$:

$$\begin{aligned}\langle \eta(x,t)\rangle &= \langle \gamma(x,t)\rangle \\ \langle \eta(x,t),\eta(x',t)\rangle + \langle \eta(x,t)\rangle\,\delta(x-x') &= \langle \gamma(x,t),\gamma(x',t)\rangle\,,\end{aligned} \tag{3.3.20}$$

where the notation $\langle \bullet,\bullet\rangle$ denotes the covariance of two variables (e.g., $\langle X,X'\rangle = \langle XX'\rangle - \langle X\rangle\langle X'\rangle$).

In the following, the first and second moments of Eq. (3.3.19) are studied.

3.4 First moment

The average behaviour of $\eta(x,t)$ is easily obtained by dropping the noise term in Eq. (3.3.19) and using (3.3.20):

$$\frac{\partial\langle\gamma(x,t)\rangle}{\partial t} - \langle u\rangle\frac{\partial\langle\gamma(x,t)\rangle}{\partial x} = D\frac{\partial^2\langle\gamma(x,t)\rangle}{\partial x^2} + \lambda - (\sigma-\mu)\langle\gamma(x,t)\rangle \tag{3.3.21}$$

It is a linear advection-diffusion-reaction equation. Note that no shocks can develop in (3.3.21), as the diffusive term tends to smooth out high gradients in particle activity and Eq. (3.3.21) remains valid at all times. A stationary ($t\to\infty$) and homogeneous solution can be found providing that $\sigma > \mu$:

$$\langle\gamma\rangle_s = \frac{\lambda}{\sigma-\mu}, \tag{3.3.22}$$

where the notation $\langle\bullet\rangle_s$ denotes ensemble average in stationary and homogeneous conditions. Two cases are of special interest. The first one concerns the steady state of (3.3.21) when a Dirichlet boundary condition is imposed. In that case, the particle activity "relaxes" to its equilibrium value over a characteristic saturation length ℓ_{sat}. The latter is known to play a fundamental role in bedform dynamics [Andreotti *et al.*, 2012, 2010; Balmforth & Provenzale, 2001; Charru, 2006; Parker, 1975]. The second problem of interest is an initial-value problem describing the release and spread of a sediment pulse through time by (3.3.21).

First, we address the Dirichlet boundary value problem and sow how a characteristic saturation length naturally appears in the solution. The steady state of (3.3.21) is sought for a prescribed Dirichlet boundary condition at the origin $\langle\gamma(0)\rangle = 0$ (Fig. 3.4). The problem simplifies to the ordinary differential equation

$$Dy'' - \langle u\rangle y' - (\sigma-\mu)y = -\lambda, \qquad y(0) = 0, \tag{3.3.23}$$

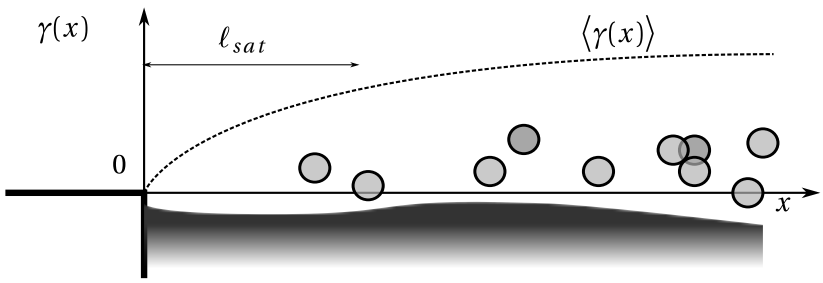

Figure 3.4 – Boundary value problem corresponding to the relaxation of particle activity to equilibrium. ℓ_{sat} is the saturation length.

with $y(x) = \langle\gamma(x)\rangle$. The solution of (3.3.23) is found with classical methods and is given by

$$\langle\gamma(x)\rangle = \frac{\lambda}{\sigma-\mu}\left(1-e^{-x/\ell_{sat}}\right), \qquad \ell_{sat} = \frac{2D}{\langle u\rangle}\left(\sqrt{1+\frac{4D(\sigma-\mu)}{\langle u\rangle^2}}-1\right)^{-1}. \tag{3.3.24}$$

The last expression can be simplified by introducing a dimensionless number $\mathscr{P}_e$, that can be interpreted as a local Péclet number comparing diffusion and advection time scales with respect to a correlation length scale $\ell_c = \sqrt{D/(\sigma-\mu)}$:

$$\mathscr{P}_e = \frac{\langle u\rangle \ell_c}{D}. \tag{3.3.25}$$

The correlation length scale originates from the coupled action of diffusion and particle exchanges with the bed (collective entrainment and deposition) but its meaning is best understood while studying spatial correlations. With respect to these new variables, the saturation length is

$$\ell_{sat} = \frac{2\ell_c}{\mathscr{P}_e}\left(\sqrt{1+4\mathscr{P}_e^{-2}}-1\right)^{-1}. \tag{3.3.26}$$

The behaviour of ℓ_{sat} is shown in Fig. 3.5(a). It increases with the local Péclet number at constant ℓ_c (and thus with $\langle u\rangle$) and with the correlation length at constant $\mathscr{P}_e$. More precisely, if the deposition rate decreases, ℓ_c increases and thus so too does ℓ_{sat}. Roughly speaking, if the particles are moving longer, they will have an impact far from their initial positions, so ℓ_{sat} will be increased. Equivalently, if the collective entrainment rate increases, ℓ_c and ℓ_{sat} increase. This can be explained by the longer distance needed for the collective feedback on particle entrainment to be fully developed. In contrast with aeolian sediment transport, the saturation length ℓ_{sat} does not originate from particle inertia (which is negligibly small in water) but rather from the particle exchanges with the bed while being advected down-

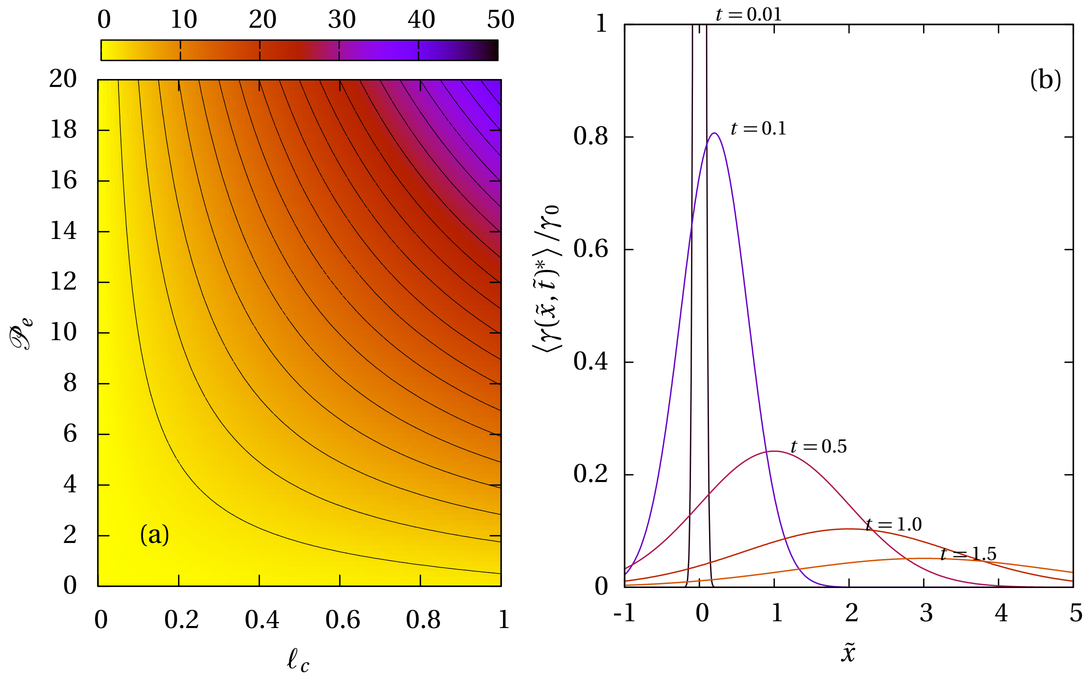

Figure 3.5: (a) ℓ_{sat} as a function of the local Péclet number and the correlation length ℓ_c. (b) Spread of a sediment pulse (Eq. (3.3.29)) for $\mathscr{P}_e = 2$.

about saturation length in bed load transport under water is available yet, so no comparison can be made with the theoretical prediction.

Now, we focus on the time and space propagation of a sediment pulse. While the particle flow is initially at equilibrium (the particle activity given by (3.3.22)), the balance between entrainment and deposition is suddenly disrupted by adding an instantaneous source of sediment at $x = 0$. The evolution of the perturbation term $\langle\gamma^*\rangle = \langle\gamma\rangle - \langle\gamma\rangle_s$ subject to the initial condition $\langle\gamma^*\rangle = \gamma_0\delta(x)$, where γ_0 denotes the strength of the source (i.e., the volume of sediment released) is sought in the following. The scaled variables $x = \tilde{x}\ell_c$, $t = \tilde{t}/(\sigma-\mu)$ are introduced so that in a dimensionless form, (3.3.21) reads

$$\frac{\partial\langle\gamma^*\rangle}{\partial\tilde{t}} + \mathscr{P}_e\frac{\partial\langle\gamma^*\rangle}{\partial\tilde{x}} = \frac{\partial^2\langle\gamma^*\rangle}{\partial\tilde{x}^2} - \langle\gamma^*\rangle, \tag{3.3.27}$$

where $\mathscr{P}_e$ is the local Péclet number defined previously. In the limit $D \to 0$, (3.3.21) degenerates into a purely hyperbolic equation with a sink term. The method of characteristics leads to a solution of the form

$$\langle\gamma^*\rangle = \gamma_0\delta(x - \langle u\rangle t)e^{-t(\sigma-\mu)}, \qquad t \geq 0, \tag{3.3.28}$$

which shows that the initial pulse is transported along the characteristics $x = \mathscr{P}_e \tilde{t}$ (thus at constant velocity) by the stream with no deformation, but its strength is attenuated exponentially over time. For finite values of particle diffusivity, and using Fourier transformation in the space variable, the solution of (3.3.27) is given by (see appendix A.4)

$$\langle \gamma(\tilde{x},\tilde{t})\rangle = \langle \gamma\rangle_s + \frac{\gamma_0}{\sqrt{4\pi\tilde{t}}}\exp\left(-\frac{(\tilde{x}-\mathscr{P}_e\tilde{t})^2}{4\tilde{t}} - \tilde{t}\right), \qquad \tilde{t}\le 0, \tilde{x}\in\mathbb{R}. \tag{3.3.29}$$

The existence of a sink term implies that the volume of sediment released is not conserved, but decreases exponentially over time (bed aggradation due to the excess in sediment). For $\mathscr{P}_e > 0$, the initial source of sediment spreads at infinite velocity as is the case for any linear diffusion problem. Such non-physical behaviour was previously discussed in section 3.1.

3.5 Second moments

Spatial correlations

Let $g(x,x',t)$ to denote the spatial correlation function of the Poisson density variable $\eta(x,t)$. By definition:

$$\begin{aligned} g(x,x',t) &= \langle \eta(x,t), \eta(x',t)\rangle \\ &\equiv \langle \eta(x,t)\eta(x',t)\rangle - \langle \eta(x,t)\rangle^2. \end{aligned} \tag{3.3.30}$$

I show in appendix A.5 that g follows the differential equation

$$\frac{1}{2}\frac{\partial g(r,t)}{\partial t} = D\frac{\partial^2 g(r,t)}{\partial r^2} - (\sigma-\mu)g(r,t) + \mu\langle\gamma\rangle_s\delta(r), \tag{3.3.31}$$

with $r = |x-x'|$. The spatial correlation function of η does not depend on the average velocity of particles. For $t\to\infty$, the stationary solution $g_s(x)$ is obtained by means of Fourier transforms (see appendix A.5):

$$\langle \eta(x), \eta(x')\rangle_s = \frac{\langle\gamma\rangle_s}{2\ell_c}\frac{\mu}{\sigma-\mu}\exp\left(-\frac{|x-x'|}{\ell_c}\right), \tag{3.3.32}$$

where the correlation length in the x-direction $\ell_c = \sqrt{D/(\sigma-\mu)}$ has been introduced previously.

The relation between second moment of η in the Poisson representation and of γ is obtained using Eq. (3.3.20). Thus, the stationary homogeneous spatial correlation function of the particle activity is

$$\langle \gamma(x,t), \gamma(x',t) \rangle_s = \delta(x-x') \langle \gamma \rangle_s + \frac{\langle \gamma \rangle_s}{2\ell_c} \frac{\mu}{\sigma-\mu} \exp\left(-\frac{|x-x'|}{\ell_c}\right). \tag{3.3.33}$$

The stationary spatial correlation function is thus the sum of a Dirac delta function of intensity equal to the mean density of moving particles and an exponential decay with a characteristic length defined by ℓ_c. The correlation length increases with the diffusivity of particles and the collective entrainment rate, but decreases with the deposition rate.

When $\mu = 0$, the process becomes spatially uncorrelated (Poisson point process) but the correlation length remains positive. On the other hand, when $\mu > 0$, the process becomes spatially correlated, so that it cannot be described anymore by a Poisson point process. In the limit $\mu \to \sigma$, spatial correlations become infinitely large. When $\mu \leq \sigma$, the system loses its stability and an exponential increase in the number of moving particles is observed.

Another quantity of interest, often used to describe spatial point processes, is the conditional intensity $h(x-x')$, which gives the conditional probability of finding a particle at x' given that there is a particle at x [Cox & Isham, 1980]. The conditional intensity and the correlation function are directly related by

$$\langle \gamma(x,t), \gamma(x',t) \rangle_s = \delta(x-x') \langle \gamma \rangle_s + \langle \gamma \rangle_s h(x-x') - \langle \gamma \rangle_s^2,$$

so that, by identification, we have

$$h(x-x') = \langle \gamma \rangle_s + \frac{1}{2\ell_c} \frac{\mu}{\sigma-\mu} \exp\left(-\frac{|x-x'|}{\ell_c}\right), \qquad x, x' \in \mathbb{R} \tag{3.3.34}$$

A more convenient function for data analysis is the K-function [Ripley, 1976], where $K(r)$ represents the expected number of moving particles found in a ball of radius $r > 0$ centred on a particle location divided by the mean process rate. This can be calculated from the conditional intensity function by:

$$\begin{aligned} K(r) &= \frac{1}{\langle \gamma \rangle_s} \int_0^r h(u)\mathrm{d}u \\ &= r + \frac{1}{\langle \gamma \rangle_s} \frac{\mu}{\sigma-\mu} \left[1 - \exp\left(-\frac{r}{\ell_c}\right)\right]. \end{aligned} \tag{3.3.35}$$

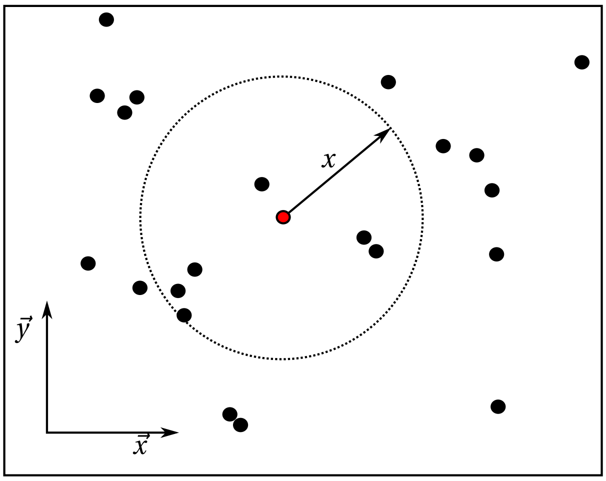

Figure 3.6: Principle of the K-function for a two-dimensional point process.

For a uncorrelated Poisson point process in one dimension, $K(r) = r$. Equation (3.3.35) shows that $K(r) > r$ if $\mu > 0$; so the point process is said to be clustered. This is not surprising as we already noticed particle clusters in Fig. 4.5 and in appendix A.3.

Spatio-temporal correlations

Now, I consider the spatio-temporal correlation function of Eq. (3.3.19), defined as

$$G(x,t) = \langle \gamma(x,t), \gamma(0,0) \rangle_s . \qquad (3.3.36)$$

For any linear Markovian system, a linear equation also exists for the evolution of the time correlation [Gillespie, 1991],

$$\frac{\partial G(x,t)}{\partial t} = D\frac{\partial^2 G(x,t)}{\partial x^2} - \langle u \rangle \frac{\partial G(x,t)}{\partial x} - (\sigma - \mu)G(x,t), \qquad (3.3.37)$$

where the initial condition $G(x,0)$ is the stationary-homogeneous spatial correlation function (3.3.33). By making the transformations $\tilde{t} = (\sigma - \mu)t$, $\tilde{x} = x/\ell_c$, the expression of the spatio-temporal correlation function can be obtained (details in appendix A.6):

$$G\left(\tilde{x}, \tilde{t}\right) = G_d(\tilde{x}, \tilde{t}) + G_r(\tilde{x}, \tilde{t}), \qquad \tilde{t}, \tilde{x} \in \mathbb{R}, \qquad (3.3.38)$$

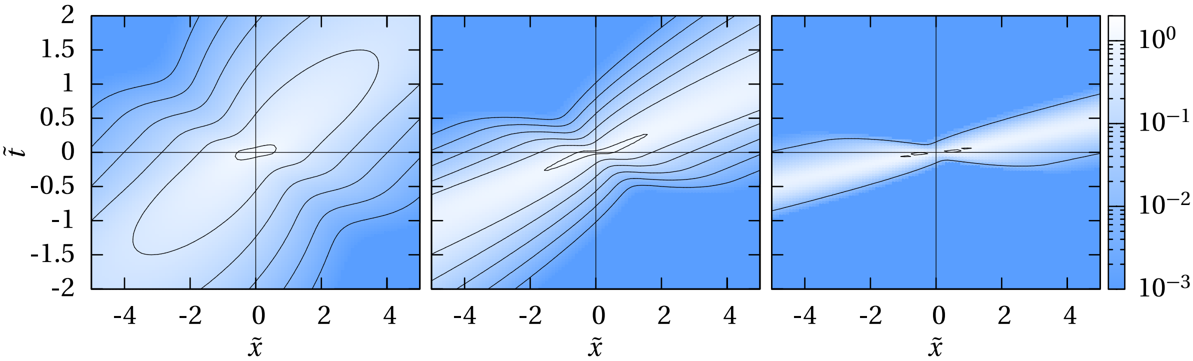

Figure 3.7: Contour plot of the spatio-temporal correlation function $G\left(\tilde{x},\tilde{t}\right)/(\langle\gamma\rangle_s/\ell_c)$ for $\mathscr{P}_e = 2, 5$ and 10 (from left to right) talking $\mu = 3.5$ s^{-1} and $\sigma = 4.0$ s^{-1}.

with

$$G_d\left(\tilde{x},\tilde{t}\right) = \frac{\langle\gamma\rangle_s}{2\ell_c\sqrt{\pi|\tilde{t}|}}\exp\left[-\frac{\left(\tilde{x}-\mathscr{P}_e\tilde{t}\right)^2}{4\tilde{t}} - \tilde{t}\right], \tag{3.3.39}$$

and

$$G_r(\tilde{x},\tilde{t}) = \frac{\langle\gamma\rangle_s\mu}{4\ell_c(\sigma-\mu)}\left\{\operatorname{erfc}\left[\left(1-\frac{\mathscr{P}_e}{2}\right)\sqrt{|\tilde{t}|}+\frac{\tilde{x}}{2\sqrt{|\tilde{t}|}}\right]\exp(\tilde{x}-\mathscr{P}_e\tilde{t}) + \operatorname{erfc}\left[\left(1+\frac{\mathscr{P}_e}{2}\right)\sqrt{|\tilde{t}|}-\frac{\tilde{x}}{2\sqrt{|\tilde{t}|}}\right]\exp(\mathscr{P}_e\tilde{t}-\tilde{x})\right\}. \tag{3.3.40}$$

$G(x,t)$ is the sum of two contributing terms. $G_d(x,t)$ quantifies the spread and advection of the delta-correlated term of Eq. (3.3.33) while $G_r(x,t)$ encodes the relaxation of the non-Poissonian spatial correlations through time. If $\mu = 0$, the stochastic process is purely Poissonian so that $G_r(x,t) = 0$. In Fig. 3.7, I plot $G\left(\tilde{x},\tilde{t}\right)/(\langle\gamma\rangle_s/\ell_c)$ for different values of $\mathscr{P}_e$.

It is clear from Fig. 3.7 that $\mathscr{P}_e$ plays a crucial role in the spread of the correlation function of the particle activity through time and space. In particular, in the limit of large $\mathscr{P}_e$ (right side of Fig. 3.7), the spatial correlation function of the particle activity (3.3.33) is projected without deformation onto the time axes. In this case, spatial correlations at a given time (Eq. (3.3.33)) are equal to temporal correlations at a given location (Eq. (3.3.37) with $\tilde{x} = 0$). The correspondence between the space and the time axes is then given by $x \sim \langle u\rangle\, t$ or $\tilde{x} \sim \mathscr{P}_e\tilde{t}$ (the proof is given in appendix A.7). This limiting case may be compared with Taylor's frozen turbulence hypothesis in fluid mechanics [Moin, 2009].

4 Summary

4.1 Local model key-points

In this chapter, a local stochastic model was proposed for the motion of bed load particles under water. Based on Ancey *et al.*'s [2008] birth-death Markov process, this local model is able to capture the correlated structures that develop during particle motions at all spatial scales. In separating the stochastic evolution of particle velocities from the bed exchange processes, a master equation for the probability density of the particle activity through space and time could be derived. The Poisson representation was then used to solve the master equation, and to derive a Langevin equation for the Poisson activity $\eta(x,t)$ of the form

$$\frac{\partial \eta(x,t)}{\partial t} = \text{deterministic flux} + \text{deterministic sources} + \text{stochastic sources}. \tag{3.4.1}$$

The deterministic bed load flux includes both a purely advective term and a diffusive term due to particle velocity fluctuations. The latter has also been reported recently by Furbish *et al.* [2012*a*], using an ensemble averaging procedure.

The expression for the moving phase, together with the Exner equation (the Exner equation expresses the conservation of the sediment mass during bed exchanges) thus form a set of coupled stochastic differential equations,

$$\begin{aligned} \mathrm{d}\eta(x,t) &= \left[-\langle u\rangle \nabla\eta(x,t) + D\nabla^2\eta(x,t) - (\sigma-\mu)\eta(x,t) + \lambda\right]\mathrm{d}t + \sqrt{2\mu\eta(x,t)}\,\mathrm{d}W(x,t), \\ \mathrm{d}\beta(x,t) &= \mathrm{d}\eta(x,t) + \left[\langle u\rangle \nabla\eta(x,t) - D\nabla^2\eta(x,t)\right]\mathrm{d}t, \end{aligned} \tag{3.4.2}$$

where $\beta(x,t)$ is the Poisson representation of the density of particles in the bed $b(x,t)$. The bed elevation is then simply $y_b \propto v_s b(x,t)/B$, B being the flume width. This system may be solved with numerical schemes adapted for stochastic equations with special care to preserve the positivity of η [Higham, 2008]. The evolution of the bed elevation can be coupled to the Saint-Venant equations (3.1.1)–(3.1.3) in a complete morpho-dynamical scheme.

Analytical results for the first and second moments of the particle activity were also derived. Two length scales appeared naturally from the analysis: the saturation length scale ℓ_{sat} and the correlation length scale ℓ_c. A local Péclet number $\mathscr{P}_e$ was also found to play an important role in the motion of particles.

4.2 Model limits

Like any simplification of reality, the model proposed here relies on fairly strong simplifying assumptions. First, a full phase-space representation has been avoided by suggesting that the relaxation time of particle velocity was small compared to the other time scales. Second, sediment particles have been assumed to be points. Thus, in the model, two particles can be found to be separated by a distance less than their diameter, leading to non-physical inter-penetration of particles.

Third, the interactions of moving particles with the bed have been simplified to the point of absurdity. Indeed, only three types of exchanges with the bed have been retained: entrainment, collective entrainment and deposition. More complex exchanges involving two or more particles may also be involved, particularly when particle activity becomes high. Once a sheet-layer flow is fully developed, the simple exchanges assumed here may be insufficient to describe reality, as moving particles would be continuously interacting with each others. In this limit, continuous models based on energy dissipation inside the bed load layer [Bagnold, 1973] might be more adequate.

Last but not least, all the analytical results presented in this chapter are based on the assumption that all exchange rates remained constant in time and space. As those rates are expected to change with flow shear velocity and local bed slope, even a weak coupling between the bed load phase, the bed, and the fluid flow may reveal complex and non-linear phenomena. Still, it is possible, in theory, to allow the coefficients of the stochastic equation (3.3.19) to vary and to explore numerically the behaviour of solutions.

IV Experiments

Four different experimental data sets were used to compare with the theoretical results of chapter III. Two of them have previously been published [Böhm *et al.*, 2004; Roseberry *et al.*, 2012]. The two others come from experimental setups specially built during the thesis to observe spatial and temporal fluctuations of bed load at the same time [Heyman *et al.*, 2014, 2013]. All these experimental studies provide high resolution measurements of particle transport.

Hereafter, all Böhm *et al.* [2004] experiments are denoted by the prefix B, Roseberry *et al.* [2012] experiment by R, Heyman *et al.* [2013] experiments by H and Heyman *et al.* [2014] experiments by J. The numbers following the prefix specify experimental slope and solid discharge. For instance B10-5 stands for a Böhm *et al.* [2004] experiment conducted using a 10% sloping flume with a mean solid discharge of 5 particles/s. A summary of the available data is provided in Table 4.1.

	B	d_{50}	τ_s	Fr	Re	tanθ	$\bar{v}$	$\bar{h}$	$\bar{q}_s/\nu_s$	$\bar{\gamma}$	$\mathscr{L}$	$\mathscr{T}$
B10-5	0.6	6	0.11	1.42	$4\cdot10^3$	10.0	0.41	1.0	4.9	28.9	0.25	60
R0-79	-	0.5	0.06	0.35	-	-	0.31*	12.5	78.7	1711.0	0.08	0.4
H7-1	8.0	7	0.08	1.44	$7\cdot10^3$	7.0	0.53	1.4	1.1	-	0	$2\cdot10^5$
H7-6	8.0	7	0.09	1.48	$1\cdot10^4$	7.0	0.60	1.7	5.9	-	0	$4\cdot10^4$
H7-13	8.0	7	0.09	1.50	$1\cdot10^4$	7.0	0.62	1.8	13.4	-	0	$7\cdot10^3$
J3-1	3.5	7	0.14**	1.30	$3\cdot10^4$	3.5	0.80	3.8	1.4	4.6	1	150
J4-1	3.5	7	0.17**	1.39	$3\cdot10^4$	4.5	0.86	3.9	1.2	3.9	1	150
J5-1	3.5	7	0.14**	1.47	$2\cdot10^4$	4.7	0.80	3.1	0.9	2.8	1	150

Table 4.1: Experimental parameters. B [cm], channel width; d_{50} [mm], mean particle diameter; τ_s [-], Shields stress; Fr [-], Froude number; Re [-], Reynolds number; tan(θ) [%], slope angle; $\bar{v}$ [m.s^{-1}], mean flow velocity; $\bar{h}$ [cm], mean water depth; $\bar{q}_s/\nu_s$ [particles/s], mean output solid discharge; $\bar{\gamma}$ [particles/m], mean activity; $\mathscr{L}$ [m], measurement length; *: $\mathscr{T}$ [s], measurement duration. *: In this experiment, $\bar{v}$ is the average flow velocity 1 cm above the bed. **:The Shields stress could not be determined exactly in these experiments, the channel walls bearing an important but unknown fraction of the total stress.

1 Setups

1.1 B experiment

This experiment was carried out in a narrow steep flume where sediment consisted of glass beads of equal size (6 mm). Particle transport was completely two-dimensional; this allowed Böhm *et al.* [2004] to take pictures through the side wall and detect and track individual particles via image processing. Camera resolution was 640 × 192 pixels with a frame rate of 129.2 frame per seconds (fps). Each sequence comprised 8000 images corresponding to a duration of approximately 1 min. The acquisition length was 22.5 cm, for a resolution of 0.3 mm/pixel. Thus this imaging technique covers about 2 orders of magnitude in space. For further information on the experimental conditions, the reader is referred to [Ancey *et al.*, 2006, 2008; Böhm *et al.*, 2004].

Fig. 4.1 shows an example of a recorded image and the corresponding reconstruction of particle positions and velocities using image processing.

1.2 R experiment

Roseberry *et al.* [2012] presented a set of experiments where particle trajectories were sampled in a two-dimensional window of the bed viewed from the top. High-speed imaging at 250 fps over a 7.57 cm (streamwise) by 6.05 cm (cross-stream) bed-surface domain, and with 1280×1024 pixels resolution, provided the basis for tracking particle motions (with a precision of 0.06 mm/pixel). Bed material consisted of relatively uniform coarse sand with an average

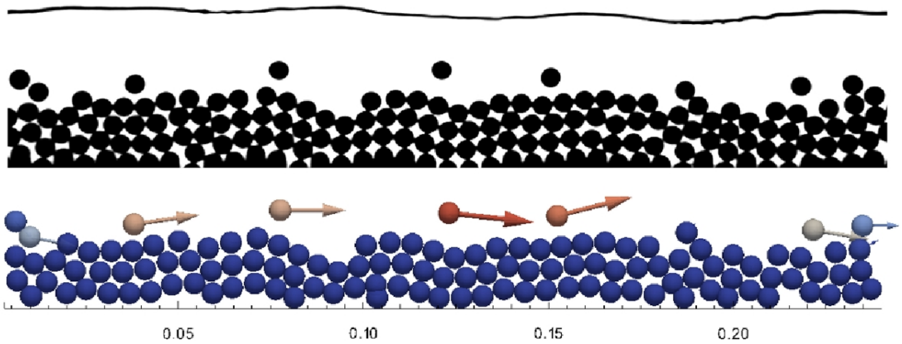

Figure 4.1: Image recorded during B experiment and visualization of particles trajectories after image processing. Units are in meters.

diameter of $d_{50} = 0.5$ mm.

The data set involved one experiment with a total duration of 0.4 seconds, i.e., 100 frames (Fig. 4.2). In contrast with the three other data sets, the R experiment concerns relatively small particles (sand) over shallow slope (the slope is not given in [Roseberry *et al.*, 2012] but one can guess it because the Froude number is much lower than unity).

1.3 J experiments

Experiments were carried out in a 2.5-m-long flume. The erodible bed was made of natural sediment particles with mean diameter of 8 mm. The flume was 3.5 cm wide and the water depth was ranging from 3 to 4 cm during experiments. The channel slope ranged between 3% and 5%. The flow was fully supercritical. Small antidunes were occasionally growing and propagated upstream, but the bed remained nearly flat in all experiments. As the channel width to flow depth ratio was relatively small ($B/h \sim 1$), the fraction of the shear stress taken by the bed was certainly reduced, because of the increased side wall friction. Experimental studies [Knight, 1981] report a drop of about 40 to 60% of the bed shear stress for such aspect ratio. It is thus hard to determine precisely the experimental Shield stress without any direct flow velocity measurements.

The originality of this data set compared to the two others lies in its high temporal and spatial resolutions. Two cameras of 1280×200 pixels resolution, placed side by side, took pictures from the transparent side wall at a rate of 200 fps. The length of the observation window was slightly less than 1 m (with a precision of about 0.4 mm/pixel) while the duration of a sequence was 150 seconds (30 000 images). For each experiment, four film sequences were repetitively taken to ensure good statistical results.

Image processing and automatic particle tracking were then performed on these images. The processing steps from raw images to particle trajectories were the following:

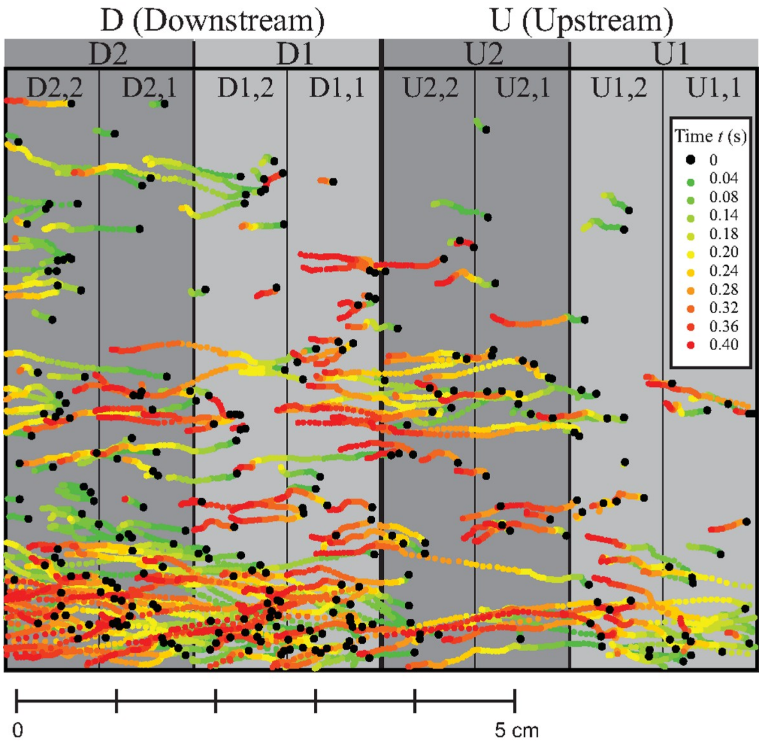

Figure 4.2: Map view of R experiments showing particle motions occurring during the 0.4 sec time series; note the clustering of motions, partly reflecting effects of the turbulent sweeps. (Reproduced from [Roseberry *et al.*, 2012] with the authorization of the authors and AGU.)

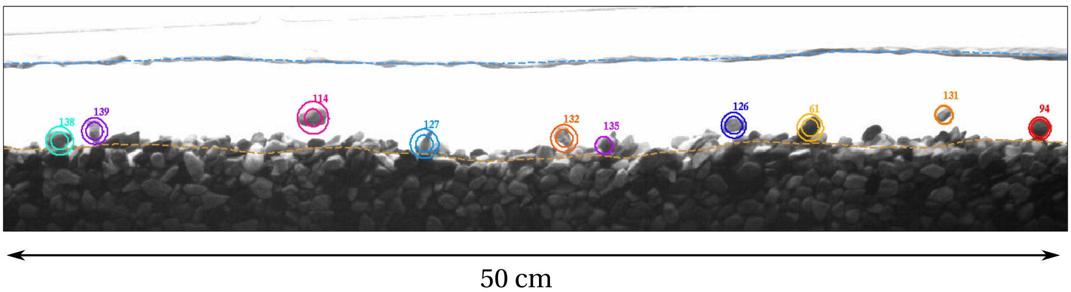

Figure 4.3: Preview of the first camera in the J experiments, and particle tracking.

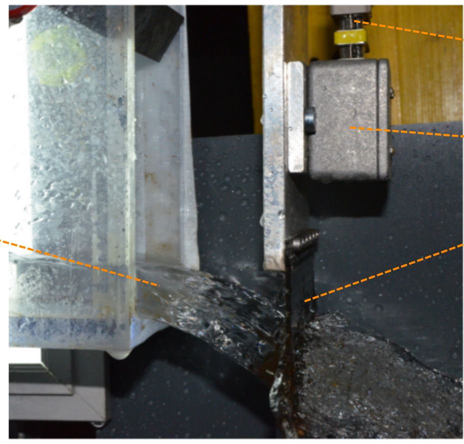

Figure 4.4: Particle counting technique at the outlet of the H experiments flume.

1. First I treated the raw images using the powerful yet simple method of median background subtraction [Radice *et al.*, 2006; Yilmaz *et al.*, 2006]. This allows a distinction between an immobile background (made up of particle resting on the bed) and a moving foreground (the moving particles).
2. An algorithm was then used to detect the centroid position of each moving particle in the foreground images. This was achieved after thresholding the foreground image and computing properties of connected regions (such as area, barycentre, eccentricity...)
3. Moving particles between two consecutive images were then associated into trajectories. The Hungarian algorithm was used here to obtain the best combinations [Kuhn, 1955]. In case of conflict (for instance, if two particles are assigned to the same particle in the following frame), the trajectory was supposed to end and a new trajectory was built.
4. Finally, to reconstruct broken trajectories, a Kalman filter was applied to each missing measurement and overlapping trajectories were merged.

1.4 H experiments

H experiments were carried out in a 2.5 m long, 8 cm wide steep slope flume. The erodible bed was made of uni-sized natural sediment particles of mean diameter 8±1.5 mm. The water depth ranged from 1 to 3 cm during experiments. This setup was able to reproduce the fully turbulent (Re$\geq$ 8000) and supercritical flow of natural steep rivers, while avoiding complex 3-dimensional patterns like meanders and bars owing to the high water depth to channel width ratio. Moreover, the extremely narrow grain size distribution limited fluctuations due to size segregation and other related phenomena [Frey & Church, 2009].

Three experiments of increasing Shields stress are presented here. In each experiment, the slope was kept constant and the water discharge was adjusted to reach the intended bed shear stress. In addition, the sediment input was controlled to guarantee a global equilibrium between erosion and deposition and to maintain the mean slope value.

As a consequence of the fairly high Froude number (Fr $\sim$ 1.4), antidunes, scaling with the water depth, formed in all experiments and propagated upstream along the channel. Their lee face angle ranged from 10 to 20°, close to the angle of repose of a slope sheared by a fluid flow [Loiseleux *et al.*, 2005].

Sediment fluxes were measured both at the entrance and at the output of the flume by a new technique developed by a former PhD student (Francois Mettra) and detailed as follows. Upon leaving the channel, each particle hits a metallic plate and the impact is recorded by a small accelerometer tied to the plate. A peak-over-threshold method is then applied to detect the times of the consecutive particle impacts (Fig. 4.4). If sufficient damping is provided to avoid spurious vibrations of the plate, this method ensures an extremely good time resolution in bed load discharge rates. As the grain size distribution is narrow, little error is made when converting the number of particles to a sediment weight. Finally, the time series covered at least 6 orders of magnitude (from $\sim 10^{-1}$ to 10^5 s). To validate the method, the output weight of sediment was systematically measured during experiments.

1.5 Turbulence characteristics and particle dynamics

Flow turbulence is of great importance for the sediment transport process, particularly when the flow strength is close to the threshold of incipient motion. Even if the flow Reynolds number varies for each experiment presented here, all of them concern fully turbulent flows.

In spite of this, the characteristics of turbulence may diverge from one experiment to another owing to the presence of the lateral channel walls. Indeed, experiment B took place in an extremely narrow channel so that the size of turbulent structures was strongly limited by the wall. In contrast, experiments J and H were carried out in a channel whose width was larger or comparable to the water depth so that the limiting factor for the size of the turbulent structures was the water depth rather than the channel width—as it is often the case in steep mountain rivers. At the far opposite, the flow of experiment R was sub-critical and both water depth and channel width were very large compared to the grain size. In this case, turbulence was only governed by the boundary layer that forms at the surface of the granular bed.

Another major difference existing between experiments B, J, H and R arises from the diameters of particles transported. The particle diameters of experiments B, J and H are about 10 times larger than the particle diameter of experiment R, so that the particle response to the flow velocity is likely to be different. The Stokes number quantifies such a response. It is defined as the ratio of the characteristic time of the particle to a characteristic time of the flow: St= $\rho \bar{v} d_{50}/(9\mu_f)$, with ρ is the particle density and μ_f the dynamic viscosity. For experiments B, J and H, it is always greater than 100, while in experiment R, it is about 3 (Table 4.2). Thus, particles of experiment B, J and H respond much slower to the flow than particles of experiment R. As will be shown in the following, the statistical characteristics of their trajectories will thus be fundamentally different.

2 Experimental data

2.1 Experiments B, R and J

In these motion-picture experiments, a typical data set consists in a set of k particle trajectories (x_i, y_i, t_i) in the camera's plane $(\vec{x}, \vec{y})$. No information was gathered about shape and size of particles; I focused only on the position of the centres of mass (x_i, y_i). In all experiments, the $\vec{y}$ axis is perpendicular to the mean transport direction of particles. I will mostly be interested in the pair of trajectory coordinates (x_i, t_i), leaving the third dimension aside.

Those trajectories are measured during a given (limited) time period $\mathscr{T}$ and spatial window $\mathscr{L}$ (see Table 4.1). They can be represented in a time-space plane, as shown in Fig. 4.5 and in appendix B.2.

Trajectories consist in one-dimensional continuous segments in the time-space plane. Instantaneous particle velocity is obtained by finite difference,

$$u_k(t_i) = \frac{x_i - x_{i-1}}{\Delta t}, \tag{4.2.1}$$

where Δt is the reciprocal of the frame rate of the camera.

In order to discriminate between moving and resting particles, a threshold must be defined. This threshold is *arbitrary* in the sense that a particle is never totally resting on the bed, but its position oscillates slightly due to the turbulent flow drag. It is worth noting that the choice of the threshold is likely to influence the results. Indeed, by including the slowest particles into the group of moving particles, more importance will be given to transport by rolling or sliding. On the contrary, by ignoring them, saltation will be the dominant mode of transport. In appendix B.1, a sensitivity analysis of the effect of the velocity threshold is provided. In the following, we chose (arbitrarily) $||\boldsymbol{u}|| > 0.05, 0.0, 0.003$ m.s^{-1} for experiments B [1], R and J respectively, where the magnitude of particle velocity $||\boldsymbol{u}||$ has been previously smoothed by a moving average time filter of length 0.038, 0, and 0.035 s for experiments B, R and J respectively.

1. The relatively high velocity threshold on experiment B (about 30% of $\langle u \rangle$) is required to discard the particles creeping inside the bed. Moreover, as the definition of experiment B is fairly low (640 pixels for about 25cm), the minimum observable change in velocity is 0.05039 m.s^{-1}

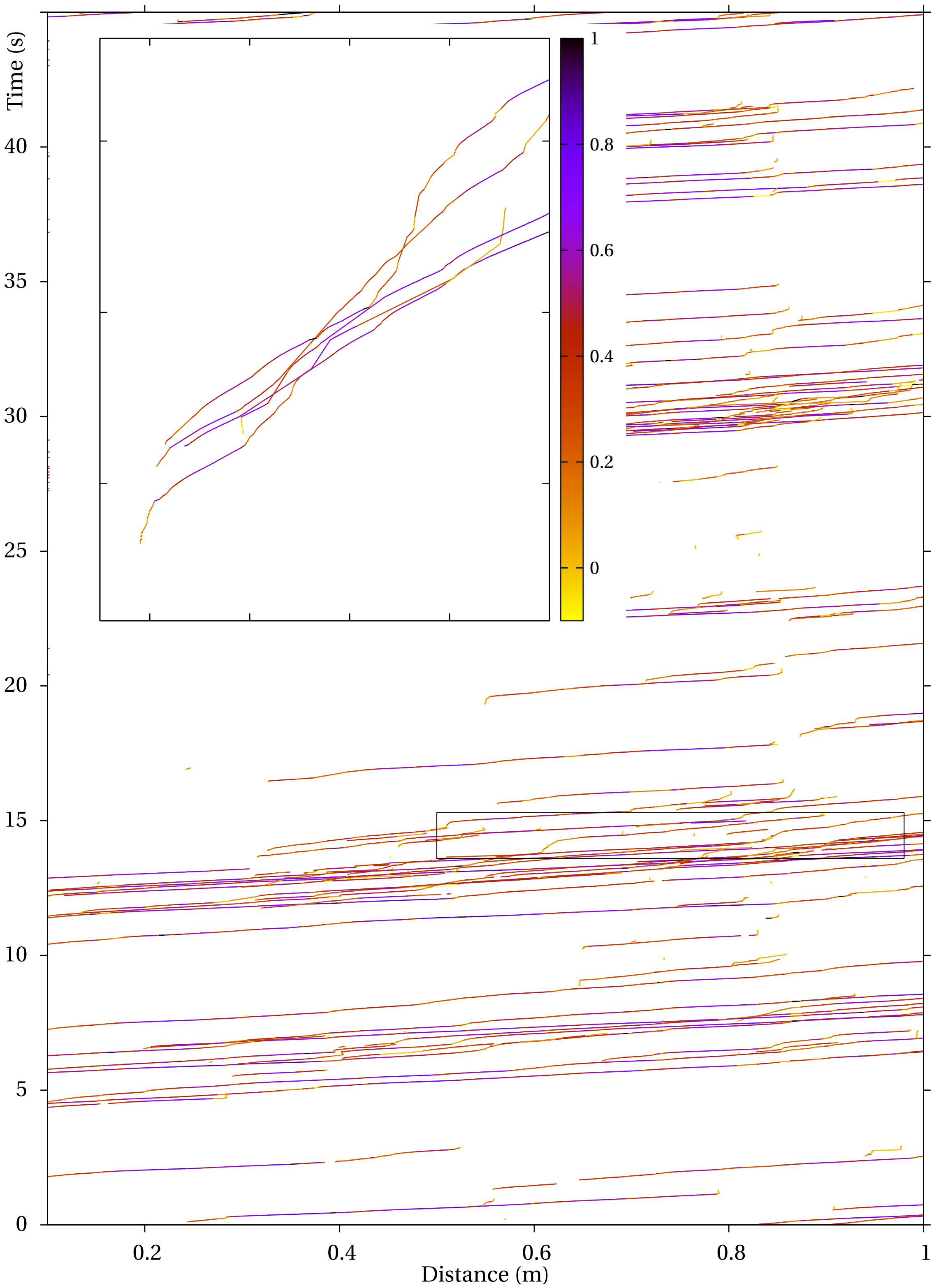

Figure 4.5: Sample of particle trajectories in the time-space plane (experiment J). The colours encode particle velocities (m/s). A close up of the black rectangle is shown in the upper left corner.

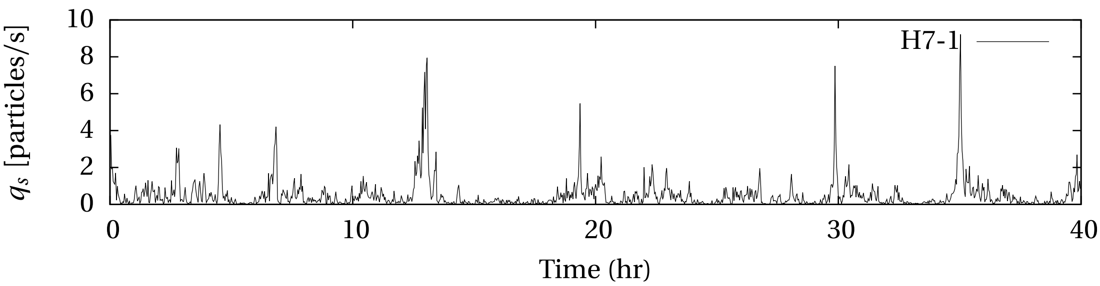

Figure 4.6: Time series of solid discharge in H experiment.

2.2 Experiments H

Experiment H contrasts from experiments B, R and J as no spatial information is gathered about particle trajectories. Instead, it was built to record the arrival time of moving particles at a precise location during long time periods. Thus, the data consists of consecutive times $t_1 < t_2 < t_3...$ representing each passage of a particle (Fig. 4.7(c)). This experiment has the advantage of providing extremely long time series (tens of hours), and thus allows for precise statistical treatment (Fig 4.6).

2.3 Averages

We have seen in chapter II section 2 that the definition of the bed load transport flux depends greatly on the chosen averaging method. Although ensemble averaging is the best procedure to characterize a stochastic process, it has little value for experimentalists. Indeed, measurement techniques allow only the sampling of spatial and temporal averages. Spatial averaging is mainly related to motion-picture experiments (such as particle image velocimetry or particle tracking, in experiments B, R and J for instance), where the information about bed load particle locations can be obtain at a given time over a spatial region. On the contrary, temporal averaging relates to more classical measurement devices, which sample bed load at a given position in time as in experiment H for instance. Relating both averages is not trivial in the majority of cases.

In the following, I highlight some of the relationships between surface, volume and time averages of the experimental bed load flux. For simplicity, I assume that particle motion occurs only in one direction $\vec{x}$, but the results are also valid for more complex cases. I assume also that all the particles have the same volume v_s [m^3].

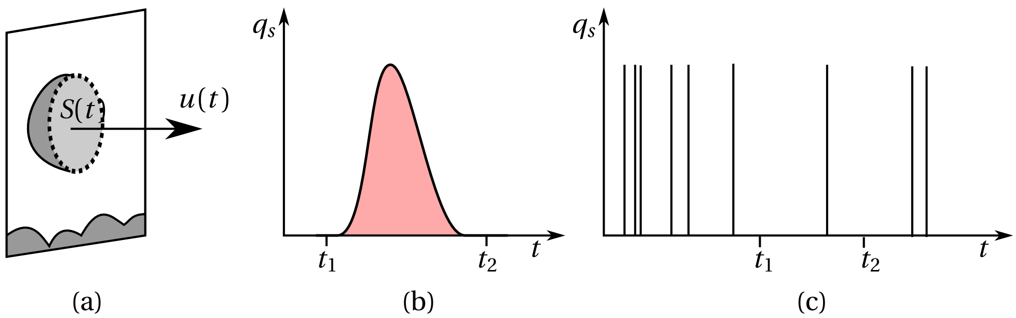

Figure 4.7: Surface flux. (a) Geometrical configuration (b) Surface flux through time. (c) Particle arrival times.

Surface average

The natural definition of the instantaneous solid flux through a surface perpendicular to $\vec{x}$ (Fig. 4.7(a))

$$q_s(t) = S(t)u(t), \qquad [\mathrm{m^3 s^{-1}}] \tag{4.2.2}$$

where $S(t)$ is the portion of surface occupied by a particle and $u(t)$ the speed of that particle. Eq. (4.2.2) differs slightly from Eq. (2.2.1) in that it is assumed that particles cross one at a time the surface. The flux between time t_1 before the particle crossed the surface and time t_2 after the passage of the particle is plotted in Fig. 4.7(b).

Now, take the cumulative flux between t_1 and t_2:

$$[\mathscr{Q}_s]_{t_1}^{t_2} = \int_{t_1}^{t_2} S(t)u(t)\mathrm{d}t = v_s \qquad [\mathrm{m^3}]. \tag{4.2.3}$$

Unsurprisingly, the time integral of the surface flux is equal to the volume of the particle.

Time average

In many experiments, only time series of bed load rates are available (for instance experiment H). If the measurement device is precise enough, all the particle arrival times may be recorded. This is the case for the acoustic sensors developed in [Heyman *et al.*, 2013]. A typical output of such measurement is represented in Fig. 4.7(c).

The instantaneous flux is zero almost everywhere except at the precise time a particle passes.

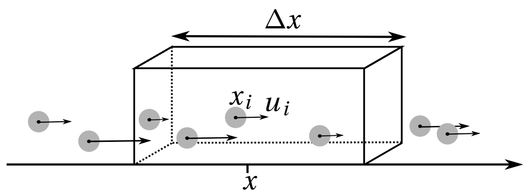

Figure 4.8: Volume average.

The cumulative flux between t_1 and t_2 can be expressed by

$$[\mathcal{Q}_s]_{t_1}^{t_2} = v_s \int_{t_1}^{t_2} \sum_i \delta(t - t_i)\mathrm{d}t, \tag{4.2.4}$$

where t_i are the arrival times of particles. If only one particle passes through the plane between t_1 and t_2, $[\mathcal{Q}_s]_{t_1}^{t_2} = v_s$ and the cumulative flux obtained with the surface-based definition is retrieved.

Although trivial, this result highlights the equivalence between the continuous surface based flux, and the discrete time series of particle passages. The bell shape of the flux obtained with the surface based definition (Fig. 4.7(b)) is approximated by Dirac delta functions in the case of bed load time series (Fig. 4.7(c)). When integrated over a sufficiently long time interval (of the order of $d_{50}/\langle u\rangle$), the cumulative flux obtained by each method is equal.

Volume average

I now consider volume averaging, which is particularly relevant in motion-picture experiments. In general, volume averaging does not relate easily to time averages, except in the case of an infinitely small volume. To prove this, consider a cloud of moving particles located in x_i (Fig. 4.9). I assume that the particles are points (their mass is concentrated at their gravity centres). The volume average flux over a window of length Δx centred at x can be expressed as [Ancey *et al.*, 2008]

$$q_s(x, \Delta x) = \frac{v_s}{\Delta x} \int_{\Delta x} \sum_i \delta(x - x_i) u_i \mathrm{d}x \equiv \frac{v_s}{\Delta x} \sum_{i=1}^{N(t)} u_i, \tag{4.2.5}$$

where $N(t)$ is number of moving particles in the volume. As before, I consider the cumulative flux between two times t_1 and t_2,

$$[\mathcal{Q}_s(x, \Delta x)]_{t_1}^{t_2} = \frac{v_s}{\Delta x} \int_{t_1}^{t_2} \int_{\Delta x} \sum_i \delta(x - x_i) u_i \mathrm{d}x\mathrm{d}t. \tag{4.2.6}$$

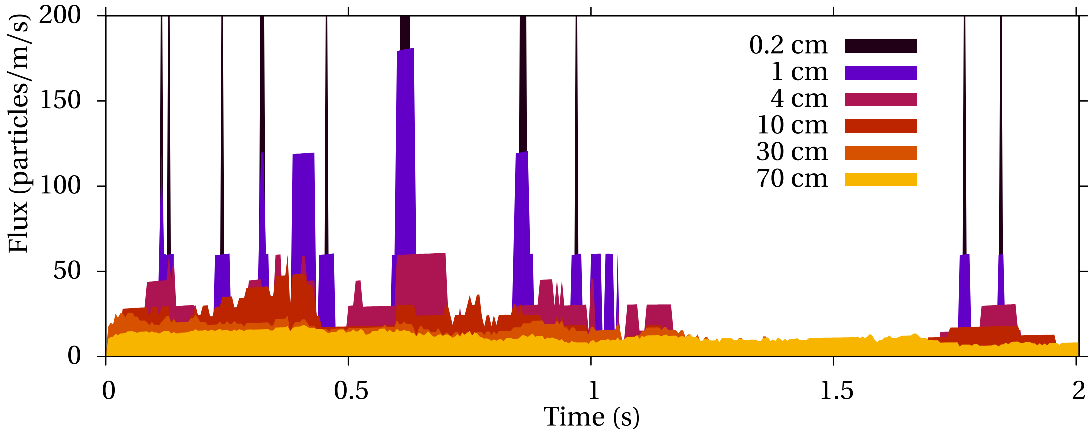

Figure 4.9: Instantaneous volume average flux through time depending on the volume size Δx.

For any Δx, there is no evident relationship between Eq. (4.2.5) and Eq. (4.2.4).

However, by letting $\Delta x \to 0$, there will be a limit when the volume contains only one or zero particles. Setting t_1 to be the time the particle enters the volume, and t_2 the time it leaves the volume, and assuming that the particle velocity does not change much during this short time interval:

$$[\mathscr{Q}_s(x, \Delta x \to 0)]_{t_1}^{t_2} = \frac{v_s}{\Delta x} u_i(t_2 - t_1) = v_s. \tag{4.2.7}$$

In a similar fashion as the cumulative surface solid flux equals the cumulative time average solid flux, the cumulative volume average flux tends to the cumulative time average flux for sufficiently small volumes ($\Delta x \to 0$). Fig. 4.9 shows the effect of the volume size on the measured flux. For large volumes, the temporal flux appears mostly continuous, as many particles are included in the average. As the volume is reduced, the flux is more and more intermittent (discontinuous), alternating between periods of zero values and periods of positive values (when a particle enters the volume). When decreasing Δx, the number of particles present in the volume has an increasing importance on the value of the instantaneous volume averaged solid flux. At the limit of an infinitely small volume, the flux is zero everywhere except at some discrete time where it takes an infinite value. In this limit, the flux is completely equivalent to the passage time of particles described previously while the velocities of particles are not involved in the expression of the solid flux.

	B10-5	R0-79	J3-1	J4-1	J5-1
d_{50}	6	0.5	7	7	7
$\bar{u}$	0.170$\pm$*0.001*	0.046$\pm$*0.001*	0.310$\pm$*0.001*	0.300$\pm$*0.001*	0.320$\pm$*0.001*
Re_p	$1\cdot10^3$	$1\cdot10^1$	$2\cdot10^3$	$2\cdot10^3$	$2\cdot10^3$
St	$3\cdot10^2$	$3\cdot10^0$	$6\cdot10^2$	$6\cdot10^2$	$6\cdot10^2$
σ_u	0.11	0.04	0.22	0.23	0.23
t_σ	0.37$\pm$*0.01*	0.54$\pm$*0.01*	1.93$\pm$*0.10*	1.99$\pm$*0.12*	1.78$\pm$*0.12*
σ	2.72$\pm$*0.09*	1.85$\pm$*0.09*	0.52$\pm$*0.03*	0.50$\pm$*0.03*	0.56$\pm$*0.03*
t_r^S	3.00	0.02	4.08	4.08	4.08
t_r	0.14$\pm$*0.02*	0.12$\pm$*0.03*	0.34$\pm$*0.01*	0.45$\pm$*0.01*	0.18$\pm$*0.03*
$k_B T/\zeta$	15$\pm$*2*	1.5$\pm$*0.3*	59$\pm$*2*	89$\pm$*2*	55$\pm$*3*
$\sigma_u^2 t_r$	17$\pm$*3*	2$\pm$*0.5*	164$\pm$*5*	238$\pm$*5*	95$\pm$*16*

Table 4.2: Transport and deposition of particles: parameter estimates and 95% confidence interval. $\bar{u}$ [m.s^{-1}], average particle velocity; Re_p [-] Particle Reynolds number; St [-], Stokes number; σ_u [m.s^{-1}], standard deviation of particle velocity; t_σ [s], mean deposition time; $t_r^S = m/(3\pi\mu d)$ [s] Stokes relaxation time; ζ [10^{-6}N.s.m^{-1}] drag coefficient; t_r [s] particle velocity relaxation time; $k_B T/\zeta$ [cm^2.s^{-1}], particle diffusivity (also denoted D); $\sigma_u^2 t_r$ [cm^2.s^{-1}], particle diffusivity (other definition).

3 Particle transport and deposition

In this section, I show how the deposition rate σ, the diffusivity D and the relaxation time t_r may be estimated independently with the experimental particle trajectories. The estimates are summarized in Table 4.2.

3.1 Deposition rate

The deposition time scale could be easily obtained if the jump duration of particles (the time between entrainment and deposition) was available. However, most motion-picture experiments are limited in space, so that part of the trajectories entering and leaving the observation window are lost. Alternatively, the mean deposition rate can be obtained by dividing the mean number of deposition events in the observation window per unit time by the mean number of moving particles:

$$\sigma = \frac{N_\sigma}{T\bar{N}}, \tag{4.3.1}$$

with N_σ the number of particle depositions during the period T. However, this method does not give information on the confidence interval of the estimated σ.

Another possible way of estimating the deposition rate relies on the fact that, according to the

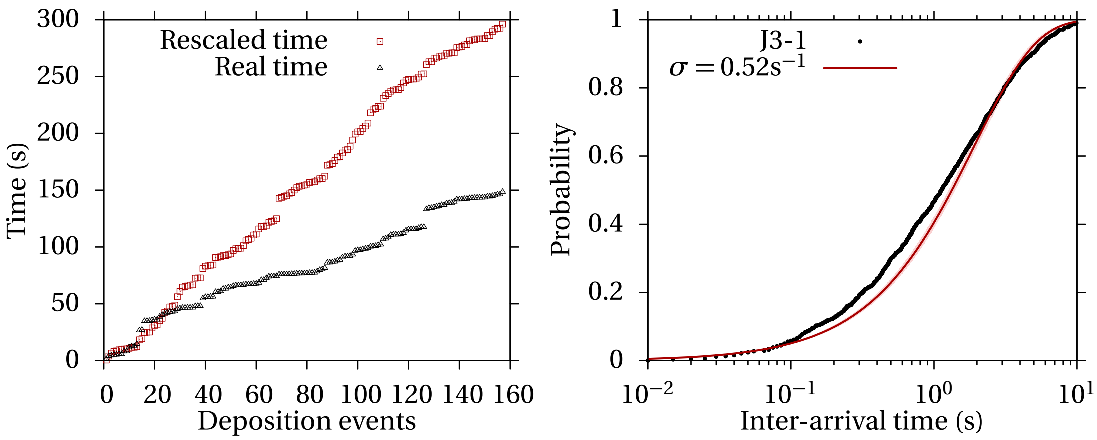

Figure 4.10: (a) Deposition process in real and rescaled time for experiment J3-1. (b) Empirical cumulative distribution of the inter-arrival time of deposition events and fitted exponential cumulative distribution for experiment J3-1.

memoryless property of Markov process, the probability of observing a particle deposition in a window Δx in a small time interval Δt is constant and equal to $\sigma N(t)\Delta t$, where $N(t)$ is the number of moving particle in that window. Thus, the deposition process can be envisioned as an inhomogeneous Poisson process with rate $\sigma N(t)$, where N is a function of time which can be measured experimentally. By rescaling time t according to $N(t)$, we can transform the inhomogeneous Poisson process into an homogeneous Poisson process [Cox & Isham, 1980]

$$T(t) = \int_0^t N(y)\mathrm{d}y. \tag{4.3.2}$$

In this new time space $T(t)$, the deposition process is homogeneous and has a rate equal to σ, and the time between deposition events is exponentially distributed with a mean arrival time $t_\sigma = \sigma^{-1}$ (Fig. 4.10).

Finally, we estimate t_σ and its 95% confidence interval by maximizing the likelihood function of the exponential. Values of $t_\sigma = \sigma^{-1}$ are reported in Table 4.2 for experiments B, R and J.

3.2 Particle transport

The probability density functions of particle velocities are presented in Fig. 4.11 for experiments B, R and J. Eq. (3.3.4) seems to fit experiments J and B relatively well. In these experiments, negative velocities occurred less frequently than predicted by Eq. (3.3.4) [2]. The exponential distribution describes the behaviour of particle velocities in experiments J and B poorly, but seems more appropriate for experiment R. These results are confirmed by the

2. A truncated Gaussian distribution, as used by Ancey & Heyman [2014], may improve the fit. In this case, a reflecting boundary condition has to be set for $u = 0$ in Eq. (3.3.2).

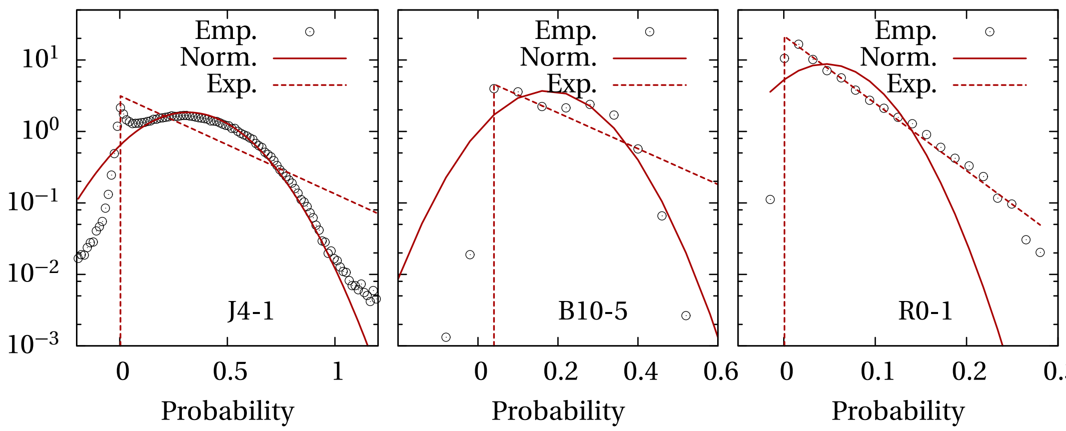

Figure 4.11: Probability density functions of particle velocities (circles), Gaussian distribution (line) and Exponential distribution (dashed line).

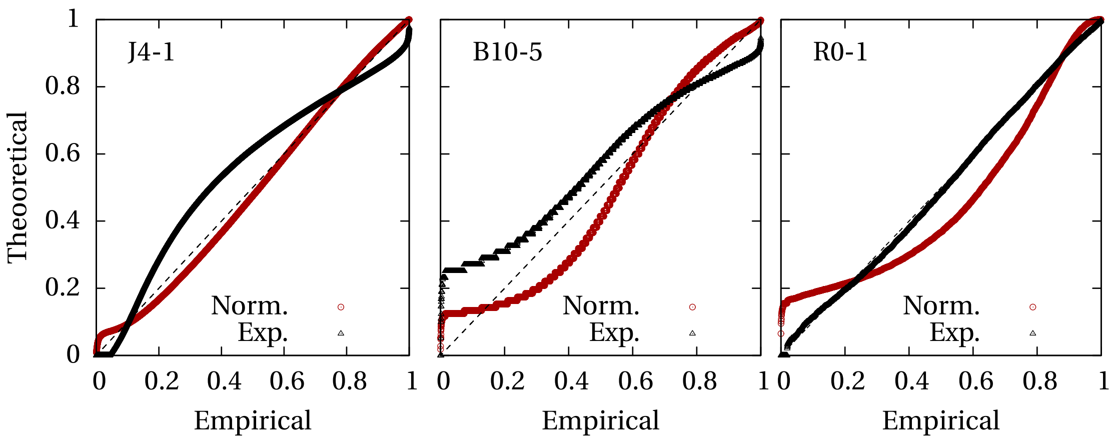

Figure 4.12: P-P plots for normal and exponentially distributed particle velocities.

P-P plots presented in Fig. 4.12. Meanwhile, experiments J and B concern relatively large particles (large Stokes number) while experiment R involves sand (low Stokes number). This may explain the difference in behaviour during particle flights: large particles have a slow response time to turbulent flow perturbations while small particles instantaneously adapt their velocity to flow velocity fluctuations. I compare the theoretical MSD against experiments in Fig. 4.13. In all experiments, the dependence on t^2 at short time is retrieved, confirming the ballistic limit of particle trajectories. At long time scales, there are not long enough trajectories to compute a correct average and the MSD diverges. Despite this, a diffusive limit is observed in most experiments at intermediate times. At these scales, the MSD increases as $2Dt$. By adjusting the two parameters $(\zeta, k_B T)$ of expression (3.3.5) to match the experimental data, the diffusivity $D = k_B T/\zeta$ and the relaxation time $t_r = m/\zeta$ can be obtained (see Table 4.2).

The relaxation time takes values between 0.1 and 0.5 s, while diffusivity ranges from 1.89 cm^2.s^{-1}

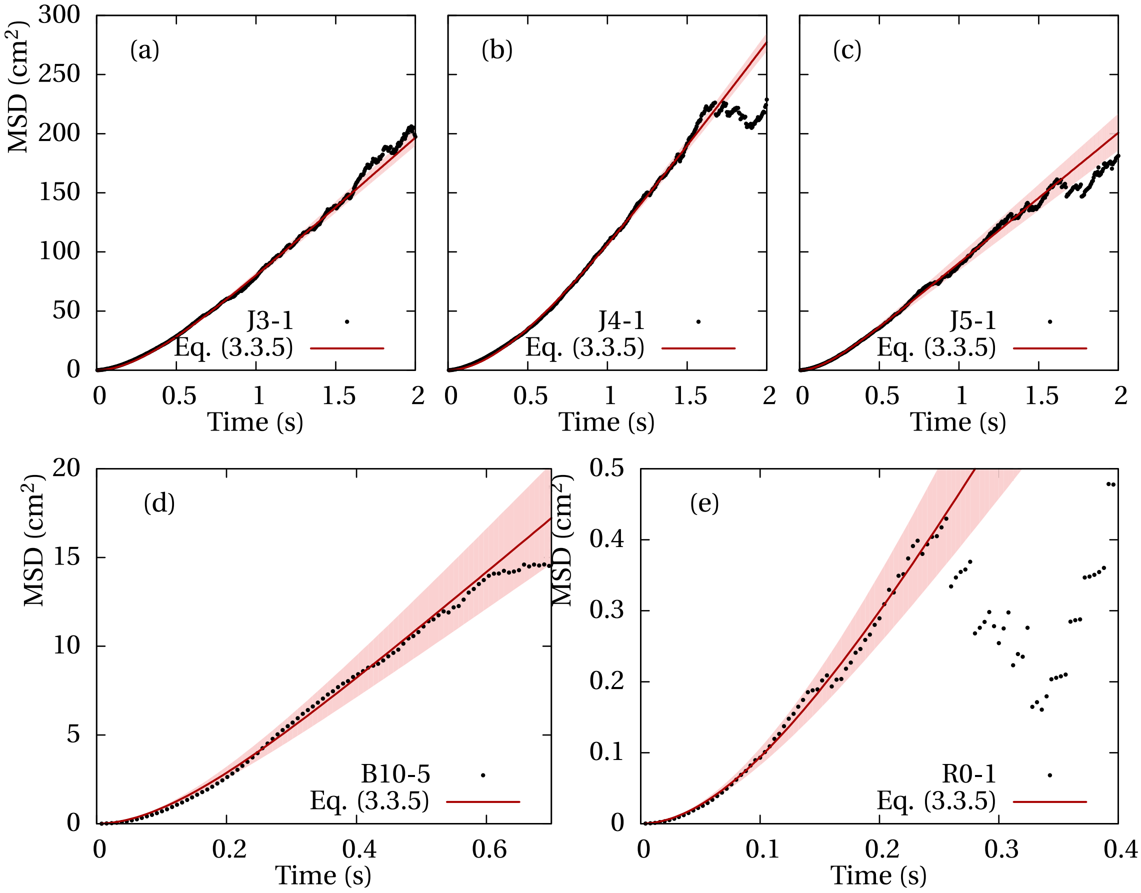

Figure 4.13: Mean squared displacement of particles as a function of time (points) and theoretical prediction (line).

for experiment R up to 90 $cm^2.s^{-1}$ for experiment J. This indicates that diffusivity may be a function of particle size and velocity.

For each experiment, I also reported the equivalent Stokes relaxation time (i.e., $t_r^S = m/(3\pi\mu_f d_{50})$. In experiments B and J, the latter is of the order of a few seconds. The experimental MSD suggests that the relaxation time of particles t_r is ten times smaller than the Stokes relaxation time. This suggests that, in addition to the flow drag, other forces modifies strongly the particle trajectory (collisions, for instance) on shorter time scales. Conversely, for experiment R, the Stokes relaxation time is one order of magnitude smaller than the measured t_r. In this case, we could argue that the role of turbulence is predominant. Indeed, as particles of experiment R reach extremely quickly the velocity of the flow region where they are located, their relaxation time is conditioned by the life time of turbulent eddies.

Another interesting comparison can be made between $k_B T/\zeta$, obtained from the asymptotic tangent to the MSD curve, and $\sigma_u^2 t_r$. We found that, theoretically, $k_B T/\zeta = \sigma_u^2 t_r$ [3]. In most

3. This result states the fluctuation-dissipation argument of Brownian motion, e.g. the viscous dissipation by

experiments, $\sigma_u^2 t_r$ appears to be 2 to 4 times bigger than the value obtained for $k_B T/\zeta$. Nevertheless, they are of the same order of magnitude, so that, as a first approximation, the Langevin model (3.3.1)–(3.3.2) may be considered to be a rough approximation of the particle transport process.

Recall that three independent phases of bed load particle motions—namely entrainment, deposition, and transport—are distinguished in the models presented in chapter III. All of these phases are envisioned as simple random processes acting on specific time scales. Among them, the transport and deposition of particles could be independently quantified with the particle trajectory samples. The only processes that can not be estimated directly with the particle trajectory samples are the entrainment and the collective entrainment rates (respectively λ and μ). Indeed, the two processes are not strictly differentiable physically, so it is not possible to determine their rates independently. The entrainment and collective entrainment rates are thus left as free parameters for the moment. The stochastic models presented previously can provide a way to estimate them.

4 Statistics of the bed load flux

In this section, we compare the experimental time series of volume and surface average bed load fluxes to Ancey *et al.*'s [2008] original model.

4.1 Volume average bed load flux

Theoretical predictions

In the following, I show how the distribution of the volume average particle flux can be derived from Ancey *et al.*'s [2008] model together with the particle transport process hypothesised in chapter III section 3.1. The probability distribution of the volume average particle flux was defined as

$$q_s(t;\mathcal{V}) = \frac{v_s}{\Delta x} \sum_{i=1}^{N(t)} u_i, \tag{4.4.1}$$

where both $N(t)$ and u_i are random variables.

Recall that in the steady state limit $t \to \infty$, the model that was proposed for particle transport leads to particle velocities normally distributed with mean $\langle u \rangle$ and standard deviation σ_u. The probability density function of the sum of k independent [4] random variables drawn from

the drag and the random collisions are linked to the velocity fluctuations of particles.

4. Independence is a reasonable assumption when transport rates are low. It is more questionable for interme-

the normal distribution is also normally distributed:

$$\sum_{i=1}^{k} u_i \sim \mathcal{N}(k\langle u\rangle, k\sigma_u^2). \tag{4.4.2}$$

Thus, the probability density function of the volume average solid flux is

$$P_{q_s}(q_s) = P_s(0)\delta(q_s) + \sum_{k=1}^{\infty} P_s(k)\frac{1}{\sigma_u\sqrt{2k\pi}}\exp\left(-\frac{(q_s\Delta x/v_s - k\langle u\rangle)^2}{2k\sigma_u^2}\right), \tag{4.4.3}$$

where $P_s(k)$ is given by (3.2.5) if $\mu > 0$ and (3.2.8) if $\mu = 0$.

Note that the probability density function of q_s is discontinuous at $q_s = 0$: there is a finite probability density $P_s(0)$ that no particle moves in the observation window, and thus that the volume average particle flux is zero. In the case where there is at least one moving particle in the observation window, P_{q_s} jumps to another finite value. Note that, as I did not exclude the probability for particles to move backward, the flux may occasionally take negative values (Fig. 4.14(a)).

Different solutions are found for P_{q_s} when considering a different particle transport model. For instance, u_i is sometimes found to follow an exponential distribution of mean $\langle u\rangle$ [Lajeunesse *et al.*, 2010; Roseberry *et al.*, 2012]. In that case, the sum of k exponential distribution is the Erlang distribution with parameter $(k, \langle u\rangle)$ so that:

$$P_{q_s}(q_s) = P_s(0)\delta(q_s) + \sum_{k=1}^{\infty} P_s(k)\frac{\langle u\rangle^k (q_s\Delta x/v_s)^{k-1} e^{-\langle u\rangle q_s\Delta x/v_s}}{\Gamma(k)}. \tag{4.4.4}$$

Hamamori [1962] is credited with the first attempt to derive the probability distribution for the sediment transport rate. He considered that bed load transport rate fluctuations arise from the migration of bedforms. He found that the probability density function of the bed load flux is

$$P(q_s) = \frac{1}{4\langle q_s\rangle}\log\left(4\frac{\langle q_s\rangle}{q_s}\right), \tag{4.4.5}$$

which implies that the fluctuations are bounded ($0 < q_s < 4\langle q_s\rangle$). More recently, Turowski [2010] used a two-parameter distribution derived from the normal distribution and called the

diate transport rates, for which interactions between moving particles and disturbance of flow velocity profile are not negligible and create correlations between particle velocities.

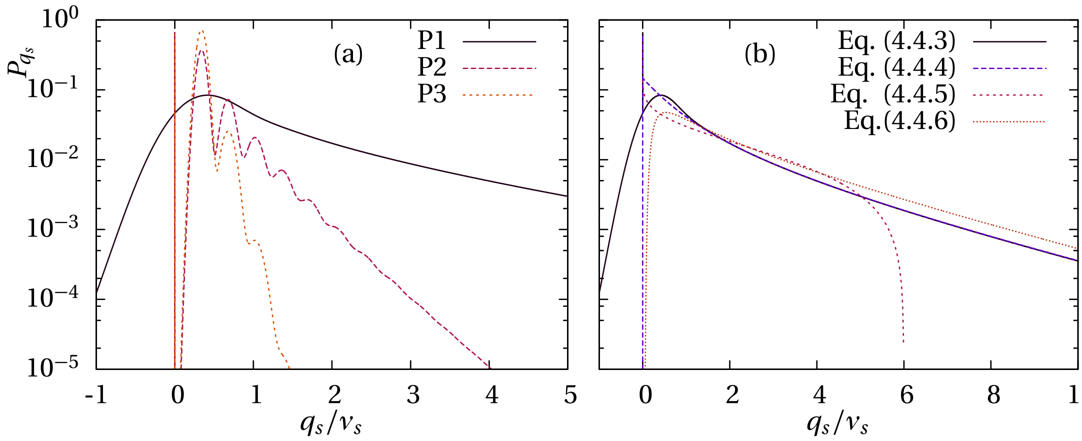

Figure 4.14: (a) Theoretical probability density function of the bed load flux for various parameters. Constant parameters are $\Delta x = 0.1$ m, $\langle u \rangle = 0.3$ m.s^{-1}, $\lambda = 1$ particles.m^{-1}s^{-1}. Case P1: $\sigma = 2$ s^{-1}, $\mu = 1.8$ s^{-1}, $\sigma_u = 0.3$ m.s^{-1}. Case P2: $\sigma = 2$ s^{-1}, $\mu = 1.0$ s^{-1}, $\sigma_u = 0.05$ m.s^{-1}. Case P3: $\sigma = 1$ s^{-1}, $\mu = 0$ s^{-1}, $\sigma_u = 0.05$ m.s^{-1}. (b) Comparison of equations (4.4.3) and (4.4.4) in the case of P1 parameters to equations (4.4.5) ($\langle q_s/v_s \rangle = 1.5$ particles.s^{-1}) and (4.4.6) ($\alpha = 1.5$ particles.s^{-1} and $1/\beta = 1$ particles.s^{-1}).

Birnbaum-Saunders distribution

$$P(q_s) = \frac{q_s + \alpha}{2\beta q_s \sqrt{2\pi\alpha q_s}} \exp\left[-\frac{(q_s-\alpha)^2}{2\alpha\beta^2 q_s}\right], \tag{4.4.6}$$

with α and β two parameters. Figure 4.14(b) shows a comparison between probability distributions (4.4.3), (4.4.4), (4.4.5), (4.4.6) for a particular case. As the fluctuations are bounded, Hamamori's relation is unable to capture the exponential tail of the distribution and tends to overestimate the bed load transport rate significantly compared to (4.4.3) in the limit of $q_s \to 0$. This latter shortcoming is also observed for the Birnbaum-Saunders distribution, but the tail behaviour is consistent with the macroscopic model predictions (Eq. (4.4.3)).

The average and the variance of a random sum of random variables is well-known [Ross, 2006]. The former is

$$\mathrm{Mean}[q_s(\Delta x)] = \frac{v_s}{\Delta x} \langle N \rangle \langle u \rangle = v_s \frac{\lambda}{\sigma - \mu} \langle u \rangle . \tag{4.4.7}$$

It is interesting to compare Eq. (4.4.7) to the entrainment form of the solid flux (2.2.3). Indeed, λ has been defined as the mean entrainment rate of particles per meter of length while $1/\sigma = t_\sigma$ is the mean particle flight time. Thus $t_\sigma \langle u \rangle$ is the mean particle flight distance and Eq. (4.4.7) and Eq. (2.2.3) are equivalent when $\mu = 0$. Indeed, Einstein [1937] did not consider the importance of collective entrainment in his early results.

The variance is

$$\mathrm{Var}[q_s(\Delta x)] = \frac{v_s^2}{\Delta x^2}\left(\langle N\rangle \mathrm{Var}[u] + \langle u\rangle^2 \mathrm{Var}[N]\right) \tag{4.4.8}$$

$$= \frac{v_s^2}{\Delta x}\frac{\lambda}{\sigma-\mu}\left(\sigma_u^2 + \langle u\rangle^2 \frac{\sigma}{\sigma-\mu}\right). \tag{4.4.9}$$

The latter expression shows that the fluctuations of the bed load flux are due to fluctuations both in particle velocity and in particle number.

Comparison with experiments J

In the following, I compare the theoretical expression (4.4.3) to experiments J [5]. To that end, the parameters r and p of a negative binomial distribution are estimated from the data of the number of moving particles in a window of length $\Delta x = 0.3$ m. According to the stochastic model, the parameters r and p are respectively $\lambda\Delta x/\mu$ and $1-\mu/\sigma$ (Eq. (3.2.5)). As σ has been measured independently (see section 3), λ and μ can also be defined uniquely. Once the probability distribution of $N(t)$ as well as the average and the variance of particle velocity are known (see table 4.2), the computation of (4.4.3) is possible.

The theoretical probability density function is found to describe fairly well the experimental data (Fig. 4.15) for small to moderate solid flux. This shows that the assumption of statistical independence between u_i and N, that allowed us to derive (3.2.5), is realistic enough in experiments J for moderate fluxes. In contrast, for higher particle fluxes, eq. (4.4.3) overestimates the empirical frequency. This can be explained by the fact that when a lot of particles move together, their velocities decrease because of mutual energy dissipation. In this case, the number of moving particles and their velocities are not independent and expression (4.4.3) does not hold anymore.

In both experiments and theory, the value $q_s/v_s = 0$ stands out from the probability density function. In other words, there is a unusually large probability that the bed load flux is null. This suggests that, close to incipient motion conditions, the bed load flux is highly intermittent.

4.2 Surface average bed load flux

In section 4.1, the distribution function of the volume average bed load flux was computed. Moreover, in section 2.3, I have shown that the volume average flux is equivalent to the surface average flux when the size of the observation window tends to zero. However, Ancey *et al.*'s [2008] macroscopic model assumes that $\mathscr{V}$ is large enough for the flux at its boundaries to be ignored. Thus, the limit $\Delta x \to 0$ is proscribed and the macroscopic model cannot be compared

5. The comparison to experiments B and R is doomed to failure because of the very low data resolution.

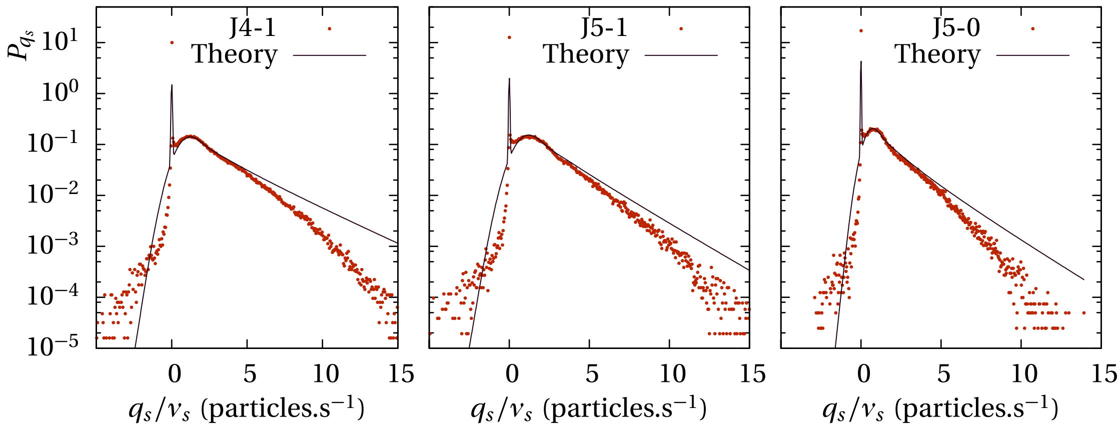

Figure 4.15: Probability distribution of the particle flux of experiments J and theoretical expression (4.4.3). Estimated parameters are (J3-1) $r = 40, p = 0.56$; (J4-1) $r = 41, p = 0.70$; (J5-1) $r = 42, p = 0.36$.

with experiments which only measure bed load transport in time, such as experiments H.

To overcome this limitation, I suppose that another exchange modifying the number of moving particle in the window exists. This new event is meant to represent the flux of particle in and out of the window and is called a migration process [6]. In a manner similar to the other exchanges, the migration process is supposed memoryless with an average rate ε [s^{-1}]. In other words, the probability that a particle emigrates out of the observation window in a small time interval Δt is

$$P(n \to n-1, \Delta t | t) = \varepsilon N(t)\Delta t + o(\Delta t). \tag{4.4.10}$$

Equivalently, the probability that a particle immigrates into the window in a small time interval Δt is

$$P(n \to n+1, \Delta t | t) = \varepsilon \langle N \rangle \Delta t + o(\Delta t). \tag{4.4.11}$$

The major statistical difference between the immigration process and the emigration process is that the former is supposed to be independent of $N(t)$ while the latter has a rate that explicitly depends on the instantaneous value of $N(t)$. Note that the immigration and the emigration process cancel on average, so that the average flux across window boundaries is null [Ancey *et al.*, 2008].

A rough estimate gives $\varepsilon \propto \langle u \rangle / \Delta x$. Indeed, the larger the particle velocity and the smaller the

6. Note that in the original Ancey *et al.*'s [2008] model, migration events were also considered though their statistics were not studied

window size, the higher the probability that a moving particle emigrates out of the window. The corresponding migration time scale is thus $t_\varepsilon = \varepsilon^{-1} \propto \Delta x / \langle u \rangle$.

The emigration process defines a discrete point process comparable to that represented in Fig. 4.7(c). This type of process is also called a renewal process and is found in many situations, such as queuing, traffic, machine failure rates [Bhat, 2008]... One of the principal characteristics of such process is the inter-arrival time T[s]; that is the waiting time between two emigration events. An *instantaneous* measure of the bed load flux at the boundary can be obtain by inverting the inter-arrival time:

$$q_s \sim v_s \frac{1}{T} \quad [\mathrm{m}^3\mathrm{s}^{-1}]. \tag{4.4.12}$$

Probability distribution of particle arrival time

In appendix B.3, I show how to derive the probability density function f_T of T based on the macroscopic model, augmented by the migration process. For $t > 0$, it reads

$$\begin{aligned} f_T(t) &= \varepsilon (z_1 - z_2)^{\lambda'/\mu} \left(\frac{\alpha - \mu}{A(t) - B(t)} \right)^{\lambda'/\mu + 1} e^{-\lambda'(1-z_2)t} \times \\ & \left\{ \frac{(\lambda'/\mu + 1)\, B(t)}{A(t) - B(t)} \left[(1-z_2) e^{-\mu(z_1 - z_2)t} + z_1 - 1 \right] + e^{-\mu(z_1-z_2)t} - 1 \right\}, \end{aligned} \tag{4.4.13}$$

where

$$\begin{aligned} A(t) &= z_2(\mu z_1 - \alpha) e^{-\mu(z_1 - z_2)t} + z_1(\alpha - \mu z_2) \\ B(t) &= (\mu z_1 - \alpha) e^{-\mu(z_1-z_2)t} + (\alpha - \mu z_2) \\ z_1 &= (\alpha + \mu)\left(1 + \sqrt{1-\epsilon}\right)/2\mu \\ z_2 &= (\alpha + \mu)\left(1 - \sqrt{1-\epsilon}\right)/2\mu, \end{aligned} \tag{4.4.14}$$

with $\lambda' = \lambda \Delta x + \varepsilon \langle N \rangle$, $\epsilon = 4\sigma\mu/(\alpha+\mu)^2$ and $\alpha = \varepsilon + \sigma$.

Equation (4.4.13) provides a fully theoretical link between the macroscopic Markov model defined on an observation window and the experimental probability density function of the inter-arrival time obtained at a precise location, such as in experiments H.

To check the validity of (4.4.13), Monte Carlo simulations of the birth-death process were performed with the Stochastic Simulation Algorithm (SSA) described in Gillespie [1977]. This algorithm is able to give exact realisations of any Markov processes. To do so, it ingeniously uses the memoryless property of these processes. Below is shown an example of a Matlab implementation of Gillespie's [1977] algorithm :

```
%%%%%%%%%%%%%%%%%%%%%%%%%%%%%%%%%%%%%%%%%%%%%
% SSA Algorithm - Example of implementation %
%%%%%%%%%%%%%%%%%%%%%%%%%%%%%%%%%%%%%%%%%%%%%

 Tlim=10; %Simulation time
 lc=0.01; %Entrainment and immigration rate
 mc=1.3; %Collective entrainment rate
 sc=1.0; % Deposition rate
 vout=0.5; % Emigration rate

 a=zeros(3,1); %Reaction rates
 v=zeros(3,1); %Reaction vectors

 %Initialisation
 N=0;
 a(1)=lc+N*mc;
 a(2)=sc*N;
 a(3)=vout*N;
 v(1)=1;
 v(2)=-1;
 v(3)=-1;
 t=0;

   while (t<Tlim)   % SSA loop
        asum=sum(a);
        j=find(cumsum(a)>rand*asum); % Choose next reaction
        k=j(1);
        dt=log(1/rand)/asum; %Sample reaction time
        N=N+v(k); %Update particle number
        t=t+dt; %Update time
        % Update reaction rates according to new value of N
        a(1)=lc+N*mc;
        a(2)=sc*N;
        a(3)=vout*N;
   end

%%%%%%%%%%%%%%%%%%%%%%%%%%%%%%%%%%%%%%%%%%%%%
```

Simulations show perfect agreement with equation (4.4.13), as can be seen in Fig. 4.16(a). As seen on the same figure, the theoretical probability density function of T shows, under certain conditions, a bimodal shape that differs considerably from exponential [7]. This bimodal distribution comes from the difference of time scales between the (slow) entrainment of particles and (fast) collective entrainment.

To clarify this, I plotted in Fig. 4.16(a) the effect of the parameter λ' (e.g., entrainment rate and immigration rate) on the shape of the probability density function of T. When $\lambda' \to 0$, with other parameters held constant, the time scales clearly separate. On the contrary, when λ' increases, no further significant scale separation can be seen and the probability density function of T has a simpler exponential behaviour.

The presence of collective entrainment is also a necessary condition to observe a separation of

7. A memoryless renewal process has inter-arrival time of events exponentially distributed.

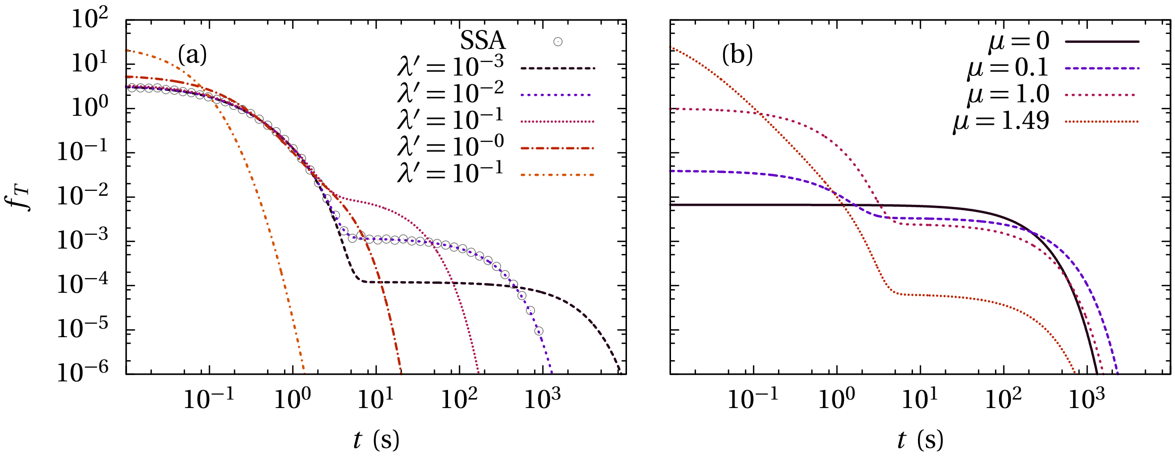

Figure 4.16: Theoretical probability density function (Eq. (4.4.13)) for the waiting time between particle arrivals. Constant parameters are $\sigma = 1.0$ s^{-1} and $\varepsilon = 0.5$ s^{-1}. (a) Effect of the entrainment rate λ' [particles.s^{-1}] with $\mu = 1.3$ s^{-1}. Comparison with a Monte Carlo simulation (for $\lambda' = 10^{-2}$ particles.s^{-1}). (b) Effect of the collective entrainment rate μ [s^{-1}] with $\lambda' = 10^{-2}$ particles.s^{-1}.

time scales in the probability density function of T. Indeed, even if the emigration rate is large compared to the entrainment rate, so that two distinct time scales exist (the fast transport of particles against the slow entrainment process), no separation is observed on the probability density function of T when $\mu \to 0$ (Fig. 4.16(b)). This can be explained by the fact that the emigration process is governed entirely by the slow entrainment (no particle leaves if no particle moves). In the case $\mu = 0$, the probability density function of T becomes exponential with parameter $\alpha/(\lambda'\varepsilon)$. However, when collective entrainment is considered ($\mu > 0$), the separation of time scales is possible due to the occurrence of fast and intense collective bursts in particle entrainment which occur together with the relatively slow entrainment of particles.

Comparison with experiments H

Experiments H were specially designed to record each particle arrival time. Thus, the experimental density probability function of inter-arrival times is available in these experiment.

Expression (4.4.13) can be used to fit the set of parameters $(\lambda', \gamma, \sigma, \mu)$ to the experimental probability density function (Fig. 4.17). The value of λ' governs the long time scales and a decrease in λ' shifts the probability density function tail to the right. The $\alpha - \mu$ value controls the short time scales, so that a decrease shifts the left plateau of the probability density function to shorter times.

I assumed that parameters σ and μ remained constant for all three H experiments, supposing that only the entrainment rate λ' increased significantly with the bottom shear stress. This is justified by the fact that, according to traditional bed load formulas, λ' is proportional to τ

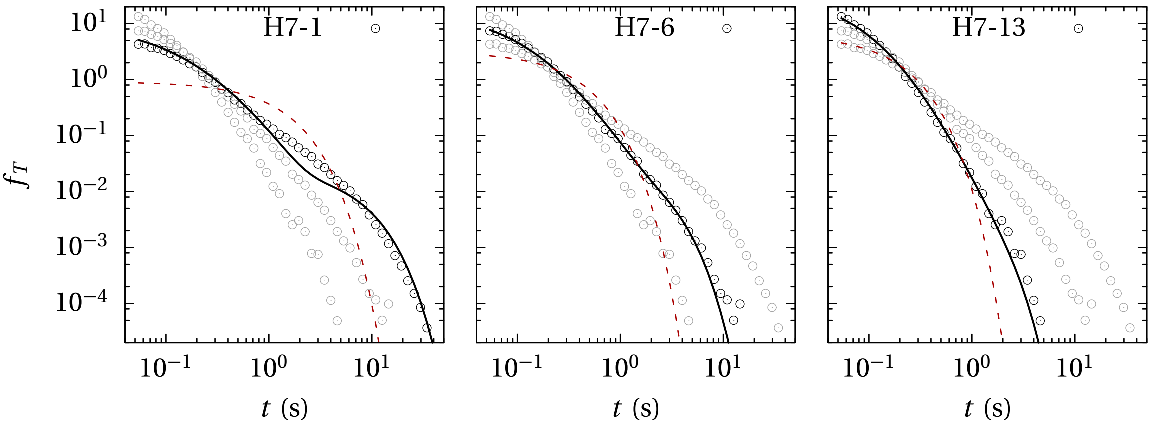

Figure 4.17: Experimental and theoretical probability density functions of the inter-arrival time of particles for the three experiments H (dark and light circles). Expression (4.4.13) (dark line) and exponential fit (red dashed line). Fitted parameters are: $\lambda'(\text{H7-1}) = 0.56$, $\lambda'(\text{H7-6}) = 2.10$ and $\lambda'(\text{H7-13}) = 5.75$ particles.s^{-1}. Fixed parameters are $\mu = 2.37$ s^{-1}, $\sigma = 2.2$ s^{-1} and $\varepsilon = 0.3$ s^{-1}.

and ε to $\sqrt{\tau}$, while σ and μ have not been reported to change much with bottom shear stress [Ancey *et al.*, 2008]. Fitted values of λ' are given in Fig. 4.17. Good agreement is found for each of the three experimental probability density functions, both short- and long-time scales being well described.

As predicted by the theory, when the Shields stress increases (and thus mainly the entrainment rate λ'), the experimental probability density function tends to the exponential distribution. In other words, the collective entrainment effect is "hidden" by the too frequent entrainment of particles by the fluid flow.

Note that the temporal statistics derived above for the emigration process could be similarly derived for other processes, for instance for the deposition process. The question would be now: "What is the average time between two particle depositions ? What is the probability distribution of such time?". There is no doubt that the latter will have roughly the same form as the probability function of T (eq. (4.4.13)), with the same phenomenon of time scale separation.

It is worth recognising that the complexity of (4.4.13) makes it of little use in practice. Nevertheless, the knowledge of the statistics of the particle arrival time has two advantages: (i) it provides a link between spatially defined quantities (e.g., $N(t)$), often left undetermined experimentally, and temporal measurements that are easier to obtained in practice, and (ii) it proves that the emigration process has a complex behaviour and is not memoryless [8].

8. In a memoryless case, the inter arrival time would have been exponentially distributed.

5 Fluctuations of the particle activity

The local model (3.3.19) allows us to study the behaviour of the spatio-temporal fluctuations of particle activity. As shown in section 2.3, two types of averages can be used to study the statistics of particle trajectories, namely volume average and time averages. Both of them are compared to the theoretical predictions.

5.1 Spatial average

Let us consider the number of moving particles in a window of length L at a given time t:

$$N(L,t) = \int_L \gamma(x,t)\mathrm{d}x. \tag{4.5.1}$$

The ensemble average of this number is [9]

$$\mathrm{Mean}[N(L,t)] = \left\langle \int_L \gamma(x,t)\mathrm{d}x \right\rangle = \int_L \langle \gamma(x,t) \rangle \,\mathrm{d}x = \langle \gamma \rangle_s L, \tag{4.5.2}$$

while the expected variance of this number (e.g., the variance of the sample mean) is defined by

$$\begin{aligned} \mathrm{Var}[N(L,t)] &= \left\langle \int_L \gamma(x,t)\mathrm{d}x \int_L \gamma(x',t)\mathrm{d}x' \right\rangle - \left\langle \int_L \gamma(x,t)\mathrm{d}x \right\rangle^2 \\ &= \int_L \int_L \langle \gamma(x,t), \gamma(x',t) \rangle \,\mathrm{d}x \;\mathrm{d}x'. \end{aligned} \tag{4.5.3}$$

Introducing Eq. (3.3.33) into Eq. (4.5.3) and integrating it (see appendix B.4):

$$\mathrm{Var}[N(L,t)] = \langle \gamma \rangle_s L + \langle \gamma \rangle_s \ell_c \frac{\mu}{\sigma - \mu} \left(L/\ell_c + \mathrm{e}^{-L/\ell_c} - 1 \right). \tag{4.5.4}$$

Eq. (4.5.4) shows the dependence of the variance of $N(L,t)$ on the length L of the sampling window. Let us define the dispersion index $I(L)$ as the ratio of the variance over the mean

$$I(\tilde{L}) = \frac{\mathrm{Var}[N(\tilde{L},t)]}{\mathrm{Mean}[N(\tilde{L},t)]} = 1 + \frac{\mu}{\sigma - \mu} \left(1 + \frac{\mathrm{e}^{-\tilde{L}} - 1}{\tilde{L}} \right), \tag{4.5.5}$$

9. Here, the ensemble average of a quantity summed over a volume is computed, which is equivalent to volume averaging in experiments.

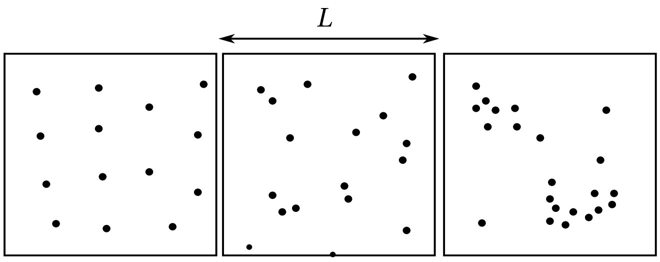

Figure 4.18: Example of a realization of point positions in a two-dimensional space depending on the value of the dispersion index $I(x)$. Here, x can be interpreted as the length of the box.

with $\tilde{L} = L/\ell_c$.

In a manner similar to the K-function introduced in section 3.5, the dispersion index characterizes the relative positions of particles. Three classes are generally distinguished, depending on the value of I: under-dispersed processes for $I < 1$; purely random processes (or Poisson process) when $I = 1$; and over-dispersed or clustered processes when $I > 1$ (Fig. 4.18).

In our model, the dispersion index is shown to grow from 1, when the window is small, to the constant value $1 + \mu/(\sigma - \mu)$, as the window length tends to infinity (Fig. 4.19). In other words, depending on the observation scale, the process exhibits a different statistical behaviour.

When L tends to 0, $I(L)$ tends to one, so that the variance and the mean of $N(L, t)$ are equal. Thus, in the small scale limit, $N(L, t)$ tends to a Poisson process. This is mathematically explained by the presence of the Dirac delta function in the spatial correlation function (3.3.33). For decreasing values of L, a limit will be reached when most of the sampling windows usually contain no particles, or rarely one particle. This limiting behaviour of $N(L, t)$ can be seen as representative of a Bernoulli process (e.g., $N(L, t) = 1$ with probability $\langle\gamma\rangle_s L$ and $N(L, t) = 0$ with probability $1 - \langle\gamma\rangle_s L$). Within the limit of a small probability of occurrence ($\langle\gamma\rangle_s L \to 0$), this approximates a Poisson process.

On the contrary, when $L \to \infty$, I reaches a constant value $I(\infty)$. Note that $I(\infty) > 1$ if $\mu > 0$, so that the variance of $N(L, t)$ is now greater than its mean. Thus, for larger scales, when $\mu > 0$, $N(L, t)$ cannot be described by a Poisson process. Moving particles are expected to form clusters during their motion when collective entrainment is considered (Fig. 4.18).

The experimental dispersion indices are presented in Fig. 4.20. As expected, the dispersion index changes through spatial scales. From a Poisson type process (the mean of $N(\tilde{L}, t)$ equals its variance) at small scales ($\tilde{L} \to 0$), $I(\tilde{L})$ continuously increases with increasing scales (Fig. 4.20(a)–(d)). The dispersion index of experiment R (Fig. 4.20(e)) follows a slightly different evolution, since it drops at scales greater than 5 cm.

The peculiar behaviour of experiment R might be explained by the relatively short measurement window ($\sim$ 8 cm) and the relatively short acquisition time (0.4 s, 100 frames) of

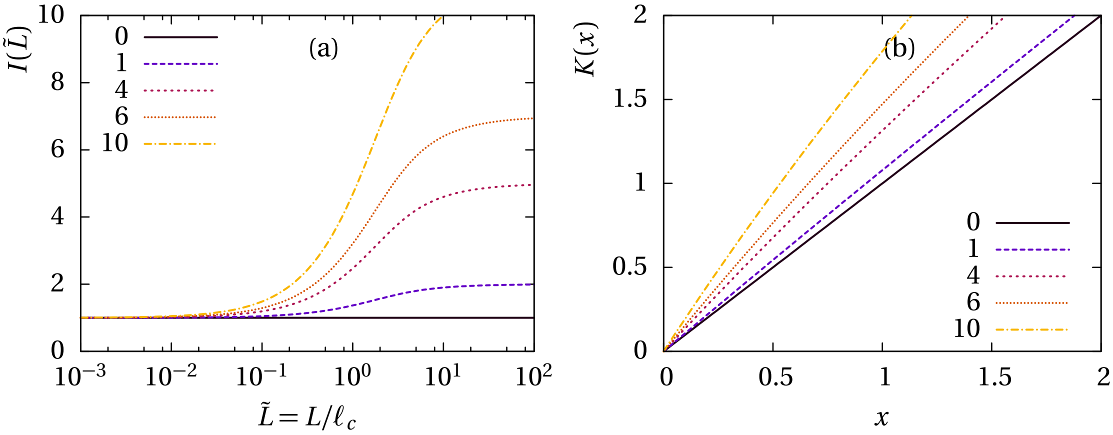

Figure 4.19: Spatial fluctuations in the number of moving particles. (a) Dispersion index (Eq. (4.5.5)) for different $\mu/(\sigma-\mu)$ values. (b) K-function (Eq. (4.5.5)) for different $\mu/(\sigma-\mu)$ values with $\langle\gamma\rangle_s = 5$ particles.m $^{-1}$ and $\ell_c = 2$ m hold constant.

experiment R which are likely to yield biased estimates of the dispersion index.

One striking feature of the experimental dispersion index that appears only in experiment B is the slight decrease below unity for observation windows of the order of the particle diameter (detail of Fig. 4.20(d)). This phenomenon results from negative values in the correlation function at those scales and cannot be described by the local model. Indeed the theoretical spatial correlation function (3.3.33) is strictly greater than zero so that the variance is expected to grow monotonically. The presence of negative values in the experimental correlation function is explained by the finite particle diameter. Recall that B experiments took place in a one-dimensional channel whose width equals the particle diameter. Thus, there is less probability [10] of finding two particles separated by a distance smaller than the particle diameter. This results in anti-correlation at scales close to the particle diameter ($L \sim d_{50}$). This effect does not appear in J and R experiments, as moving particles are summed also over the perpendicular direction $\vec{y}$ and thus the distances between particles centroids are not bounded by d_{50}.

The dispersion index of experiment R indicates that spatial correlations occur even for a gently sloping bed under subcritical flow conditions. Recall that collective entrainment is the only cause of spatial correlation in the local model. In experiment R, that is for small particle diameters and gentle slopes, correlations are likely to originate from entrainment by coherent turbulent structures rather than from direct particle-particle interactions as the Stokes number of particles is fairly low (see the discussion about the role played by the particle Stokes number during viscous particle collisions in chapter II). This may also explain the fact that the dispersion index drops for scales larger than $\ell_c = 5.3$ cm: the turbulent sweeps

10. I used the term "less probability" and not "zero probability" since the moving particles in an observation window are summed over the whole water depth (z direction), so that it is still possible that the distance separating two moving particles (in the x direction) may be less than the particle diameter.

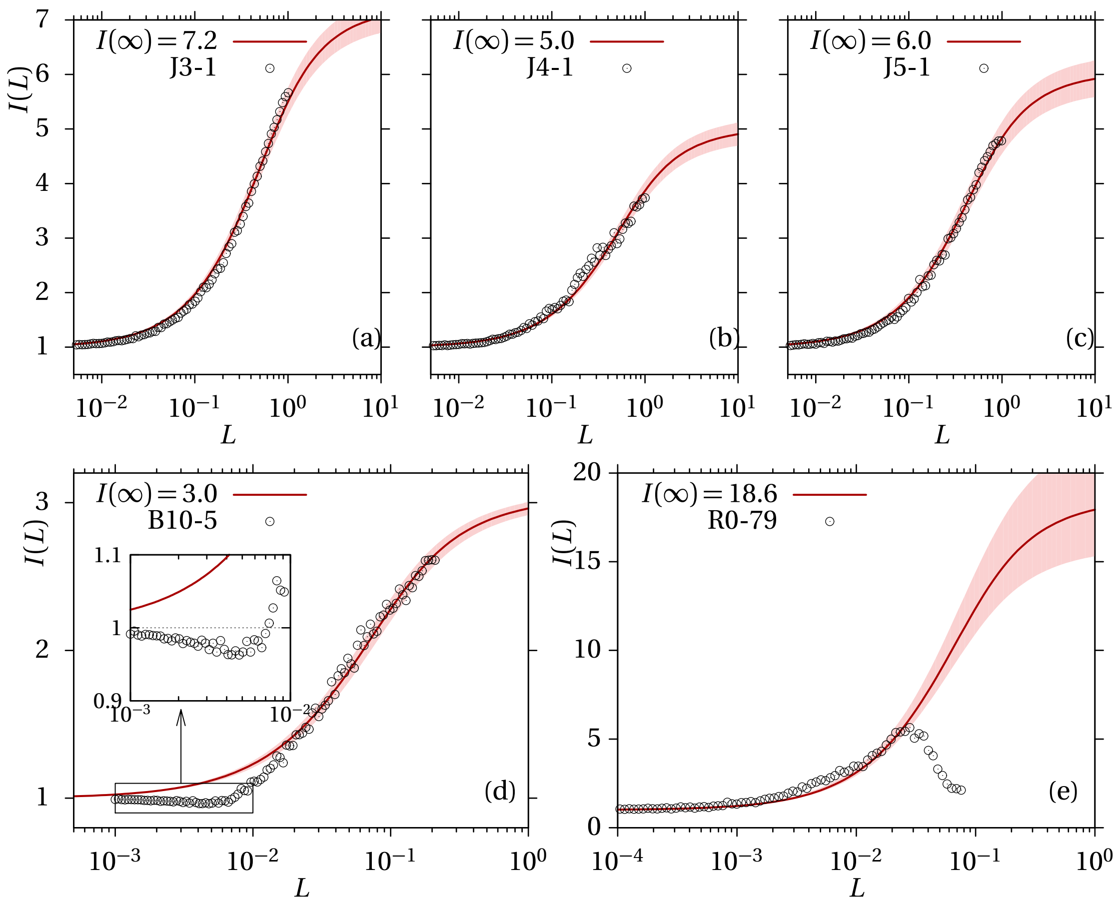

Figure 4.20: Experimental dispersion index for experiments B,R and J and comparison with theoretical predictions (Eq. (4.5.5))

involved in particle entrainment have a characteristic length and occur between turbulent ejections in a pseudo-periodical way. Thus, particles may appear under-dispersed at scales equal to the eddies lengths.

Another noteworthy feature of experiment R is the relative magnitude of the fluctuations: up to 15 times the mean particle activity. Although the B experiments were carried out on a steeper bed, their fluctuations did not exceed 3 times the mean particle activity. A reasonable explanation might be that particle diameters in the R experiment were much smaller than in B or J experiments. As a consequence, turbulent eddies entrain more particles at the same time, making thus collective effects appear stronger.

Equation (4.5.5) may be adjusted to match the experimental data by varying the collective entrainment rate (μ). It is worth noting that D and σ have been calibrated independently (see section 3), so that only μ has to be tuned artificially. Despite this, (4.5.5) agrees extremely well with the experimental points. The values of μ are reported in table 4.3.

Unfortunately, the limiting value of the dispersion index $I(\infty)$ is reached for the maximum observation window $\mathscr{L}$ in none of the experiments presented (see table 4.1). Even experiments J —designed specially to achieve this purpose and by far the longest motion-picture data available ($\mathscr{L} \sim 1$ m)— are unable to reach the final plateau. It is still possible to extrapolate the theoretical expression (4.5.5) to predict the behaviour of fluctuations at larger scales and to obtain $I(\infty)$.

Once μ has been obtained, the theoretical K-function can be compared to each experiment. From Fig. 4.21, we can see that the theoretical K-function describes experimental data less accurately than the dispersion index does. This could be explained by the fact that an additional parameter, $\langle\gamma\rangle_s$, is required in Eq. (3.3.35). Thus, if the measure of $\langle\gamma\rangle_s$ is biased (as it can be the case for short trajectory samples), the theoretical K-function may also be biased.

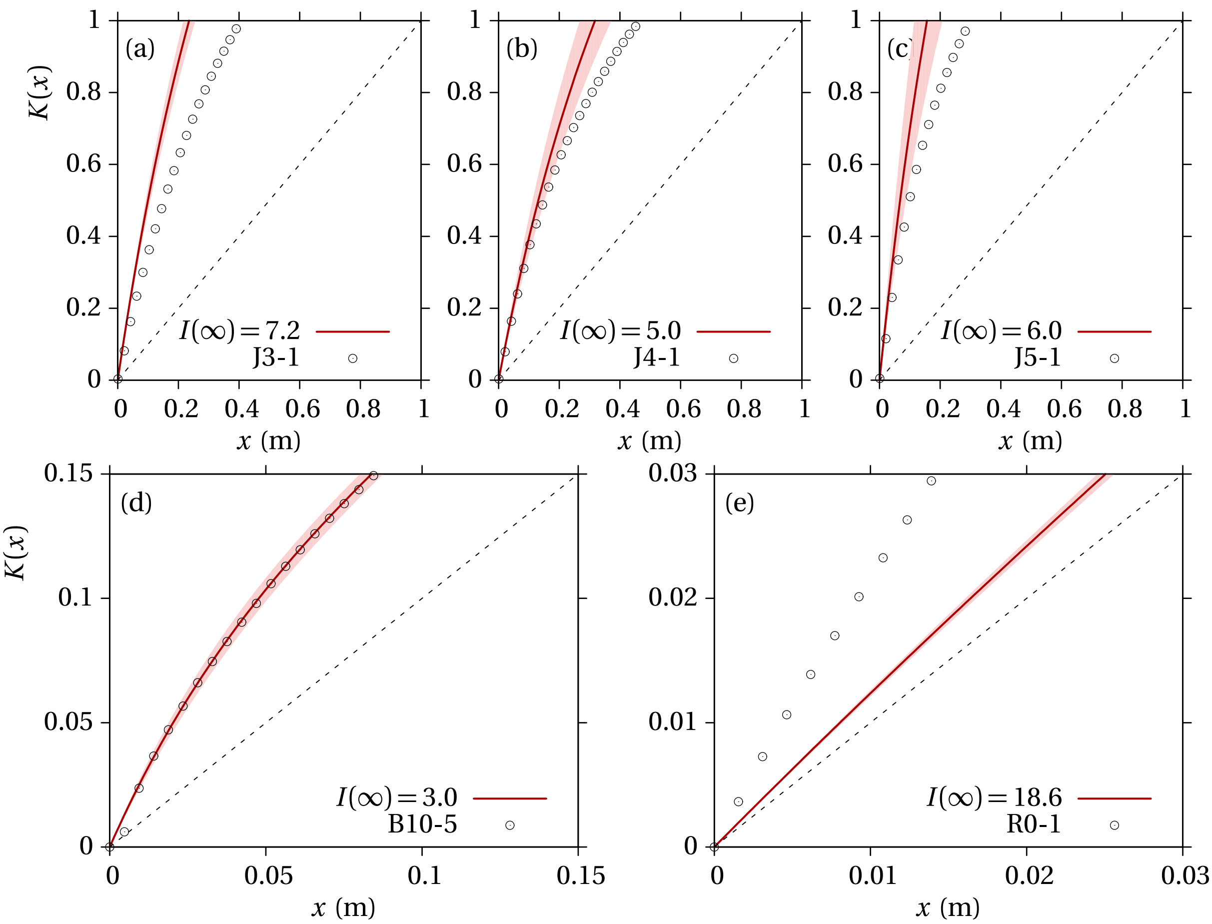

Figure 4.21: Experimental K-function for experiments B,R and J and comparison with theoretical predictions (Eq. (3.3.35)). x units are in meters. The dashed line stands for the Poisson process case $K(x) = x$.

ℓ_c can be calculated from the values of μ, σ and D (Tables 4.2 and 4.3). It takes value from the centimetre (experiments R and B) to the tenth of centimetres (experiment J). Looking at equations (3.3.33) and (4.5.5), ℓ_c defines the scale where approximately[11] 36.8% of the maximum fluctuations above the mean are observed. In other words, to observe at least 95% of the overall fluctuations, scales of the order of $20\ell_c$ should be observed experimentally, that is about 1 m for experiment B and R, and 3 m for experiments J. This length may be considered as the minimum size of the volume for the macroscopic model of Ancey *et al.* [2008] to hold.

In addition to the technological challenge such a long measuring length involves, the experimental flume might need to be even longer to avoid effects from the input and output boundary conditions. The saturation length ℓ_{sat} (see Eq. (3.3.26)) is a good estimator of the length needed for perturbations induced at the boundary to vanish. It is clear that the boundary conditions of experiments B and J, carried out on relatively short flumes (between 0.5 and $10\ell_{sat}$), may give biased results. Moreover, for experimental scales of the order of $20\ell_c$, it is often impossible to insure the spatial homogeneity of the sediment transport. Indeed, the instability of the bed-water interface leads inexorably to the development of bedforms of various wavelengths (from centimetres to hundreds of meters) and thus precludes the assumption of homogeneity in theory.

The local Péclet number can also be calculated with the experimental values of parameters. $\mathscr{P}_e$ is observed to range from 4 (experiment B) to 14 (experiments J), proving the variety of modes of transport in bed load transport. Bed load occurring in experiment B is still strongly diffusive at the correlation length scale while in experiments J, it is mostly advective at this scale.

5.2 Temporal average

Most bed load measurement devices sample bed load temporally [Bunte & Abt, 2005]. For instance, weighting bins [Singh *et al.*, 2009] or geophone sensors [Rickenmann *et al.*, 2012] monitor bed load discharge at a given location over time. In this case, Eq. (4.5.5) cannot be used to test stochastic predictions. Instead, the fluctuations of the mean number of particles that pass through a given location during a time period T is sought:

$$N(x,T) = \langle u \rangle \int_T \gamma(x,t)\mathrm{d}t.$$

The variance of this number is

$$\begin{aligned} \mathrm{Var}[N(x,T)] &= \langle u \rangle^2 \int_T \int_T \langle \gamma(x,t), \gamma(x,t') \rangle \,\mathrm{d}t\ \mathrm{d}t', \\ &= \langle u \rangle^2 \int_T \int_T G(0, t-t')\mathrm{d}t\ \mathrm{d}t'. \end{aligned} \tag{4.5.6}$$

11. More exactly, $(I(\ell_c)-1)/(I(\infty)-1) = e^{-1} = 36.8\%$

	B10-5	R0-79	J3-1	J4-1	J5-1
$\bar{\gamma}$	26.9±*0.6*	1713±*51*	4.56±*0.7*	3.87±*0.4*	2.84± *0.5*
$\bar{u}$	0.170±*0.001*	0.046±*0.001*	0.310±*0.001*	0.300±*0.001*	0.320±*0.001*
σ	2.72±*0.09*	1.85±*0.09*	0.52±*0.03*	0.50±*0.03*	0.56±*0.03*
D	15±*2*	1.5±*0.3*	59±*2*	89± *2*	55± *3*
μ	1.825±*0.020*	1.754±*0.006*	0.447±*0.001*	0.403±*0.002*	0.470±*0.001*
λ	24±*3*	171±*415*	0.33±*0.06*	0.39±*0.05*	0.27±*0.05*
ℓ_c	4.1±*0.3*	3.8±*0.5*	28.7±*0.6*	29.8±*0.7*	24.3±*0.9*
$\mathscr{P}_e$	4.6±*1.1*	12.2±*5*	15.1±*0.8*	10.1±*0.5*	14.1±*1.3*
$I(\infty)$	3.0±*0.2*	18.6±*5*	7.2±*0.5*	5.0±*0.4*	6.0±*0.5*
ℓ_{sat}	20±*6*	47±*23*	434±*33*	303±*22*	345±*45*
t_c	0.24±*0.02*	0.82±*0.2*	0.92±*0.02*	0.99±*0.03*	0.76±*0.03*

Table 4.3: Estimates of local model parameters and 95% confidence intervals. $\bar{\gamma}$ [particle.m^{-1}], average particle activity; $\bar{u}$ [m.s^{-1}], average particle velocity; σ [s^{-1}], deposition rate; D [cm^2.s^{-1}], particle diffusivity; t_r [s] particle velocity relaxation time; λ [particle.m^{-1}.s^{-1}], particle entrainment rate per meter length; μ [s^{-1}], collective entrainment; ℓ_c [cm], correlation length ($\ell_c = \sqrt{D/(\sigma-\mu)}$); $\mathscr{P}_e$ [-] local Péclet number ($\mathscr{P}_e = \ell_c \bar{u}/D$); $I(\infty)$ [-], limiting value of the dispersion index; ℓ_{sat} [cm] saturation length (Eq. (3.3.26)); t_c [s], correlation time in the frozen flow hypothesis.

Unfortunately, this integral is too complex to be calculated analytically. Still, estimates can readily be obtained at large $\mathscr{P}_e$ (for high average particle velocity). In this case, it can be shown that the spatial correlation function of the particle activity is projected on the temporal axis without deformation (the proof is given in appendix A.7). The equivalence between time and space is then given by $t \sim x/\langle u\rangle$. This approximation can be compared to Taylor's frozen-flow hypothesis in turbulent flows with a dominant velocity [Moin, 2009]. This hypothesis relies on the existence of a large mean particle flow which "transport" the spatial particle structures so quickly that they do not change much during their transport. In this hypothesis, the relative particle positions in space would correspond exactly to their relative arrival time at given location, the correlated structures being "frozen".

Thus, the same statistical behaviour should be found for both temporal and spatial measurements. This should notably be the case for the dispersion index. From eq. (4.5.5), the frozen flow hypothesis leads to

$$I(\tilde{T}) = \frac{\mathrm{Var}[N(x,\tilde{T})]}{\mathrm{Mean}[N(x,\tilde{T})]} = 1 + \frac{\mu}{\sigma-\mu}\left(1 + \frac{e^{-\tilde{T}}-1}{\tilde{T}}\right), \tag{4.5.7}$$

with $\tilde{T} = T/t_c$. We introduced $t_c = \ell_c/\langle u\rangle$ as the correlation time that is related to the frozen-flow hypothesis. Thus, at the high particle velocity limit, the variance of the sampled solid discharge at a given location has the same dependence on the acquisition duration as the

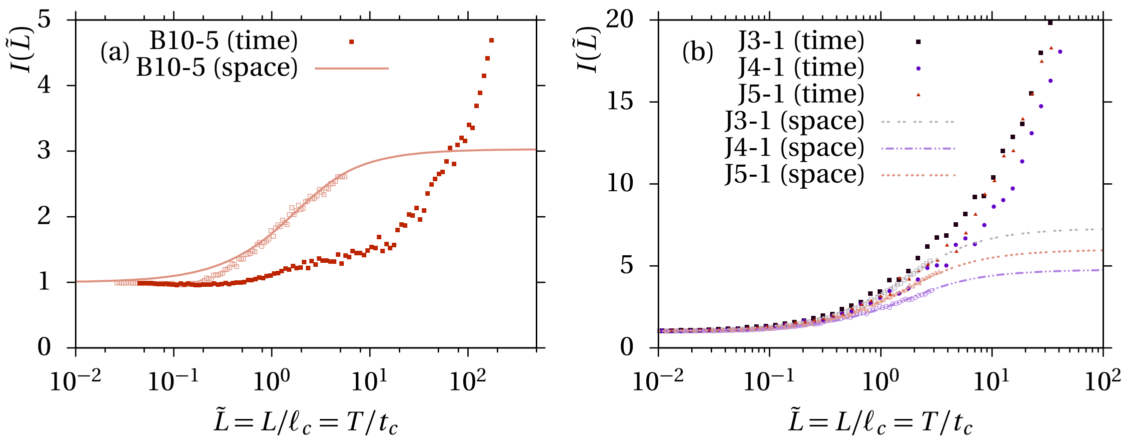

Figure 4.22: The frozen particle flow hypothesis, or the link between temporal and spatial dispersion indices. (Eq. (4.5.5) and Eq. (4.5.7)). (a) experiment B and (b) experiments J.

variance of the number of moving particles has on the observation window length.

In Fig. 4.22, I reported both dispersion indices (spatial and temporal) on the same graph for experiments B and J. As experiment R is relatively short (0.4 s), it was not used here.

The equivalence between spatial and temporal fluctuations via the Taylor hypothesis is severely called into question by Fig 4.22. The fluctuations of $N(x, \tilde{T})$ are Poissonnian at small time scales similarly to the fluctuations of $N(\tilde{L}, t)$. However, the behaviour of both spatial and temporal dispersion index diverges at larger scales. Indeed, at large time scales, the temporal dispersion index greatly exceeds the limiting value of the spatial dispersion index in all experiments. For intermediate time scales, experiments B and J behave differently. The temporal dispersion index of experiment B increases first slower than its spatial counterpart, but rejoins and exceeds the latter for scales of the order of $100t_c$, that is about 22 s. On the other hand, the temporal dispersion indices of experiments J closely follows the spatial dispersion index for time scales smaller than $10t_c$ (about 10 s), but beyond that, a net departure between the two indices is observed.

There may be several explanations of the departure between the two indices. First, the frozen flow hypothesis might not be valid in the context of sediment transport. Indeed, correlated structures may change rapidly during their advective motion so that an observer at a precise location would get a deformed picture of their shape. This explanation is confirmed by looking at the Péclet number of experiments B and J: the Péclet number of experiment B is rather small compared to the Péclet number of experiment J while we have shown that the the Taylor frozen flow hypothesis was valid in the case of $\mathscr{P}_e \to \infty$. Indeed, at small scales, the temporal dispersion index of experiment J is closer to the spatial one than in experiment B (Fig. 4.22).

However, this alone does not explain the fact that both indices have not the same limiting value $I(\infty)$. Two reasons may be put forward. First, the apparent plateau of the spatial

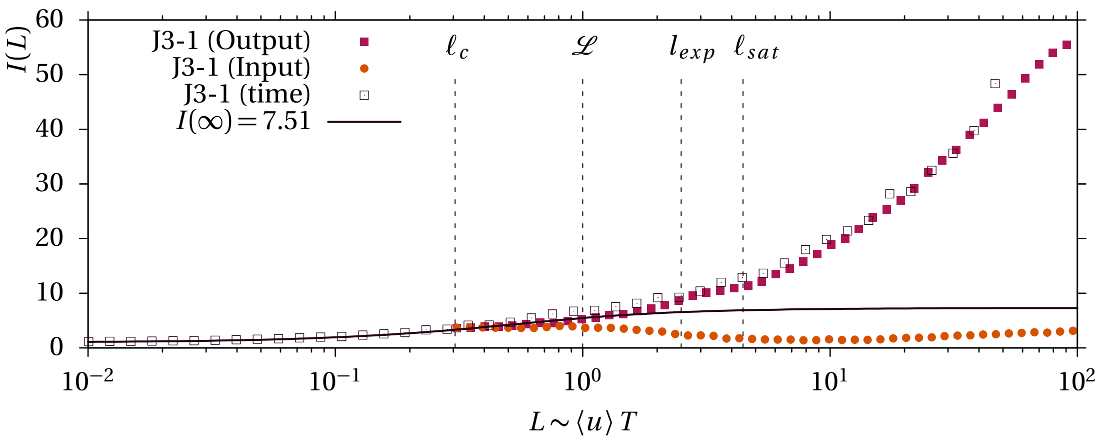

Figure 4.23: $I(L)$, in the frozen flow hypothesis as given by the accelerometer input and output signals as well as by the particle trajectories. I also reported the correlation length ℓ_c, the experiment length l_{exp}, the maximum observation window length $\mathscr{L}$ and the saturation length ℓ_{sat} for comparison.

dispersion index might be closely related to the maximum length of the observation window, so that a larger observation window, or even a larger experimental flume, would result in a higher plateau of the dispersion index. The second reason may be related to the apparent intermittent behaviour of the sediment transport in those experiments. Looking at Fig. 4.5, it is clear that particles travel by "clusters" that do not change a lot during their passage through the observation window. These clusters originate upstream of the observation window, and may be the hallmark of the sediment feeding system. Especially in experiments J, the relaxation length ℓ_{sat} is longer than the flume length so that, the influence of the inlet boundary conditions may affect the results.

The latter supposition can be checked quite easily since the sediment flux at the inlet and the outlet of the flume were simultaneously monitored with the same technique used for experiments H (i.e., accelerometers sensors). The temporal dispersion index computed from particle trajectories and that obtained from the accelerometers are shown in Fig. 4.23, and follow the same curve. The accelerometer time series being longer than a video sequence, the limiting value of the dispersion index can be computed for larger time scales (up to $200\ell_c$). On the other hand, the dispersion index of the input flux remains very low at all times, proving that no spurious correlations were introduced at the inlet by the sediment distribution system. Thus, the effect of the boundary conditions can be excluded in the explanation of the anomalously high values of the temporal dispersion index.

The last possible explanation is that the exchange rates, assumed to be constant in order to derive the theoretical dispersion index, may change with time and space. Indeed, even if the bed remained nearly flat in all experiments, small changes in bed slope and flow velocity may severely impact the sediment transport conditions and thus, the correlations observed.

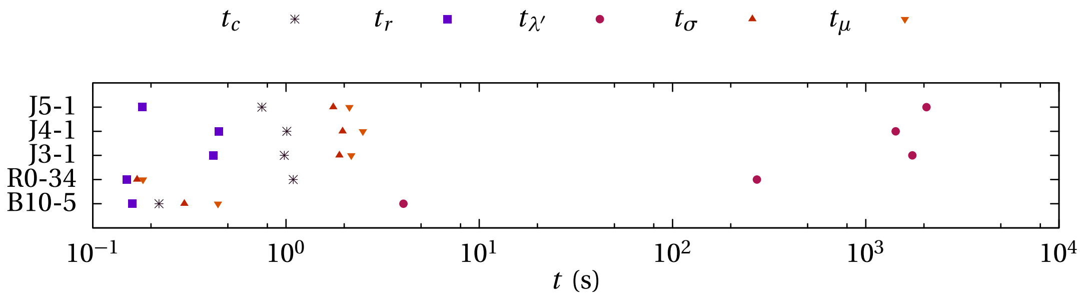

Figure 4.24: A summary of the time scales involved.

To go further, experimental or numerical studies of bed load transport involving longer spatial and temporal scales have certainly to be carried out.

6 Summary

In this chapter, a few experimental results were compared to theoretical predictions based on the models of Ancey *et al.* [2008] and Ancey & Heyman [2014]. In particular, two experiments (H and J) were developed during the thesis to obtain high quality samples of particle trajectories and long time series of bed load flux that allowed precise statistical analysis.

Experimental data agrees relatively well with the birth-death stochastic theory. Indeed, both Ancey *et al.*'s [2008] macroscopic model and Ancey & Heyman's [2014] local picture of the transport process give results comparable to what is observed experimentally (Figs. 4.15,4.17,4.20).

Besides these good results, there are some evidences that the stochastic models are only rough approximations of the reality of the transport process. For instance, theory poorly describes the high solid discharge region of the particle flux density function (Fig. 4.15), and also the K-function (Fig. 4.21). This can be explained by the fact that strong assumptions were made in order to obtain analytical results. For instance, to separate the transport of particles from the particles exchanges with the bed, it was assumed that the particle velocity relaxation time was much smaller than any other time scales of the problem. This approximation is somewhat called into question by looking at Fig. 4.24, where time scale estimates for all experiments are shown. In spite of this, the model has been found to perform well even in the small scales (Δx, $\Delta t \to 0$) where the assumption is expected to fail (see for instance, the spatial dispersion index of Fig. 4.20).

V Conclusion

1 Summary of results

This thesis has provided an experimental study of the fluctuations arising in bed load transport. Based on the study of individual particle motions, namely entrainment, transport and deposition, stochastic equations governing the particle activity at various scales were compared to various experimental data sets.

In the first stage of the thesis, a *macroscopic* picture of the fluctuations was studied using a simple birth-death model recently published [Ancey *et al.*, 2008]. Two applications were proposed. First, the probability density function of the volume averaged bed load flux was compared to experimental data [Ancey & Heyman, 2014]. The probability density is the sum of two contributing terms: a Dirac Delta function, encoding the relatively frequent periods without any solid flux, and an infinite sum of weighted Gaussian distributions, describing the relative probabilities of finding n moving particles in the volume with velocities u_i. This result assumes that the number of particles and their velocities are independent variables [Böhm *et al.*, 2004]. The second result is related to the time average solid flux or, equivalently, the flux measured at a precise location in time. By slightly modifying the original model, the probability density function of the inter-arrival time of particles could be derived [Heyman *et al.*, 2013]. The latter has a rather specific form due to the presence of collective entrainment, since two distinct time scales clearly appear in the probability density. This effect was referred to as "separation of time scales" and was shown to provide an additional evidence of the importance of collective dynamics in bed load transport.

In the second stage of the thesis, we studied the applications of Ancey & Heyman's [2014] stochastic model, which itself is based on the birth-death model of Ancey *et al.* [2008]. We showed that this model is able to describe the average transport process as well as spatio-temporal fluctuations in particle activity. These fluctuations, taking the shape of coherent structures of particle positions, were found to originate from the coupled action of the particle exchanges with the bed and the transport of particles by the flow [Heyman *et al.*, 2014]. Coherent structures were found to develop and to propagate only when collective entrainment was considered ($\mu > 0$). They can be related to experimental evidence of clustering during particle transport [Ancey *et al.*, 2006; Drake *et al.*, 1988].

The *local* model is based on five parameters, each of which has a physical meaning: the entrainment rate λ, the collective entrainment rate μ, the deposition rate σ, the average particle velocity $\langle u \rangle$ and the particle diffusivity D. The first two can be estimated via the method of moments (with Eqs. (3.3.22) and (4.5.3)) while the last three can be calibrated independently. Two characteristic lengths emerge from the model: a saturation length ℓ_{sat} (Eq. (3.3.26)) quantifying the length needed for particle activity to recover its average equilibrium value, and a correlation length $\ell_c = \sqrt{D/(\sigma - \mu)}$ which describes the typical size of fluctuations in particle activity. We also defined a local Péclet number $\mathscr{P}_e = \langle u \rangle\, l_c / D$ that describes the relative importance of advection against diffusion of particles at the correlation length. This number plays an important role in the shape of the spatio-temporal correlation function (Eq. (3.3.38)).

The stochastic model was tested against various experimental data of particle trajectories, and showed good overall agreement, notably in the description of the spatial dispersion index. The model also provides interesting guidelines for researchers studying the fluctuations of bed load transport rates. To capture 95% of the fluctuations of particle activity, an experiment should be designed such that it provides a measurement window larger than $20\ell_c$. The difficulty lies in the fact that ℓ_c is not known *a priori*, but has to be computed from parameter estimates or obtained experimentally. Another issue arises since, at scales of the order of $20\ell_c$, it is generally difficult to ensure experimentally the homogeneity of the bed load transport process. Indeed, bedforms inexorably develop and migrate, locally modifying the flow and in turn the sediment transport [Best, 2005]. Their wavelengths range from centimetres (ripples) to hundreds of meters (bars). Model parameters may thus vary in time and space, precluding the use of the results derived in the case of stationary and homogeneous transport conditions.

This leads us to question the use of average equations to describe bed load transport. As fluctuations were shown to span scales often larger than the ones at which bed load can be considered stationary and homogeneous —or even at scales larger than the experiment size— average equations (such as Eq. (3.3.21)) may fail to describe the non-linear interactions between the bed load fluctuations and the system boundaries. Consequently, a correct description of bed load transport cannot avoid the modelling of local fluctuations and their interactions with the system boundaries. These particular systems are sometime called "far from equilibrium" to express their tendency to exhibit locally large fluctuations compared to their mean behaviour [Nicolis & Prigogine, 1977].

2 Perspectives

The parameter estimation of stochastic models, such as the local model presented in this thesis, is fraught with difficulties. Indeed, it is likely that no bed load transport system could be found, in the laboratory or in nature, over scales small enough to be assumed in a stationary and homogeneous state, but large enough to measure the largest fluctuations of particle activity. We need thus to find other ways than the method of moments to estimate the model parameters. A general method, such as maximising a likelihood function —that would depend explicitly on the boundary conditions— may be more suitable [Iacus, 2008]. To construct such a space-time dependent function, a numerical solution of the Fokker–Planck equation (3.3.15) constrained by the experimental boundary conditions (such as the particle feeding system, the flume length, ...) might be of particular interest. Alternatively, Monte Carlo simulations of the stochastic equation (3.3.19) may also be envisioned, but at a greater computational cost. As model parameters are also expected to change with local modifications of the bed slope or the fluid flow, a similar likelihood function, inhomogeneous and unsteady, may be useful to estimate the dependence of parameters on such variables, overcoming the restrictive (and erroneous) assumption of a system evolving around a stationary and homogeneous equilibrium.

Now, imagine that the local stochastic model is coupled with the Exner and the Saint-Venant or Navier–Stokes equations. By a simultaneous and local description of the bed load transport fluctuations, as well as the fluid flow and the bed surface evolution, we may now be able to give a more accurate picture of the whole transport process. Interestingly, bedform growth may be triggered by sufficiently high bed perturbations, even when linear stability analysis predicts the stability of the bed-water interface. This may be the case with the growth of antidunes as they were proved to follow from a sub-critical bifurcation [Balmforth & Vakil, 2012; Colombini & Stocchino, 2008]. Thus, a coupled model may allow for a better description of the development of these particular bedforms.

The proposed model may also be generalized to a second spatial dimension. Indeed, the motion of particles is only rarely unidirectional, as particle impacts and turbulent flow velocity tend to modify particle trajectory. Thus, a dispersion of particles in the direction normal to the mean velocity vector may also occur [Seizilles *et al.*, 2014]. The corresponding transverse diffusivity is expected to be different than the diffusivity found in the mean particle flow direction, so that the overall dispersion process is anisotropic. Despite this and thanks to the overall linearity of the stochastic equation (3.3.19), the addition of a transverse diffusive flux is feasible.

A Theory

A.1 Poisson representation

In this appendix, we show that the master equation (3.2.4) governing the evolution of $P(n,t)$ (the probability of observing n moving particles in an observation window) greatly simplifies by a transformation called Poisson representation [Gardiner & Chaturvedi, 1977].

A.1.1 Principle

Let us assume that $P(n,t)$ can be written as a superposition of Poisson distributions with rates a

$$P(n,t)=\int_{\mathbb{R}^+}\frac{e^{-a}a^n}{n!}f(a,t)\mathrm{d}a, \tag{A.1.1}$$

where $f(a)$ is a positive real-valued function characterizing the relative probability of observing the Poisson rate a.

This representation can be seen as a Laplace-like transformation that allows us to pass from a discrete probability space, referred to as the n-space, to a continuous probability space, hereafter called the a-space. In general, it cannot be taken for granted that the function f is a genuine probability density function. Indeed, the existence and uniqueness of f can be shown, the constraint $\int_{\mathbb{R}^+} f(a)\mathrm{d}a = 1$ is satisfied, but it cannot be demonstrated that f is always positive [Gardiner & Chaturvedi, 1977].

In the present case, it will be shown that such a condition is systematically fulfilled and so, f is a genuine probability density function. The Poisson representation is thus a technique, which, similarly to generating functions, allows to transform a discrete probability space into a continuous probability space, making analytical calculations much easier.

Moreover, the Poisson representation enjoys many interesting properties, the most important being that the forward master equations (3.2.4) in the n-space are represented by a Fokker–Planck equation in the a-space. Another interesting feature is that the moments in the n- and a-spaces are related. Indeed, it can be easily checked that the p-factorial moment of n is equal to the p-moment of a:

$$\begin{aligned}
\langle n(n-1)(n-2)\ldots(n-p+1)\rangle &= \sum_{n=0}^{\infty} n(n-1)\ldots(n-p+1)P(n,t) \\
&= \int_{\mathbb{R}^+} \sum_{n=0}^{\infty} n(n-1)\ldots(n-p+1)\frac{e^{-a}a^n}{n!} f(a)\mathrm{d}a \\
&= \int_{\mathbb{R}^+} \frac{e^{-a}a^{n-p}}{(n-p)!} a^p f(a)\mathrm{d}a \\
&= \int_{\mathbb{R}^+} a^p f(a)\mathrm{d}a \\
&= \left\langle a_p \right\rangle .
\end{aligned} \tag{A.1.2}$$

This implies that $\langle n\rangle = \langle a\rangle$ and $\langle n^2\rangle = \langle a^2\rangle + \langle a\rangle$. This property will be quite useful in the following when mapping the a- and n-spaces.

A.1.2 Derivation of a Fokker–Planck equation for $f(a,t)$

We first express the generating function in the Poisson representation,

$$G(z,t) = \sum_{n=0}^{\infty} z^n \int_{\mathscr{C}} \frac{e^{-a}a^n}{n!} f(a,t)\mathrm{d}a = \int_{\mathscr{C}} e^{a(z-1)} f(a,t)\mathrm{d}a, \tag{A.1.3}$$

where the identity$e^x = \sum_{k=0}^{\infty} x^k/k!$ was used and where the integration domain $\mathscr{C}$ will be defined later. In a functional form, Eq. (A.1.3) reads

$$G(z,t) = \{K, f\}, \tag{A.1.4}$$

where the braces and K are respectively

$$\{f,g\} = \int_{\mathscr{C}} f(x)g(x)\mathrm{d}x, \quad K(z,a) = e^{a(z-1)}. \tag{A.1.5}$$

Replacing the generating function into the master equation (3.2.4) gives

$$\frac{\partial}{\partial t}G(z,t) = L_z[G], \qquad L_z[G] = \lambda\Delta x(z-1) + \left\{\sigma + \mu z^2 - (\mu+\sigma)z\right\}\frac{\partial G}{\partial z}. \tag{A.1.6}$$

Note that

$$\frac{\partial}{\partial t}G(z,t) = \left\{K, \frac{\partial f}{\partial t}\right\}, \tag{A.1.7}$$

such that if we find an operator M_a^* such that $L_z[G] = \left\{K, M_a^*[f]\right\}$, we would have an equation for f:

$$\left\{K, \frac{\partial f}{\partial t}\right\} = \left\{K, M_a^*[f]\right\} \Longleftrightarrow \frac{\partial f}{\partial t} = M_a^*[f]. \tag{A.1.8}$$

Keeping this objective in mind, we first expand $L_z[G]$ using (A.1.4). Noting that $\partial G/\partial z = \{aK, f\}$,

$$L_z[G] = \{[\lambda\Delta x(z-1) + a(z-1)(\mu z - \sigma)]\, K, f\}. \tag{A.1.9}$$

Further noticing that $\partial K/\partial a = (z-1)K$ and $\partial^2 K/\partial a^2 = (z-1)^2 K$, the last equation reads

$$L_z[G] = \left\{\left[(\lambda\Delta x - a(\mu-\sigma))\frac{\partial}{\partial a} + a\mu\frac{\partial^2}{\partial a^2}\right] K, f\right\} = \{M_a[K], f\}. \tag{A.1.10}$$

The task now consists in finding the adjoint operator $M_a^*[f]$ such that $\{M_a[K], f\} = \left\{K, M_a^*[f]\right\}$. This can be achieved by integrating $\{M_a[K], f\}$ by parts, and cancelling boundary terms:

$$\begin{aligned}
\{M_a[K], f\} &= \int_{\mathscr{C}} M_a[K] f(a)\mathrm{d}a \\
&= \int_{\mathscr{C}} (\lambda\Delta x - a(\mu-\sigma)) f(a)\frac{\partial K}{\partial a}\mathrm{d}a + \int_{\mathscr{C}} a\mu f(a)\frac{\partial^2 K}{\partial a^2}\mathrm{d}a \\
&= \left[K(\lambda\Delta x + a(\mu-\sigma))f + \mu a f\frac{\partial K}{\partial a} - \mu K\frac{\partial a f}{\partial a}\right]_{\partial\mathscr{C}} \\
&\quad + \int_{\mathscr{C}} K\left(\mu\frac{\partial^2}{\partial a^2}(af) - \frac{\partial}{\partial a}\left[(\lambda\Delta x + a(\mu-\sigma))f\right]\right)\mathrm{d}a.
\end{aligned} \tag{A.1.11}$$

Assuming that f is a probability density function, it must tend to zero in $+\infty$ to be normalizable. Furthermore, since a is the parameter of a Poisson distribution, it is strictly positive. Thus $f(a) = 0$ if $a < 0$. As a consequence, the boundary terms of Eq.(A.1.12) must vanish for

$\mathscr{C} = [0, +\infty[$. Thus:

$$\{M_a[K], f\} = \left\{K, M_a^*[f]\right\}, \quad M_a^*[f] = \mu \frac{\partial^2}{\partial a^2}(af) - \frac{\partial}{\partial a}\left[(\lambda \Delta x + a(\mu - \sigma))f\right]. \tag{A.1.12}$$

The governing equation for f is then

$$\frac{\partial f}{\partial t} = \mu \frac{\partial^2 af}{\partial a^2} - \frac{\partial}{\partial a}[(\lambda \Delta x - a(\sigma - \mu))f]. \tag{A.1.13}$$

This is a second-order nonlinear parabolic diffusion equation, which has the structure of a Fokker–Plank equation.

This opens up interesting avenues for further use and interpretation (see §A.1.4). Solutions to (A.1.13) have been studied by Feller [1951] and Sacerdote [1990]. Note that (A.1.13) is singular at $a = 0$ (transformation from a parabolic to a hyperbolic problem). In all cases encountered here ($\sigma - \mu > 0$ and $\lambda \Delta x > 0$), the solution is a genuine probability density function (a noncentral chi-square distribution) [Cox *et al.*, 1985].

A.1.3 Steady state solution

When $\mu = 0$ (no collective entrainment), the diffusive term in (A.1.13) cancels out, and (A.1.13) becomes hyperbolic:

$$\frac{\partial f}{\partial t} + \frac{\partial}{\partial a}[(\lambda \Delta x - a(\sigma - \mu))f] = 0. \tag{A.1.14}$$

A stochastic process whose Fokker–Planck equation contains only a drift term is called a Liouville process, and is purely deterministic [Gillespie, 1991]. Thus, for $\mu = 0$, the stochastic process governing the Poisson rate variable a is deterministic. One can solve the initial-value problem (A.1.14) with the method of characteristics:

$$\frac{Df}{Dt} = f\sigma \text{ along } a(t) \text{ with } \frac{\mathrm{d}a}{\mathrm{d}t} = \lambda \Delta x - a(t)\sigma, \tag{A.1.15}$$

$$a(0) = a_0, \quad f(a(0)) = f_0. \tag{A.1.16}$$

A continuous solution of (A.1.16) is

$$f(a(t)) = f_0 e^{\sigma t}, \quad a(t) = \frac{\lambda \Delta x}{\sigma} + \left(a_0 - \frac{\lambda \Delta x}{\sigma}\right) e^{-\sigma t}. \tag{A.1.17}$$

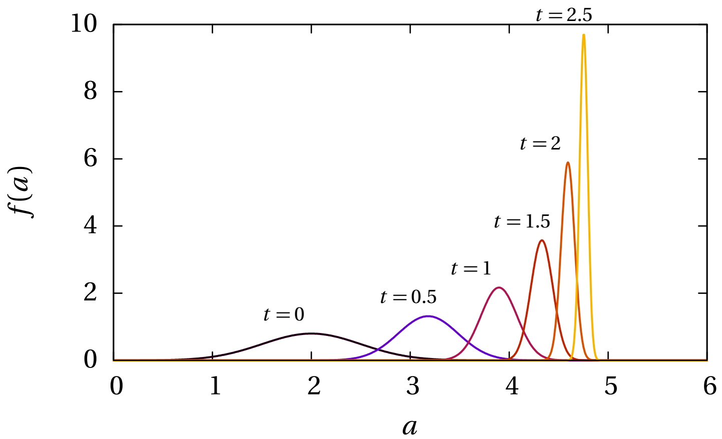

Figure A.1: Time evolution of $f(a,t)$ (Eq (A.1.14)) for various t. $\lambda\Delta x = 5$, $\sigma = 1$ and f_0 a Gaussian density function of mean 2 and standard deviation 0.5.

When $t \to \infty$, for any initial conditions $f(a_0)$, all characteristics tend to $\lambda\Delta x/\sigma$. Meanwhile $f(a(t)) \to \infty$ when $t \to \infty$, so that any initial density function f_0 will concentrate its mass around the value $a_\infty = \lambda\Delta x/\sigma$ (Fig. A.1). Thus, in the case $\mu = 0$, the steady state distribution is the Dirac Delta function:

$$f_s(a) = \delta(a - a_\infty). \tag{A.1.18}$$

Consequently, in the n-space, the stationary distribution of the number of moving particles when $\mu = 0$ is:

$$P_s(n) = \int_{\mathbb{R}^+} \frac{e^{-a} a^n}{n!} \delta(a - a_\infty) \mathrm{d}a = \frac{e^{-a_\infty} a_\infty^n}{n!}, \tag{A.1.19}$$

which is the Poisson distribution with mean $a_\infty = \lambda\Delta x/\sigma$, in agreement with equation (3.2.8). Put in other words, any non-Poissonian initial condition for $P(n, t = 0)$ will always relax to the Poisson distribution when $\mu = 0$ because the Poisson rate a tends to the sure value a_∞.

I now consider the case where $\mu > 0$. In the steady state (when $\partial_t f = 0$), integrating Eq. (A.1.13) reads :

$$\mu \frac{\partial a f}{\partial a} = (\lambda\Delta x - a(\sigma - \mu)) f + c_1. \tag{A.1.20}$$

For $a \to \infty$, $f \to 0$ and $af \to 0$ providing that the first moment of f exists. Thus $\partial af/\partial a \to 0$

and the constant of integration c_1 must be null. Integrating once again:

$$f(a) = c_2 a^{\lambda\Delta x/\mu - 1} \exp\left[-\frac{\sigma-\mu}{\mu} a\right] \tag{A.1.21}$$

where c_2 can be determined with the normalization condition $\int_{\mathbb{R}^+} f \mathrm{d}a = 1$. Finally, the gamma distribution $\mathrm{Ga}(\alpha,\beta)$ is recovered:

$$f(a) = Ga(a;\alpha,\beta) = \frac{a^{\alpha-1}\exp(-a/\beta)}{\Gamma[\alpha]\beta^\alpha}, \tag{A.1.22}$$

with $\alpha = \lambda\Delta x$ and $\beta = \mu/(\sigma-\mu)$.

Coming back to the n-space, the distribution of moving particle in the observation window is:

$$P_s(n) = \int_{\mathbb{R}^+} \frac{e^{-a}a^n}{n!} \mathrm{Ga}(a:\alpha,\beta)\mathrm{d}a = \mathrm{NegBin}(n,r,p) = \frac{\Gamma(r+n)}{\Gamma(r)} p^r (1-p)^n, \tag{A.1.23}$$

with $r = \alpha = \lambda\Delta x/\mu$ and $p = 1/(1+\beta) = 1-\mu/\sigma$. The solution (3.2.5), obtained with generating function, is retrieved within the Poisson representation framework.

A.1.4 Langevin representation

As (A.1.13) takes the form of a Fokker–Planck equation with the following drift and diffusion functions $A(a) = \lambda\Delta x + a(\mu-\sigma)$ and $D(a) = 2\mu a$, the process could also be interpreted in terms of a Langevin stochastic equation for $a(t)$:

$$\mathrm{d}a = A(a)\mathrm{d}t + \sqrt{D(a)}\mathrm{d}W(t) = (\lambda\Delta x - a(\sigma-\mu))\mathrm{d}t + \sqrt{2\mu a}\mathrm{d}W(t), \tag{A.1.24}$$

where $\mathrm{d}W(t)$ represents the time derivative of a Wiener process $W(t)$ (e.g., a Brownian random walk). $\mathrm{d}W(t)$ is also called “white noise” since it is uncorrelated in time. Note that the amplitude of the noise term is modulated by the collective entrainment parameter μ. In that case, the noise is said to be multiplicative (in contrast with an additive noise which is independent of the state of the process, as it was assumed in Jerolmack & Mohrig [2005] for instance).

In the absence of collective entrainment ($\mu = 0$), the process is purely deterministic in the

a-space:

$$\frac{\mathrm{d}a}{\mathrm{d}t} = \lambda\Delta x - a(\sigma-\mu) \Rightarrow a(t) = \frac{\lambda\Delta x}{\sigma} + \left(a_0 - \frac{\lambda\Delta x}{\sigma}\right)\exp[-\sigma t], \tag{A.1.25}$$

which is equivalent to Eq. (A.1.17).

When collective entrainment occurs ($\mu > 0$), the process is random, with a multiplicative noise term. In that case, the solution to (A.1.24) subject to $a(0) = a_0$ is

$$a(t) = a_\infty + (a_0 - a_\infty)\mathrm{e}^{-(\sigma-\mu)t} + \sqrt{2\mu}\mathrm{e}^{-(\sigma-\mu)t}\int_0^t \mathrm{e}^{(\sigma-\mu)t'}\sqrt{a(t')}\mathrm{d}W(t'), \tag{A.1.26}$$

where $a_\infty = \langle a\rangle_s = \lambda\Delta x/(\sigma-\mu)$ denotes the average stationary solution of a when $t \to \infty$.

A.1.5 Advantage of the Poisson representation

Let us summarize the approach. We started with a counting problem, in which we were interested in characterizing the evolution of N particles in a control volume, knowing that particles could be entrained (through individual or collective entrainment mechanisms controlled by $\lambda\Delta x$ and μ, respectively) or deposited (at a rate σ). The governing equation for N is the master equation (3.2.4).

Instead of working in the discrete probability space of the random variable N, it is possible to work in a continuous probability space, with the random variable a. The Fokker–Planck equation governing the probability function of a is obtained without any approximation, unlike Kramers-Moyal or system-size expansions, as used by Ancey [2010]. The resulting representation is strictly equivalent to the original master equation (3.2.4) and thus its validity does not depend on the system size.

This absolute equivalence is a great advantage compared to system size expansions: it allows us to study stochastic systems that are not in the thermodynamic equilibrium limit. Indeed, the Poisson representation is particularly suited for finite size systems where only a few particles are reacting. In this representation, the limit $\mathcal{V} \to 0$, or $N(t) \to 0$, is perfectly tractable. Thus, the Poisson representation allows for the development of a local stochastic theory for bed load. This is the topic of chapter 3.

It is worth noting that, any uni-molecular birth of death event—an event involving only one particle (e.g., entrainment and deposition)— does not induce stochastic component in the Poisson representation. Indeed, the Fokker–Planck equation (A.1.13) has only a drift term when $\mu = 0$. In other words, a stochastic process involving only reactions of individual particles can be treated as a purely deterministic process in the Poisson representation. In fact, this shows that such simple stochastic processes are always Poisonnian. Again, this will appear very helpful in chapter 3 where I will consider local exchanges between observation windows. These exchanges will be easily handled in the Poisson representation as they involve only individual particles.

A.2 Link to the BCRE model

The BCRE model presented by Bouchaud *et al.* [1995] gives the density of rolling grains $\mathscr{R}$ as the solution of

$$\partial_t \mathscr{R} + \nabla(V\mathscr{R}) = \nabla^2(D\mathscr{R}) - \mathscr{R}\alpha\nabla h, \tag{A.2.1}$$

where ∇h stands for the bed slope variations close to the angle of repose and α is a constant. Thus, in their model, when the slope is bigger than the angle of repose ($\nabla h < 0$) the second term on the left-hand side acts as a source in the equation. In that case, the number of rolling grains increases exponentially, leading to a local avalanche. On the contrary, when the slope is less than the angle of repose ($\nabla h > 0$), grains are mainly deposited, causing the avalanche to stop ($\mathscr{R} = 0$). The resemblance with Eq. (3.3.19) is striking. In the latter, an exponential increase in the number of moving particles occurs when the collective entrainment rate is greater than or equal to the deposition rate ($\mu \geq \sigma$). In contrast with (A.2.1), when deposition is greater than collective entrainment, a non trivial steady-state solution exists, due to the uncorrelated particle entrainment process (with rate λ).

Our model could thus be seen as a "BCRE" model that includes an additional random perturbation. Though the present work concerns bed load transport, and we restrict ourselves to the steady-state case ($\mu < \sigma$), the limit $\mu \to \sigma$ might be of particular interest for other granular flows. In particular, (3.3.19) may also be applicable to certain dry and dilute granular flows, and thus may allow for their statistical description.

A.3 Point process

It is possible to draw an analogy between the Poisson representation and the point process framework. Point processes are discrete processes in time or space. They consist in an ensemble of singular events, or objects (points) distributed in the continuum space. For instance, the locations of pine trees in a forest, the failure times of a light bulb, or even the arrival times of particles (chapter IV section 4.2) can all be appreciated through the point process framework [Cox & Isham, 1980].

Point processes are generally described with their rate function η, defined as the expected number of points per unit space [Cox & Isham, 1980]. The simplest case is when the rate function is constant in time and space. In that case, counting the points in a given area S results in a Poisson distributed random variable of rate ηS. Those processes are called Poisson point processes. When the rate function is a function of space and/or time, $\eta = \eta(x, t)$, the process is called an inhomogeneous Poisson point process. Eventually, when the rate function is also a random variable, the process is called a doubly stochastic point process, or Cox process [Cox & Isham, 1980].

Now, consider an instantaneous picture of the transport process, for instance by looking at Fig. 4.5 at fixed time. Moving particles are spread on the real line and thus also define a point process. We saw that, in the Poisson represention, the Poisson activity $\eta(x, t)$ was a random variable following (3.3.19). Thus, the process I described previously is a doubly stochastic point process for $\mu > 0$ and a Poisson process for $\mu = 0$. To summarize, starting from a multivariate Markov process defined on a lattice and described by a multivariate master equation, I ended up with a model belonging to a general class of point processes, called doubly stochastic processes, when collective entrainment is considered.

The two approaches are related through the Poisson representation. The advantage of using the birth-death framework lies in the facility it offers to derive a multivariate master equation. However, it does not describe the individual location of particles (they are summed in a lattice cell). On the other hand, viewing particle transport as a spatial point process allows to study relationships existing among individual particles, such as the mean particle distance, the two-particles density function... Those can then be used as closure equations of statistical models [Herczynski & Pienkowska, 1980].

To prove the pertinence of the preceding comparison between the two approaches, I show how it is possible to compute a probable realization of particle positions from Eq. (3.3.19). As noted earlier, by means of the Poisson representation, $\eta(x, t)$ can be interpreted as the random rate of a Poisson distribution. First, Eq. (3.3.19) needs to be numerically solved to get a realization of $\eta(x)$ at a given time t. This can be achieved using standard methods for stochastic differential equations (for instance an Euler–Maruyama scheme [Kloeden & Platen, 2011]). Once a realization of $\eta(x)$ has been obtained, I proceed as follows. A constant $C > \eta(x)$ is chosen and then a realization of point positions according to a Poisson process with rate C is

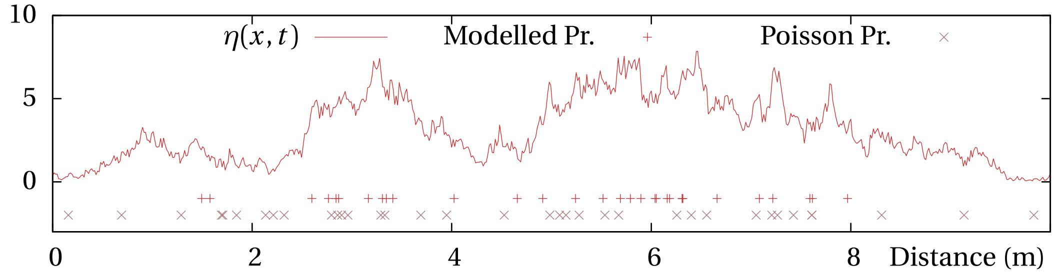

Figure A.2: Simulation of the Poisson rate process (Eq. (3.3.19)) and corresponding possible realization of particle positions. The Poissonian case (with the same mean rate) is also plotted for the sake of comparison. Model parameters are $\lambda = 0.05$ particles/m, $\mu = 9.99$ s^{-1}, $\sigma = 10$ s^{-1}, $\langle u \rangle = 0.1$ m s^{-1} and $D = 0.008$ m^{2}s^{-1}

computed. This can be achieved by taking the distance between points to be an exponentially distributed random variable with parameter $1/C$, for instance. Then, a point k is randomly selected or discarded according to the criteria:

$$\begin{aligned} \text{if } r &< \eta(x_k)/C, \text{ keep point;} \\ \text{if } r &> \eta(x_k)/C, \text{ delete point;} \end{aligned}$$

where r is drawn from a uniform distribution in $[0,1]$. The remaining points form a possible observation of particle positions according to the model. In Fig. A.2, it is possible to observe the clustering of particles around the region of high $\eta(x)$ values, while for the Poisson process, particles positions are purely random so that no clustering appears. The clustering of particles is a special feature of the local model (when $\mu > 0$) and can be quantified by the study of second moments.

A.4 Average behavior

In the following, I denote the Fourier transform of a function f by its capital letter F. Using the Fourier transform in the space variable,

$$\langle \gamma^*(\tilde{x}, \tilde{t}) \rangle = \frac{1}{2\pi} \int_{-\infty}^{+\infty} \Gamma(\omega, \tilde{t}) e^{i\omega\tilde{x}} \mathrm{d}\omega, \tag{A.4.1}$$

eq. (3.3.27) can be written as

$$\mathrm{d}\Gamma(\omega, \tilde{t}) = -\left[\omega^2 + \mathrm{i}\omega\mathscr{P}_e + 1\right] \Gamma(\omega, t)\mathrm{d}\tilde{t}. \tag{A.4.2}$$

Given the initial condition

$$\Gamma(\omega,0)=\int_{-\infty}^{+\infty}\gamma_0\delta(\tilde{x})e^{-i\omega\tilde{x}}\mathrm{d}\omega=\gamma_0, \tag{A.4.3}$$

we can solve (A.4.2):

$$\Gamma(\omega,\tilde{t})=\gamma_0\exp\left(-\left[\omega^2+\mathrm{i}\omega\mathscr{P}_e+1\right]\tilde{t}\right). \tag{A.4.4}$$

The inverse Fourier transform of (A.4.4) is

$$\langle\gamma(\tilde{x},\tilde{t})^*\rangle=\frac{\gamma_0}{\sqrt{4\pi\tilde{t}}}\exp\left(-\frac{(\tilde{x}-Pe\,\tilde{t})^2}{4\tilde{t}}-\tilde{t}\right). \tag{A.4.5}$$

A.5 Spatial correlation function

Let $g(x,x',t)$ denote the spatial correlation function of the Poisson density variable $\eta(x,t)$. By definition:

$$\begin{aligned} g(x,x',t) &= \langle\eta(x,t),\eta(x',t)\rangle \\ &\equiv \langle\eta(x,t)\eta(x',t)\rangle-\langle\eta(x,t)\rangle^2. \end{aligned} \tag{A.5.1}$$

Taking the differential of g and using Itō's lemma [1],

$$\begin{aligned} \mathrm{d}g(x,x',t) &= \mathrm{d}\langle\eta(x,t)\eta(x',t)\rangle-\mathrm{d}\left(\langle\eta(x,t)\rangle^2\right) \\ &= \langle\mathrm{d}\eta(x,t)\eta(x',t)\rangle+\langle\eta(x,t)\mathrm{d}\eta(x',t)\rangle+\langle\mathrm{d}\eta(x,t)\mathrm{d}\eta(x',t)\rangle, \end{aligned}$$

where the last term in the right hand side of the previous equation is an additional quadratic co-variation term arising in the integration by parts of stochastic integrals. Note that $\mathrm{d}\left(\langle\eta(x,t)\rangle^2\right)$ is zero by definition of the average. Using Eq. (3.3.18) and Eq. (3.3.22), Eq. (A.5.2) becomes

$$\begin{aligned} \mathrm{d}g(x,x',t) &= D\left(\partial^2/\partial x^2+\partial^2/\partial x'^2\right)\langle\eta(x,t)\eta(x',t)\rangle\,\mathrm{d}t \\ &\quad - \langle u\rangle\left(\partial/\partial x+\partial/\partial x'\right)\langle\eta(x,t)\eta(x',t)\rangle\,\mathrm{d}t \\ &\quad - 2(\sigma-\mu)\langle\eta(x,t)\eta(x',t)\rangle\,\mathrm{d}t+2\langle\eta\rangle_s\left(\lambda+\mu\delta(x-x')\right)\mathrm{d}t. \end{aligned} \tag{A.5.2}$$

1. Itō's lemma is the stochastic equivalent to the chain rule (differentiation of functions of continuous variables).

In a spatially homogeneous situation, $g(x,x',t)$ is a function of $r=|x-x'|$ only, which is denoted by $g(r,t)$. Thus, substituting Eq. (A.5.1) into Eq. (A.5.3), we obtain:

$$D\frac{\partial^2 g_s(r)}{\partial r^2}-(\sigma-\mu)g_s(r)+\mu\langle\gamma\rangle_s\,\delta(r)=0, \tag{A.5.3}$$

with $r=|x-x'|$. One can simplify Eq. (A.5.3) by rescaling the variable r by $\tilde{r}=r/\ell_c$,

$$\frac{\partial^2 g_s(\tilde{r})}{\partial \tilde{r}^2}-g_s(\tilde{r})+\frac{\langle\gamma\rangle_s}{\ell_c}\frac{\mu}{\sigma-\mu}\delta(\tilde{r})=0, \tag{A.5.4}$$

with $\ell_c=\sqrt{D/(\sigma-\mu)}$. Taking the Fourier transform of (A.5.4), we obtain the algebraic equation

$$G(\omega)=\frac{\langle\gamma\rangle_s}{\ell_c}\frac{\mu}{\sigma-\mu}\frac{1}{\omega^2+1}, \tag{A.5.5}$$

with G the Fourier transform of g_s and ω the angular frequency. The Fourier inverse of Eq. (A.5.5) is given by

$$g_s(\tilde{r})=\frac{\langle\gamma\rangle_s}{2\ell_c}\frac{\mu}{\sigma-\mu}\exp(-|\tilde{r}|). \tag{A.5.6}$$

Hence

$$\langle\eta(x),\eta(x')\rangle_s=\frac{\langle\gamma\rangle_s}{2\ell_c}\frac{\mu}{\sigma-\mu}\exp\left(-\frac{|x-x'|}{\ell_c}\right). \tag{A.5.7}$$

A.6 Spatio-temporal correlation function

We want to solve the equation

$$\frac{\partial G(x,t)}{\partial t}=D\frac{\partial^2 G(x,t)}{\partial x^2}-\langle u\rangle\frac{\partial G(x,t)}{\partial x}-(\sigma-\mu)G(x,t), \tag{A.6.1}$$

with initial condition $G(x,0)$ given by the solution of the stationary spatial correlation function, Eq. (3.3.33). Taking the dimensionless variables $\tilde{t}=(\sigma-\mu)t$ and $\tilde{x}=x/\ell_c$ one can simplify Eq. (A.6.1),

$$\frac{\partial G(\tilde{x},\tilde{t})}{\partial \tilde{t}}=\frac{\partial^2 G(\tilde{x},\tilde{t})}{\partial \tilde{x}^2}-\mathscr{P}_e\frac{\partial G(\tilde{x},\tilde{t})}{\partial \tilde{x}}-G(\tilde{x},\tilde{t}), \tag{A.6.2}$$

with $\mathscr{P}_e=\langle u\rangle\ell_c/D$. The Fourier transform of Eq. (A.6.2) reads

$$\frac{\partial \mathscr{G}(\omega,\tilde{t})}{\partial \tilde{t}}=-(\omega^2+\mathscr{P}_e\mathrm{i}\omega+1)\mathscr{G}(\omega,\tilde{t}), \tag{A.6.3}$$

with $\mathscr{G}$ the Fourier transform of G and ω the angular frequency. The Fourier representation of the initial condition Eq. (3.3.33) is

$$\mathscr{G}(\omega,0)=\frac{\langle\gamma\rangle_s}{\ell_c}\left[1+\left(\frac{\mu}{\sigma-\mu}\right)\frac{1}{\omega^2+1}\right], \tag{A.6.4}$$

so that the solution of Eq. (A.6.3) is

$$\mathscr{G}(\omega,\tilde{t})=\mathscr{G}_d(\omega,\tilde{t})+\mathscr{G}_r(\omega,\tilde{t}), \tag{A.6.5}$$

with

$$\begin{aligned}\mathscr{G}_d(\omega,\tilde{t}) &= \frac{\langle\gamma\rangle_s}{\ell_c}\exp\left[-(\omega^2+\mathscr{P}_e\mathrm{i}\omega+1)\tilde{t}\right],\\ \mathscr{G}_r(\omega,\tilde{t}) &= \frac{\langle\gamma\rangle_s}{\ell_c}\frac{\mu}{\sigma-\mu}\frac{\exp\left[-(\omega^2+\mathscr{P}_e\mathrm{i}\omega+1)\tilde{t}\right]}{\omega^2+1}.\end{aligned} \tag{A.6.6}$$

The inverse Fourier transform of Eq. $\mathscr{G}_d(\omega,\tilde{t})$ is

$$G_d(\tilde{x},\tilde{t})=\frac{\langle\gamma\rangle_s}{2\ell_c\sqrt{\pi\tilde{t}}}\exp\left[\frac{(\tilde{x}-\mathscr{P}_e\tilde{t})^2}{4\tilde{t}}-\tilde{t}\right]. \tag{A.6.7}$$

Computing the inverse of $\mathscr{G}_r(\omega,\tilde{t})$ is a more difficult task. The convolution property of Fourier transforms gives

$$\mathscr{F}^{-1}\{F_1\times F_2\}=f_1*f_2, \tag{A.6.8}$$

where F_i is the Fourier transform of f_i and $*$ the convolution operator. $\mathscr{G}_r(\omega,\tilde{t})$ is the product of two functions whose Fourier inverses are

$$\mathscr{F}^{-1}\left\{\frac{1}{\omega^2+1}\right\} = \frac{\exp(-|x|)}{2}, \tag{A.6.9}$$

$$\mathscr{F}^{-1}\left\{\exp\left[-\omega^2\tilde{t}\right]\right\} = \frac{\exp\left[-x^2/(4t)\right]}{\sqrt{4\pi\tilde{t}}}, \tag{A.6.10}$$

so that the Fourier inverse of $\mathscr{G}_r(\omega,\tilde{t})$ is given by

$$G_r(\tilde{x}+\mathscr{P}_e\tilde{t},\tilde{t}) = \frac{\langle\gamma\rangle_s}{\ell_c}\frac{\mu}{\sigma-\mu}\frac{\exp(-\tilde{t})}{2\sqrt{4\pi\tilde{t}}}\int_{-\infty}^{+\infty}\exp\left(-|\tilde{x}-y|\right)\exp\left(\frac{-y^2}{4\tilde{t}}\right)\mathrm{d}y.$$

Knowing the value of the integrals

$$\int_{-\infty}^{x} \exp(y)\exp\left(\frac{-y^2}{4t}\right)\mathrm{d}y = \sqrt{\pi t}\,\exp(t)\mathrm{erfc}\left(\frac{2t-x}{2\sqrt{t}}\right),$$

and

$$\int_{x}^{\infty} \exp(-y)\exp\left(\frac{-y^2}{4t}\right)\mathrm{d}y = \sqrt{\pi t}\,\exp(t)\mathrm{erfc}\left(\frac{2t+x}{2\sqrt{t}}\right),$$

where erfc is the complementary error function (e.g. erfc(x)=1-erf(x)), we can obtain a general solution for Eq. (A.6.11),

$$\begin{aligned} G_r(\tilde{x},\tilde{t}) = \frac{\langle\gamma\rangle_s}{4\ell_c}\frac{\mu}{\sigma-\mu} & \left\{\exp\left(\tilde{x}-\mathscr{P}_e\tilde{t}\right)\mathrm{erfc}\left[(1-\mathscr{P}_e/2)\sqrt{\tilde{t}}+\tilde{x}/(2\sqrt{\tilde{t}})\right]\right. \\ & \left. +\exp\left(\mathscr{P}_e\tilde{t}-\tilde{x}\right)\mathrm{erfc}\left[(1+\mathscr{P}_e/2)\sqrt{\tilde{t}}-\tilde{x}/(2\sqrt{\tilde{t}})\right]\right\}. \end{aligned}$$

A.7 Equivalence between spatial and temporal correlations at large $\mathscr{P}_e$

In this appendix, we prove that the temporal correlation function (at a given location) $G(0,\tilde{t})$ (Eq. (3.3.37)) tends to the spatial correlation function $\langle\gamma(\tilde{x}),\gamma(0)\rangle_s$ (Eq. (3.3.33)) when $\mathscr{P}_e\to\infty$) with the correspondence between time and space given by $\tilde{x}\sim\mathscr{P}_e\tilde{t}$. For $\tilde{x}=0$, G_r simplifies to

$$G_r(0,\tilde{t}) = \frac{\langle\gamma\rangle_s}{4\ell_c}\frac{\mu}{\sigma-\mu}\left\{\exp\left(-\mathscr{P}_e\tilde{t}\right)\mathrm{erfc}\left[(1-\mathscr{P}_e/2)\sqrt{\tilde{t}}\right]+\exp\left(\mathscr{P}_e\tilde{t}\right)\mathrm{erfc}\left[(1+\mathscr{P}_e/2)\sqrt{\tilde{t}}\right]\right\} \quad (A.7.1)$$

The last expression can be further simplified in the limit of $\mathscr{P}_e\to\infty$ by taking the asymptotic expansions of complementary error function in $\pm\infty$,

$$\begin{aligned} \lim_{y\to\infty}\mathrm{erfc}(y) &= \frac{\mathrm{e}^{-y^2}}{\sqrt{\pi}}\left(\frac{1}{y}+O(y^{-3})\right), \\ \lim_{y\to-\infty}\mathrm{erfc}(y) &= 2-\frac{\mathrm{e}^{-y^2}}{\sqrt{\pi}}\left(\frac{1}{y}+O(y^{-3})\right). \end{aligned}$$

Introducing these limits into Eq. (A.7.1), and with a little algebra, we find that

$$\lim_{\mathscr{P}_e \to \infty} G_r(0,\tilde{t}) \quad \simeq \quad \frac{\langle \gamma \rangle_s}{2\ell_c} \frac{\mu}{\sigma - \mu} \exp\left(-\mathscr{P}_e \tilde{t}\right). \tag{A.7.2}$$

To find the limit of G_d at large $\mathscr{P}_e$, we first consider the case of $\tilde{t} > 0$. For $\tilde{x} = 0$, G_d simplifies to

$$G_d(0, \tilde{t} > 0) = \frac{\langle \gamma \rangle_s}{2\ell_c \sqrt{\pi \tilde{t}}} \exp\left[-({\mathscr{P}_e}^2/4 + 1)\tilde{t}\right], \tag{A.7.3}$$

When $t \to 0$, at fixed $\mathscr{P}_e$ and $\tilde{x}$, we have the limit

$$\lim_{\tilde{t} \to 0} G_d(\tilde{x}, \tilde{t}) \simeq \frac{\langle \gamma \rangle_s}{2\ell_c \sqrt{\pi \tilde{t}}} \exp\left[\frac{-(\tilde{x} - \mathscr{P}_e \tilde{t})^2}{4\tilde{t}}\right] \simeq \frac{\langle \gamma \rangle_s}{\ell_c} \delta(\tilde{x}). \tag{A.7.4}$$

Finally, to leading order, we have

$$\lim_{\mathscr{P}_e \to \infty} G(\tilde{x}, \tilde{t}) \quad \simeq \quad \frac{\langle \gamma \rangle_s}{\ell_c} \delta(\tilde{x}) + \frac{\langle \gamma \rangle_s}{2\ell_c} \frac{\mu}{\sigma - \mu} \exp\left(-\mathscr{P}_e \tilde{t}\right). \tag{A.7.5}$$

We can recognize in Eq. (A.7.5) the spatial correlation function (3.3.33) with $\mathscr{P}_e \tilde{t} = \tilde{x}$. This proves the equivalence between spatial and temporal correlations of particle activity at large $\mathscr{P}_e$.

B Experiments

B.1 Velocity threshold

The value of the velocity threshold discriminating moving from resting particles may have a strong impact on the results. To show this, I consider the values of the deposition rate σ, the relaxation time t_r and the diffusivity D for different velocity thresholds applied to experiments B10-5 and J3-1 (Fig. B.1).

It can be noted from Fig. B.1 that the velocity threshold has a strong influence on the estimated value of parameters. It is strongly determinant in experiment B10-5 while slightly less important in experiment J3-1. In experiment B, the transport of particles involved at least three different mechanisms: (i) bed creeping at extremely low velocities, (ii) particle rolling motion at low velocities and (iii) particle saltation at medium and high velocities. Changing the threshold thus favours or penalizes one mode of motion against another. It is worth noting the abrupt decrease in particle flux when the threshold increases in experiment B10-5, proving that a lot of particles move rather slowly inside the bed layer.

In contrast, the bed load flux of experiment J3-1 is not that sensitive to the threshold value. This can be explained by the fact that particles mainly move in saltation. Indeed, the rolling motion is limited by the non-spherical shape of particles while bed creeping is absent due to high friction contact between particles.

More generally, increasing the velocity threshold results in a decrease of the bed load flux $\bar{q}_s$ together with an increase of the mean sediment velocity $\bar{u}$ and a decrease of its standard deviation σ_u. It also results in a decrease of the velocity relaxation time t_r and of the apparent

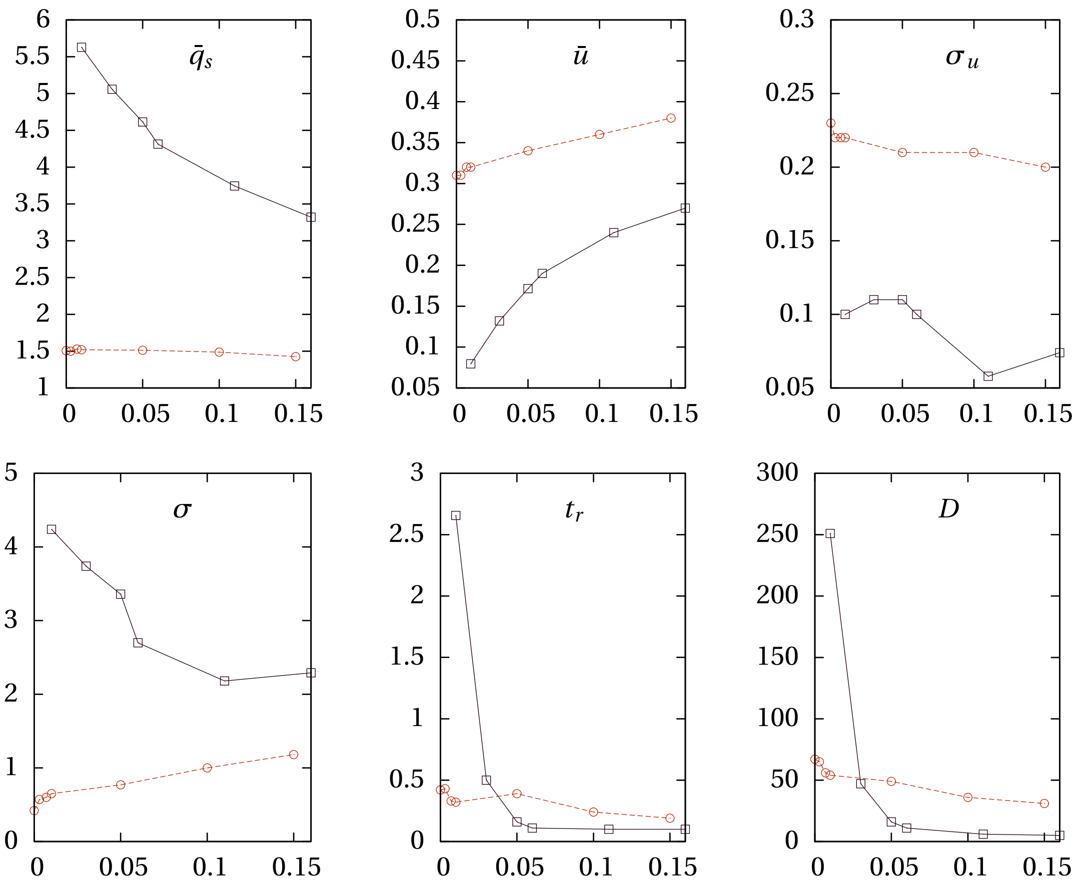

Figure B.1: Sensibility of computed parameters depending on the values of the velocity threshold for experiment B10-5 (black squares) and experiment J3-1 (orange circles).

diffusivity rate D. This may be explained by the fact that fewer and fewer rolling and sliding particles are counted as moving when the threshold is increased so that the bulk dynamics, mainly constituted of saltating particles, appears more uniform.

The deposition rate σ has a more complex dependence on velocity threshold. On the one hand, decreasing the velocity threshold favours long trajectories, that is, low deposition rates. In the other hand, increasing the velocity threshold may also decrease deposition rates as slow particles – more likely to deposit than fast particles– are not taken into account in the moving phase. As pointed out previously, such a threshold is arbitrary and does not rely on physical bases. To overcome this issue of sensibility, a full phase-space modelling of positions and velocities may be considered. In this framework, no criteria separating resting from moving particles would have to be postulated.

B.2 An album of particle motions

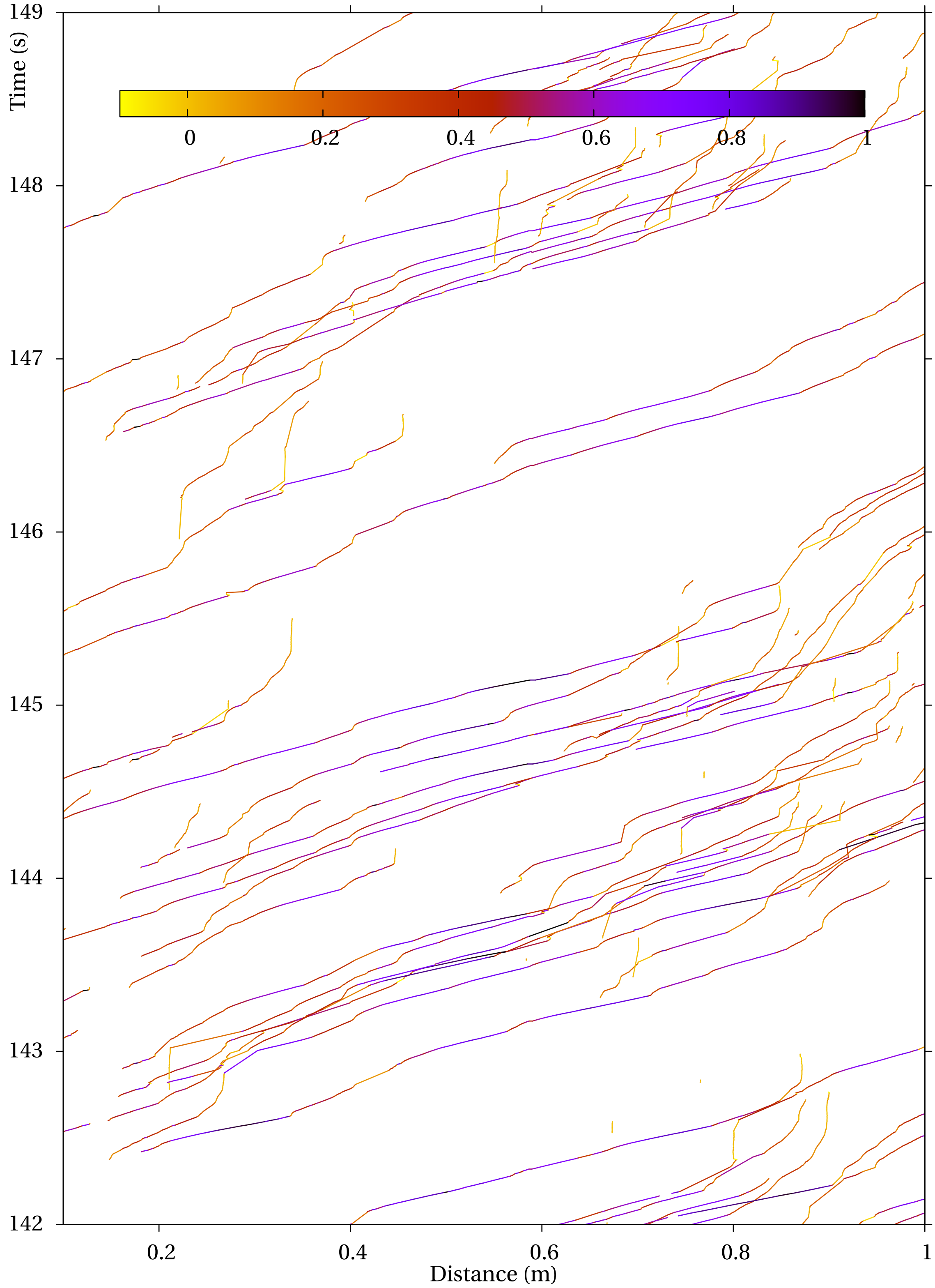

Figure B.2: Particle trajectories in experiment J5-1. Colours encode velocity (in m/s).

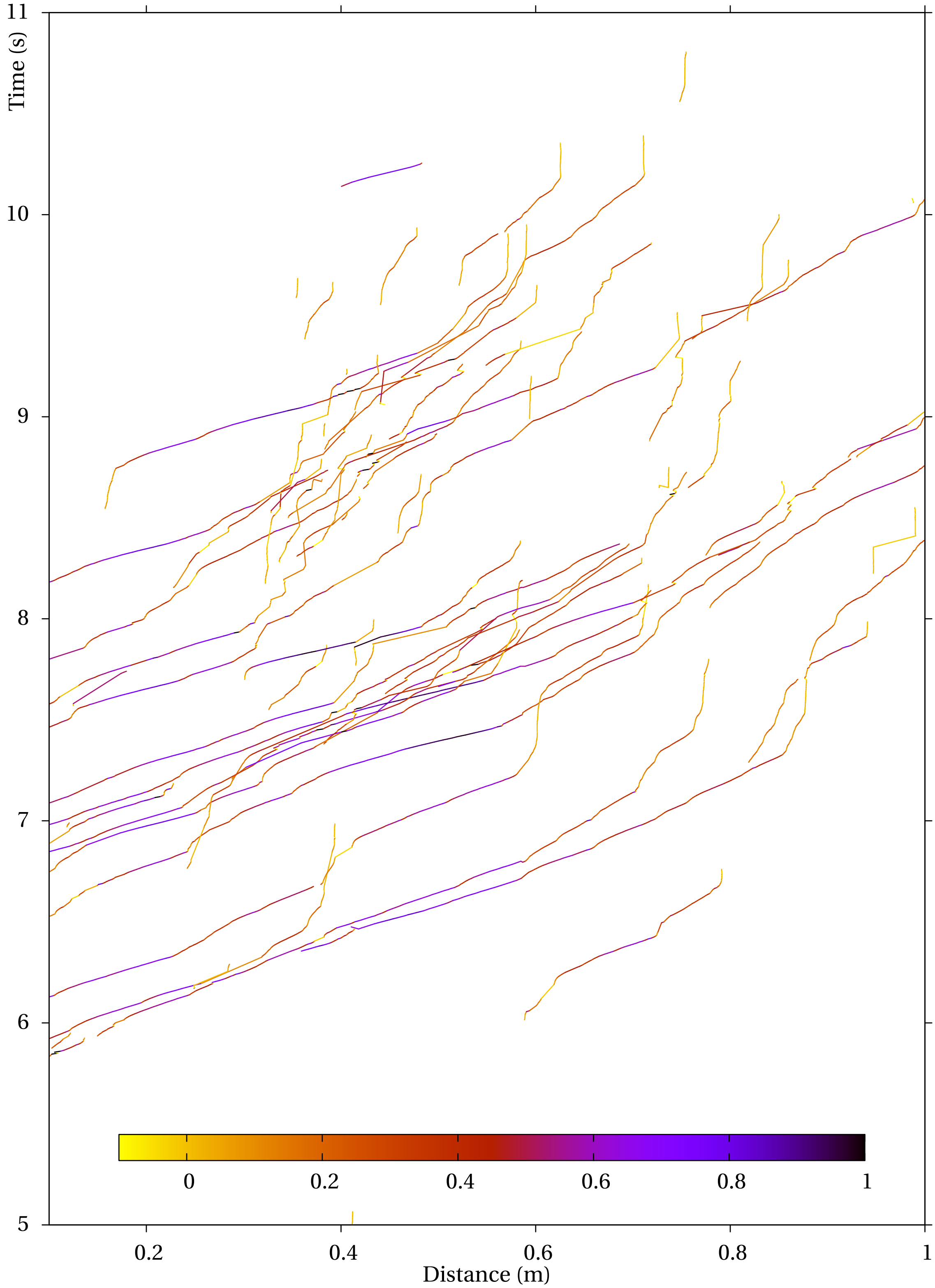

Figure B.3: Particle trajectories in experiment J3-1. Colours encode velocity (in m/s).

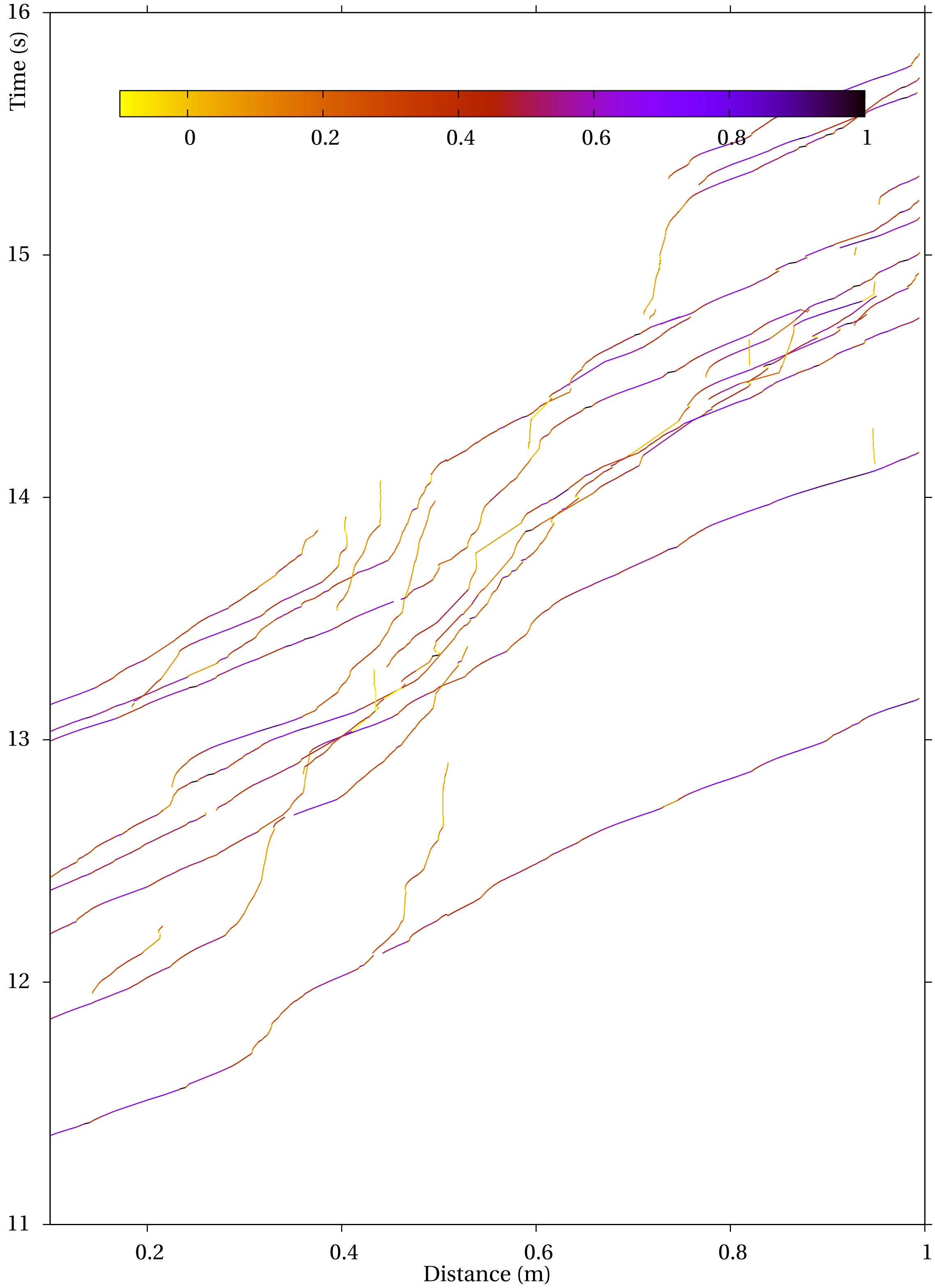

Figure B.4: Particle trajectories in experiment J4-1 (second run). Colours encode velocity (in m/s).

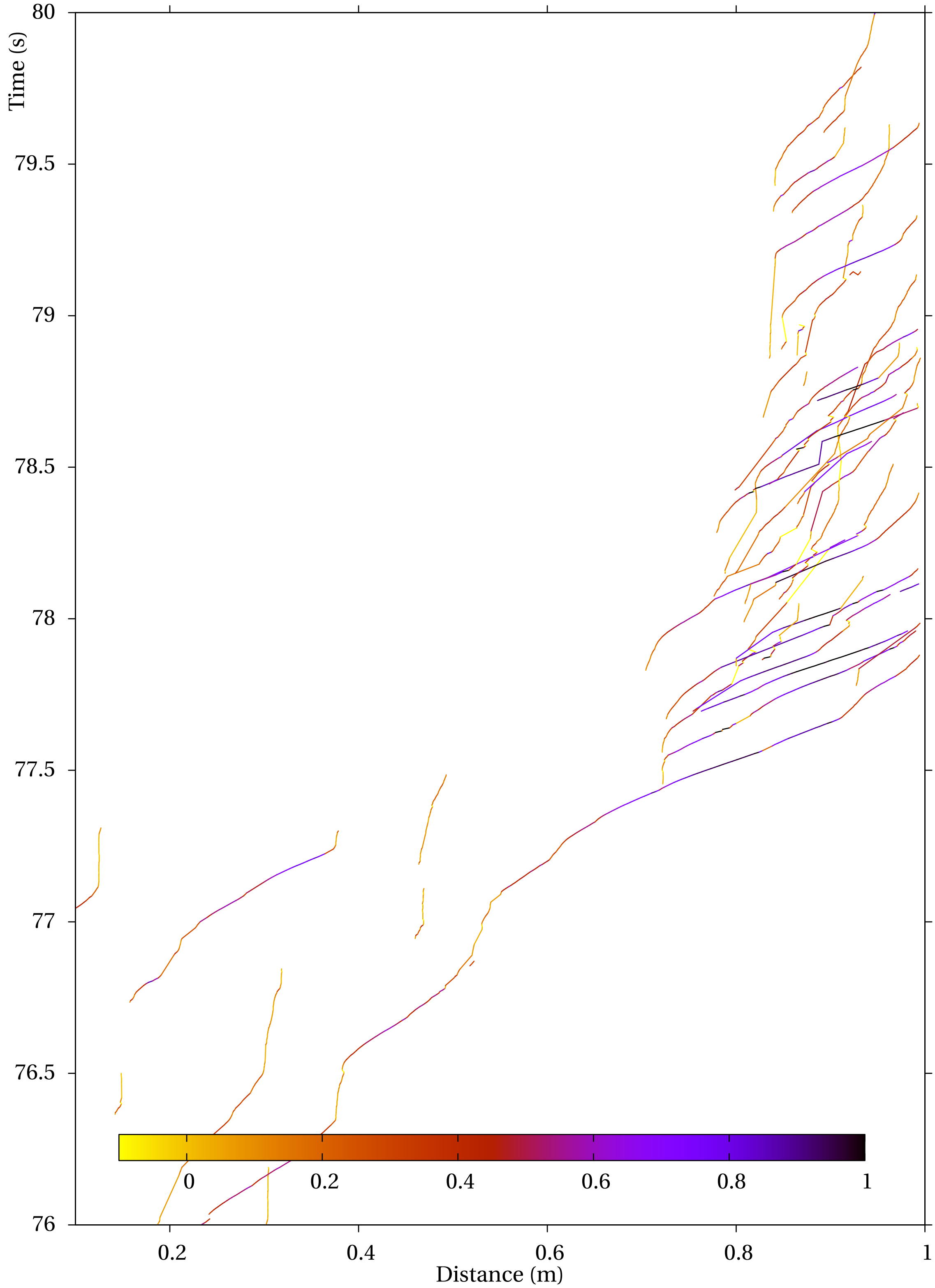

Figure B.5: Particle trajectories in experiment J4-1 (fourth run). Colours encode velocity (in m/s).

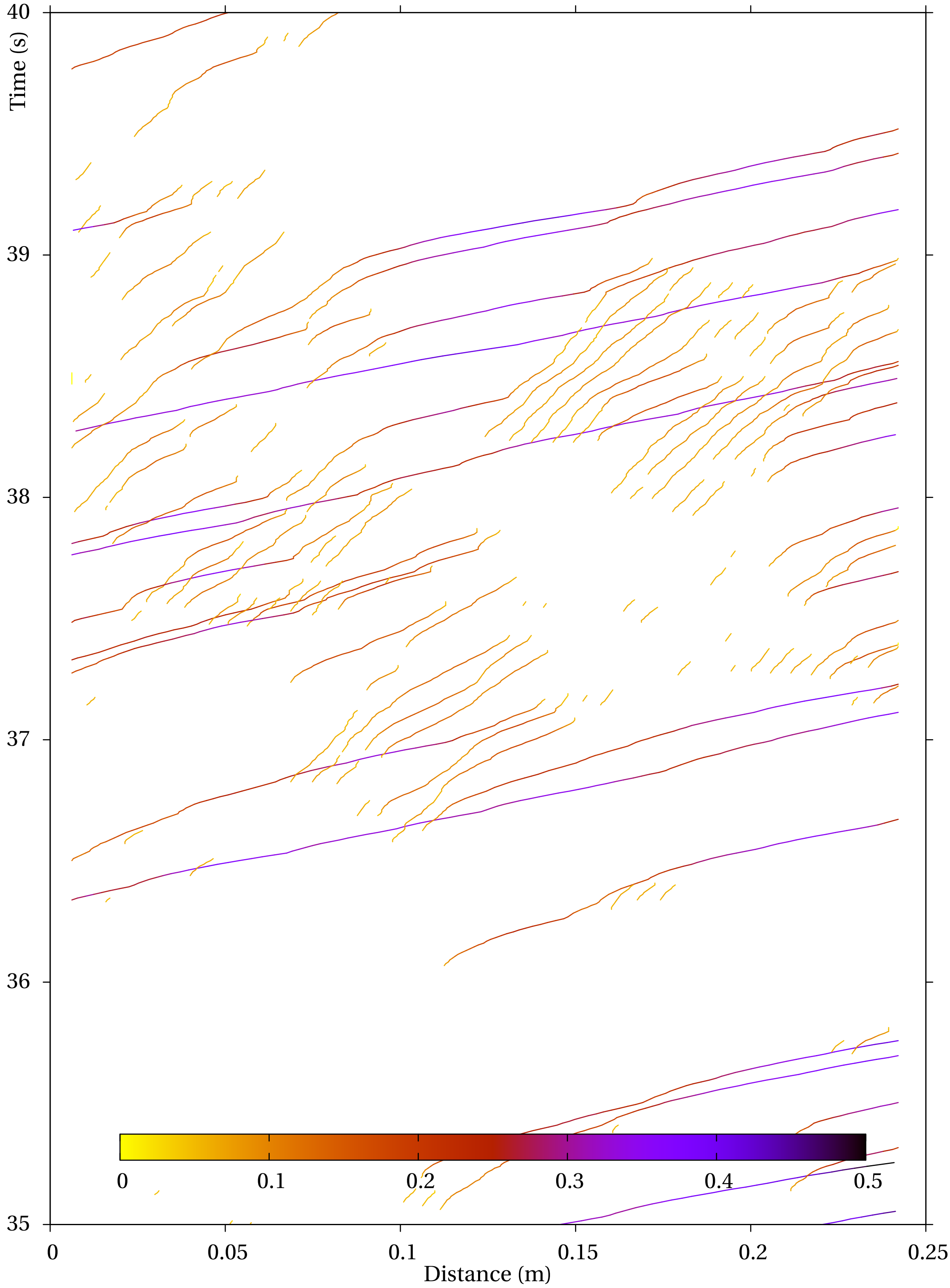

Figure B.6: Particle trajectories in experiment B10-5. Colours encode velocity (in m/s).

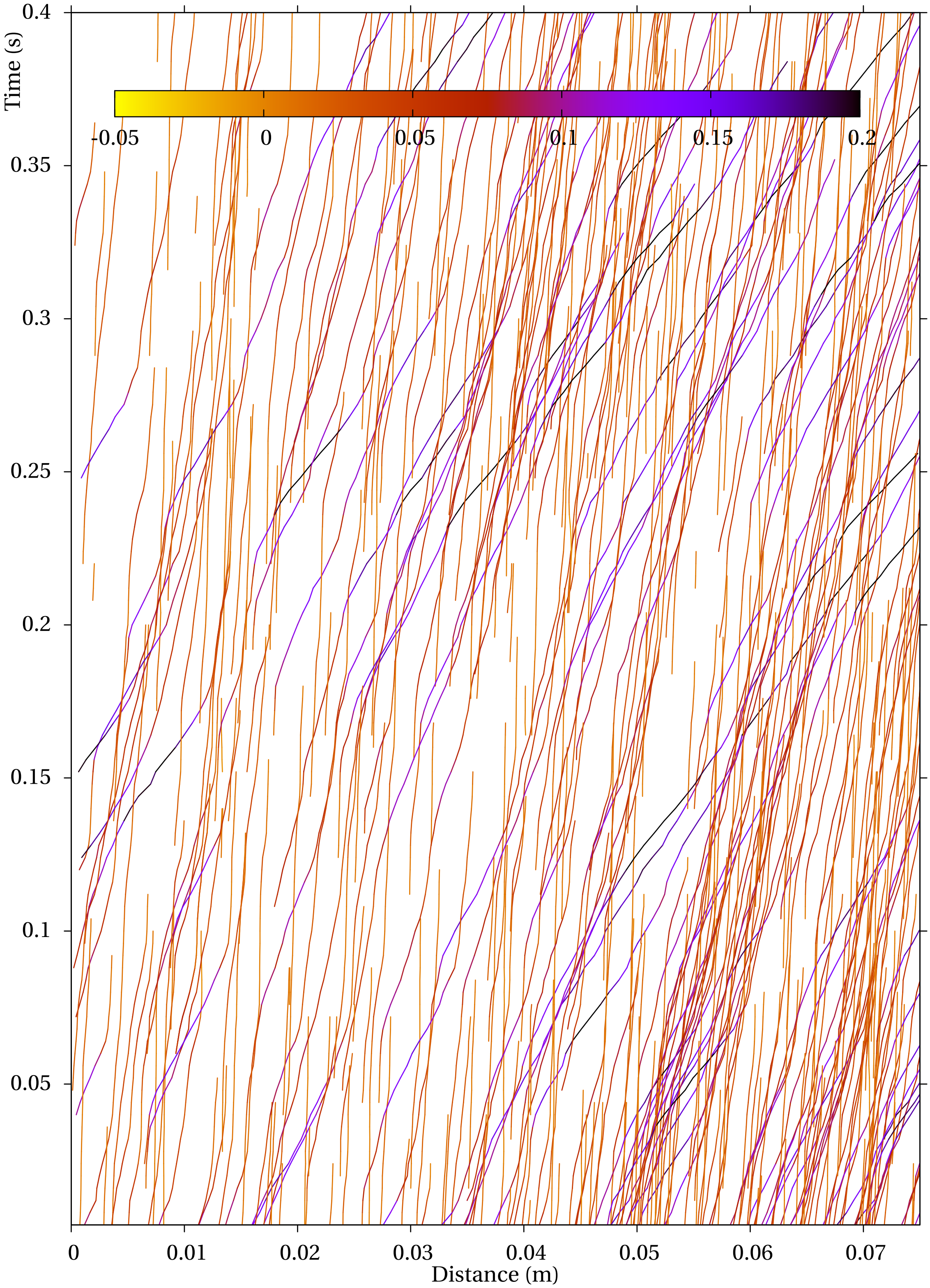

Figure B.7: Particle trajectories in experiment R0-79. Colours encode velocity (in m/s).

B.3 Derivation of the probability function of the inter-arrival time of particles

Let us define

$$F_n(t) = \Pr(T > t, N(t) = n), \tag{B.3.1}$$

where t is the time since the last emigration event. $F_n(t)$ is the probability that $N(t) = n$ and that no emigration event occurred during time t. Thus

$$F(t) = \Pr(T > t) = \sum_{n=0}^{\infty} F_n(x) = \langle F_n(t) \rangle_n\,, \tag{B.3.2}$$

where $\langle \bullet \rangle_n$ represents ensemble averaging over all possible n. I now consider the transition probabilities on the interval $(t, t+\Delta t]$. $F_n(t+\Delta t)$ equals the probability that any other event but no emigration occurs during Δt. For the state $N(t+\Delta t) = 0$, thus:

$$F_0(t+\Delta t) = F_0(t)\left[1 - \lambda' \Delta t\right] + F_1(t)\sigma \Delta t + o(\Delta t). \tag{B.3.3}$$

The first term on the right hand side of Eq. (B.3.3) is the probability that nothing happened during Δt ($\lambda' = \lambda \Delta x + \varepsilon \langle N \rangle$ denotes the (undifferentiated) effect of entrainment and immigration of particles). The second term on the right hand side of Eq. (B.3.3) is the probability that a unique moving particle ($N(t) = 1$) is deposited onto the bed so that $N(t+\Delta t) = 0$. Similarly, for any $n \geq 1$:

$$\begin{aligned} F_n(t+\Delta t) &= F_n(t)\left[1 - (\lambda' + n(\sigma + \mu + \gamma))\Delta t\right] \\ &+ F_{n+1}(t)\sigma(n+1)\Delta t \\ &+ F_{n-1}(t)\left[\lambda' + \mu(n-1)\right]\Delta t \\ &+ o(\Delta t). \end{aligned} \tag{B.3.4}$$

Dividing by Δt and letting $\Delta t \to 0$, we get

$$\frac{\mathrm{d}F_0}{\mathrm{d}t} = -\lambda' F_0(t) + \sigma F_1(t), \tag{B.3.5}$$

$$\frac{\mathrm{d}F_n}{\mathrm{d}t} = -(\lambda' + n(\sigma + \mu + \varepsilon) F_n(t) + \sigma(n+1) F_{n+1}(t) + \left[\lambda' + \mu(n-1)\right] F_{n-1}(t), \quad (n \geq 1) \tag{B.3.6}$$

The initial condition for (B.3.6) reads:

$$F_n(0) = \Pr(T > 0, N(0) = n) = \Pr(N(0) = n). \tag{B.3.7}$$

The random variable $N(0)$ must be understood as: "the state of the Markov process given that an emigration event just occurred", which is the same as

$$\Pr(N(0) = n) = K\varepsilon(n+1)\Pr(N(t) = n+1), \tag{B.3.8}$$

where K is a normalization constant which will be determined later.

Summing all equations in (B.3.6) simplifies the system considerably since almost all terms cancel out. Only the ε terms remain,

$$\sum_{n=0}^{\infty} F_n'(t) = \sum_{n=0}^{\infty} -\varepsilon n F_n(t). \tag{B.3.9}$$

Calling f_T the probability density function of T, (B.3.9) gives the simple relationship

$$f_T(t) = -F'(t) = \varepsilon \left\langle F_n(t) \right\rangle_n . \tag{B.3.10}$$

The general solution of (B.3.6) for all n can be obtained with the help of the generating function

$$G(z,t) = \sum_{n=0}^{\infty} F_n(t) z^n, \tag{B.3.11}$$

with $z \in [0,1]$. Introducing (B.3.11) into (B.3.6) yields the partial differential equation

$$\frac{\partial G}{\partial t} - (\sigma + \mu z^2 - z(\alpha + \mu))\frac{\partial G}{\partial z} = (z-1)\lambda' G, \tag{B.3.12}$$

where the short hand notation $\alpha = \varepsilon + \sigma$ is used. Equation (B.3.12) can be solved with the method of characteristics. The initial condition for (B.3.12) is the generating function corresponding to (B.3.8). The latter is easily obtained by observing that it is the derivative of the steady state generating function of N, given in Ancey *et al.* [2008]:

$$G(z,0) = K\varepsilon \frac{\partial}{\partial z}\left[\left(\frac{\alpha-\mu}{\alpha-\mu z}\right)^{\lambda'/\mu}\right] = \left(\frac{\alpha-\mu}{\alpha-\mu z}\right)^{\lambda'/\mu+1},$$

where K has been replaced to fulfill the normalization condition $G(1,0) = 1$. The solution of Eq. (B.3.12) is

$$G(z,t) = \left[(z_1-z_2)e^{-\mu(1-z_2)t}\right]^{\lambda'/\mu}\left(\frac{\alpha-\mu}{A(t)-B(t)z}\right)^{\lambda'/\mu+1}\left[z_1 - z + e^{-\mu(z_1-z_2)t}(z-z_2)\right], \tag{B.3.13}$$

where $A(t)$, $B(t)$, z_1, and z_2 are

$$\begin{aligned} A(t) &= z_2(\mu z_1-\alpha)e^{-\mu(z_1-z_2)t} + z_1(\alpha-\mu z_2), \\ B(t) &= (\mu z_1-\alpha)e^{-\mu(z_1-z_2)t} + (\alpha-\mu z_2), \\ z_1 &= (\alpha+\mu)\left(1+\sqrt{1-\epsilon}\right)/2\mu, \\ z_2 &= (\alpha+\mu)\left(1-\sqrt{1-\epsilon}\right)/2\mu, \end{aligned} \tag{B.3.14}$$

and $\epsilon = 4\sigma\mu/(\alpha+\mu)^2$. As seen in (B.3.10), the probability density function of T is related to the first moment of F_n. A useful property of generating functions gives

$$\left.\frac{\partial G(z,t)}{\partial z}\right|_{z=1} = \langle F_n(t)\rangle_n, \tag{B.3.15}$$

so that finally for all $t > 0$,

$$\begin{aligned} f_T(t) = \; & \varepsilon(z_1-z_2)^{\lambda'/\mu}\left(\frac{\alpha-\mu}{A(t)-B(t)}\right)^{\lambda'/\mu+1} e^{-\lambda'(1-z_2)t} \times \\ & \left\{\frac{\left(\lambda'/\mu+1\right)B(t)}{A(t)-B(t)}\left[(1-z_2)e^{-\mu(z_1-z_2)t} + z_1 - 1\right] + e^{-\mu(z_1-z_2)t} - 1\right\}, \end{aligned} \tag{B.3.16}$$

where $A(t)$, $B(t)$, z_1 and z_2 have been defined in (B.3.15).

B.4 Spatial fluctuations of the particle activity

We want to compute the integral

$$\mathrm{Var}[N(L,t)] = \int_L \int_L \langle \gamma(x,t), \gamma(x',t) \rangle \,\mathrm{d}x\ \mathrm{d}x'.$$

That is

$$\mathrm{Var}[N(L,t)] = \langle \gamma \rangle_s L + \frac{\langle \gamma \rangle_s}{2\ell_c} \frac{\mu}{\sigma - \mu} \int_{-L/2}^{L/2} \int_{-L/2}^{L/2} \mathrm{e}^{-|x-x'|/\ell_c} \mathrm{d}x\ \mathrm{d}x'.$$

The value of the integral can be obtained by using

$$\begin{aligned} \int_{-L/2}^{L/2} \int_{-L/2}^{L/2} \mathrm{e}^{|x-x'|/\ell_c} \mathrm{d}x\ \mathrm{d}x' &= \int_{-L/2}^{L/2} \left[\int_{-L/2}^{x} \mathrm{e}^{(x-x')/\ell_c} \mathrm{d}x + \int_{x}^{L/2} \mathrm{e}^{-(x-x')/\ell_c} \mathrm{d}x \right] \mathrm{d}x' \\ &= \ell_c \int_{-L/2}^{L/2} \left[2 - \mathrm{e}^{L/(2\ell_c)} \left(\mathrm{e}^{-x'/\ell_c} + \mathrm{e}^{x'/\ell_c} \right) \right] \mathrm{d}x' \\ &= 2\ell_c^2 \left(L/\ell_c + \mathrm{e}^{-L/\ell_c} - 1 \right). \end{aligned}$$

Thus,

$$\mathrm{Var}[N(L,t)] = \langle \gamma \rangle_s L + \langle \gamma \rangle_s \ell_c \frac{\mu}{\sigma - \mu} \left(L/\ell_c + \mathrm{e}^{-L/\ell_c} - 1 \right).$$

Bibliography

Ancey, C. 2010 Stochastic modeling in sediment dynamics: Exner equation for planar bed incipient bed load transport conditions. *J. Geophys. Res.* **115**, F00A11.

Ancey, C., Böhm, T., Jodeau, M. & Frey, P. 2006 Statistical description of sediment transport experiments. *Phys. Rev. E* **74** (1), 011302.

Ancey, C., Davison, A. C., Böhm, T., Jodeau, M. & Frey, P. 2008 Entrainment and motion of coarse particles in a shallow water stream down a steep slope. *J. Fluid Mech.* **595**, 83–114.

Ancey, C. & Heyman, J. 2014 A microstructural approach to bed load transport: mean behaviour and fluctuations of particle transport rates. *J. Fluid Mech.* **744**, 129–168.

Andreotti, B., Claudin, P., Devauchelle, O., Durán, O. & Fourrière, A. 2012 Bedforms in a turbulent stream: ripples, chevrons and antidunes. *J. Fluid Mech.* **690**, 94–128.

Andreotti, B., Claudin, P. & Pouliquen, O. 2010 Measurements of the aeolian sand transport saturation length. *Geomorphology* **123** (3–4), 343–348.

Bagnold, R. A. 1956 The flow of cohesionless grains in fluids. *Phil. Trans. Roy. Soc. A* **249** (964), pp. 235–297.

Bagnold, R. A. 1973 The nature of saltation and of "bed-load" transport in water. *Proc. R. Soc. Lon. Ser. - A* **332** (1591), pp. 473–504.

Balmforth, N.J. & Provenzale, A. 2001 Patterns of dirt. In *Geomorphological Fluid Mechanics* (ed. N. Balmforth & A. Provenzale), *Lecture Notes in Physics*, vol. 582, pp. 369–393. Springer Berlin / Heidelberg.

Balmforth, N.J. & Vakil, A. 2012 Cyclic steps and roll waves in shallow water flow over an erodible bed. *J. Fluid Mech.* **695**, 35–62.

Best, J. 2005 The fluid dynamics of river dunes: A review and some future research directions. *J. Geophys. Res.* **110** (F4), F04S02.

BHAT, U. NARAYAN 2008 *An Introduction to Queueing Theory*, 12th edn. Birkhäuser Basel.

BÖHM, T., ANCEY, C., FREY, P., REBOUD, J.L. & DUCOTTET, C. 2004 Fluctuations of the solid discharge of gravity-driven particle flows in a turbulent stream. *Phys. Rev. E* **69** (6), 061307.

BOUCHAUD, J.-P., CATES, M. E., PRAKASH, J. RAVI & EDWARDS, S. F. 1995 Hysteresis and metastability in a continuum sandpile model. *Phys. Rev. Lett.* **74** (11), 1982–1985.

DU BOYS, P. 1879 Etudes du régime du rhône et de l'action exercée par les eaux sur un lit à fond de graviers indéfiniment affouillable. *Annales des Ponts et Chaussées, Série 5* **18**, 141–195.

BRIDGE, J. S. & BENNETT, S. J. 1992 A model for the entrainment and transport of sediment grains of mixed sizes, shapes, and densities. *Water Resour. Res.* **28** (2), 337–363.

BUNTE, K. & ABT, S. R. 2005 Effect of sampling time on measured gravel bed load transport rates in a coarse-bedded stream. *Water Resour. Res.* **41** (11), W11405.

CAMPAGNOL, J., RADICE, A., NOKES, R., BULANKINA, V., LESCOVA, A. & BALLIO, F. 2013 Lagrangian analysis of bed-load sediment motion: database contribution. *J. Hydraul. Res.* **51** (5), 589–596.

CAO, Z. 1997 Turbulent bursting-based sediment entrainment function. *J. Hydraul. Eng.* **123** (3), 233–236.

CAO, Z., PENDER, G., WALLIS, S. & CARLING, P. 2004 Computational dam-break hydraulics over erodible sediment bed. *J. Hydraul. Eng.* **130** (7), 689–703.

CELIK, A.O., DIPLAS, P., DANCEY, C.L. & VALYRAKIS, M. 2010 Impulse and particle dislodgement under turbulent flow conditions. *Phys. Fluids* **22** (4), 046601.

CHARRU, F. 2006 Selection of the ripple length on a granular bed sheared by a liquid flow. *Phys. Fluids* **18** (12), 121508.

CHARRU, F. & HINCH, E. J. 2006 Ripple formation on a particle bed sheared by a viscous liquid. part 1. steady flow. *J. Fluid Mech.* **550**, 111–121.

CHATURVEDI, S. & GARDINER, C.W. 1978 The poisson representation. ii two-time correlation functions. *J. Stat. Phys.* **18**, 501–522.

COLEMAN, S. E. & NIKORA, V. I. 2009 Exner equation: A continuum approximation of a discrete granular system. *Water Resour. Res.* **45** (9), W09421.

COLEMAN, S. E. & NIKORA, V. I. 2011 Fluvial dunes: initiation, characterization, flow structure. *Earth Surf. Processes* **36** (1), 39–57.

COLOMBINI, M. & STOCCHINO, A. 2008 Finite-amplitude river dunes. *J. Fluid Mech.* **611**, 283–306.

CORDIER, S., LE, M.H. & DE LUNA, T. MORALES 2011 Bedload transport in shallow water models: Why splitting (may) fail, how hyperbolicity (can) help. *Adv. in Water Res.* **34** (8), 980 – 989.

COX, D. R. & ISHAM, V. 1980 *Point Processes*. Chapman & Hall, London.

COX, J., INGERSOLL, J. & ROSS, S. 1985 A theory of the term structure of interest rates. *Econometrica* **53** (2), 385–407.

DETERT, M., WEITBRECHT, V & JIRKA, G.H. 2010 Laboratory measurements on turbulent pressure fluctuations in and above gravel beds. *J. Hydraul. Eng.* **136** (10), 779–789.

DINEHART, R. L. 1999 Correlative velocity fluctuations over a gravel river bed. *Water Resour. Res.* **35** (2), 569–582.

DRAKE, T. G., SHREVE, R. L., DIETRICH, W. E., WHITING, P. J. & LEOPOLD, L. B. 1988 Bedload transport of fine gravel observed by motion-picture photography. *J. Fluid Mech.* **192**, 193–217.

DWIVEDI, A., MELVILLE, B.W., SHAMSELDIN, A.Y. & GUHA, T.K. 2011 Analysis of hydrodynamic lift on a bed sediment particle. *J. Geophys. Res.* **116** (F2), F02015.

EINSTEIN, A. 1906 Zur theorie der brownschen bewegung. *Ann. Phys.* **19**, 371–381.

EINSTEIN, H. A. 1937 *Der Geschiebetrieb als Wahrscheinlichkeitproblem (Bedload transport as a probability problem)*. English translation by W.W. Sayre, in Sedimentation, Ed. H.W. Shen, Fort Collins, Colorado, 1972, C1–C105, ETHZ.

EINSTEIN, H. A. 1950 *The bed-load function for sediment transportation in open channel flows*. U.S. Dept. of Agriculture, Washington, D. C.

ETTEMA, R. & MUTEL, C. 2004 Hans Albert Einstein: Innovation and compromise in formulating sediment transport by rivers. *J. Hydraul. Eng.* **130** (6), 477–487.

FAN, N., ZHONG, D., WU, B., FOUFOULA-GEORGIOU, E. & GUALA, M. 2014 A mechanistic-stochastic formulation of bed load particle motions: from individual particle forces to the fokker-planck equation under low transport rates. *J. Geophys. Res.-earth* **119**, in press.

FELLER, W. 1951 Two singular diffusion problems. *Ann. Math* **54** (1), pp. 173–182.

FERGUSON, R. 2007 Flow resistance equations for gravel- and boulder-bed streams. *Water Resour. Res.* **43** (5), W05427.

FERGUSON, R. 2012 River channel slope, flow resistance, and gravel entrainment thresholds. *Water Resour. Res.* **48** (5), W05517.

FREDSOE, J. 2012 Sediment transport. In *Handbook of Environmental Fluid Dynamics, Volume One*. CRC Press.

FREY, P. & CHURCH, M. 2009 How river beds move. *Science* **325** (5947), 1509–1510.

FURBISH, D.J., HAFF, P.K., ROSEBERRY, J.C. & SCHMEECKLE, M.W. 2012*a* A probabilistic description of the bed load sediment flux: 1. theory. *J. Geophys. Res.-earth* **117** (F3), F03031.

FURBISH, D.J., ROSEBERRY, J.C. & SCHMEECKLE, M.W. 2012*b* A probabilistic description of the bed load sediment flux: 3. the particle velocity distribution and the diffusive flux. *J. Geophys. Res.-earth* **117** (F3), F03033.

GARDINER, C.W. 2002 *Handbook of Stochastic Methods : for Physics, Chemistry and the Nnatural Sciences*. Springer.

GARDINER, C.W. & CHATURVEDI, S. 1977 The Poisson representation. I. a new technique for chemical master equations. *J. Stat. Phys.* **17**, 429–468.

GILLESPIE, D.T. 1977 Exact stochastic simulation of coupled chemical reactions. *J. Phys. Chem.* **81** (25), 2340–2361.

GILLESPIE, D.T. 1991 *Markov Processes: An Introduction for Physical Scientists*. Academic Press.

GOLDSTEIN, S. 1951 On diffusion by discontinuous movements and the telegraph equation. *The Quarterly Journal of Mechanics and Applied Mathematics* **4** (2), 129–156.

GRAF, W.H. & ALTINAKAR, S. 2005 *Transport of Sediments (in Encyclopedia of Hydrological Science)*. New York: John Wiley & Sons.

GRAF, W. H. 1971 *Hydraulics of Sediment Transport*. McGraw-Hill.

HAMAMORI, A. 1962 *A Theoretical Investigation on the Fluctuation of Bed-load Transport*. Delft Hydraul. Lab., Delft, Netherlands.

HERCZYNSKI, R. & PIENKOWSKA, I. 1980 Toward a statistical theory of suspension. *Ann. Rev. Fluid Mech.* **12** (1), 237–269.

HEYMAN, J., MA, H.B., METTRA, F. & ANCEY, C. 2014 Spatial correlations in bed load transport: evidence, importance, and modelling. *J. Geophys. Res.* **submitted**.

HEYMAN, J., METTRA, F., MA, H. B. & ANCEY, C. 2013 Statistics of bedload transport over steep slopes: Separation of time scales and collective motion. *Geophys. Res. Lett.* **40(1)**, 128–133.

HIGHAM, D. J. 2008 Modeling and simulating chemical reactions. *SIAM Rev.* **50** (2), 347–368.

HILL, K. M., DELLANGELO, L. & MEERSCHAERT, MARK M. 2010 Heavy-tailed travel distance in gravel bed transport: An exploratory enquiry. *J. Geophys. Res.* **115**, F00A14.

HOEY, T. 1992 Temporal variations in bedload transport rates and sediment storage in gravel-bed rivers. *Prog. Phys. Geog.* **16** (3), 319–338.

IACUS, S.M. 2008 *Simulation and Inference for Stochastic Differential Equations*. New York: Springer.

JEROLMACK, D. J. & MOHRIG, D. 2005 A unified model for subaqueous bed form dynamics. *Water Resour. Res.* **41** (12), W12421.

JOSEPH, G. G., ZENIT, R., HUNT, M. L. & ROSENWINKEL, A. M. 2001 Particle-wall collisions in a viscous fluid. *J. Fluid Mech.* **433**, 329–346.

KATUL, G., WIBERG, P., ALBERTSON, J. & HORNBERGER, G. 2002 A mixing layer theory for flow resistance in shallow streams. *Water Resour. Res.* **38** (11), 1250.

KIESGEN DE RICHTER, S., LE CAËR, G. & DELANNAY, R. 2012 Dynamics of rearrangements during inclination of granular packings: the avalanche precursor regime. *J. Stat. Mech.-theory E.* **2012** (04), P04013.

KLEINHANS, M. & VAN RIJN, L. 2002 Stochastic prediction of sediment transport in sand-gravel bed rivers. *J. Hydraul. Eng.* **128** (4), 412–425.

KLOEDEN, P. E. & PLATEN, E. 2011 *Numerical Solution of Stochastic Differential Equations*. New York: Springer.

KNIGHT, D.W. 1981 Boundary shear in smooth and rough channels. *J Hydraul Div* **107** (7), 839–851.

KUHN, H. W. 1955 The Hungarian method for the assignment problem. *Naval Research Logistics Quarterly* **2** (1-2), 83–97.

KUHNLE, R.A. & SOUTHARD, J.B. 1988 Bed load transport fluctuations in a gravel bed laboratory channel. *Water Resour. Res.* **24** (2), 247–260.

LAJEUNESSE, E., MALVERTI, L. & CHARRU, F. 2010 Bed load transport in turbulent flow at the grain scale: Experiments and modeling. *J. Geophys. Res.* **115** (F4), F04001.

LEGENDRE, D., DANIEL, C. & GUIRAUD, P. 2005 Experimental study of a drop bouncing on a wall in a liquid. *Phys. Fluids* **17** (9), 097105.

LOISELEUX, T., GONDRET, P., RABAUD, M. & DOPPLER, D. 2005 Onset of erosion and avalanche for an inclined granular bed sheared by a continuous laminar flow. *Phys. Fluids* **17** (10), 103304.

MARTIN, R., JEROLMACK, D. J. & SCHUMER, R. 2012 The physical basis for anomalous diffusion in bed load transport. *J. Geophys. Res.-earth* **117** (F1), F01018.

MEYER-PETER, E. & MULLER, R. 1948 Formulas for bed-load transport. *Proceedings of the International Association for Hydraulic Research, ThirdAnnual Conference, Stockholm, Sweden.* pp. 39–64.

MOIN, P. 2009 Revisiting Taylor's hypothesis. *J. Fluid Mech.* **640**, 1–4.

MORVAN, H., KNIGHT, D., WRIGHT, N., TANG, X. & CROSSLEY, A. 2008 The concept of roughness in fluvial hydraulics and its formulation in 1D, 2D and 3D numerical simulation models. *J. Hydraul. Res.* **46** (2), 191–208.

MÜLLER, J. & HILLEN, T. 1998 Modulation equations and parabolic limits of reaction random-walk systems. *Math Method Appl Sci* **21** (13), 1207–1226.

NICOLIS, G. & PRIGOGINE, I. 1977 *Self-Organization in Nonequilibrium Systems: From Dissipative Structures to Order through Fluctuations*, 1st edn. Wiley.

NIKORA, V., HABERSACK, H., HUBER, T. & MCEWAN, I. 2002 On bed particle diffusion in gravel bed flows under weak bed load transport. *Water Resour. Res.* **38** (6), 1081.

NITSCHE, M., RICKENMANN, D., TUROWSKI, J. M., BADOUX, A. & KIRCHNER, J. W. 2011 Evaluation of bedload transport predictions using flow resistance equations to account for macro-roughness in steep mountain streams. *Water Resour. Res.* **47** (8), W08513.

OTHMER, H.G., DUNBAR, S.R. & ALT, W. 1988 Models of dispersal in biological systems. *J Math Biol* **26** (3), 263–298.

PAPANICOLAOU, A. N., DIPLAS, P., EVAGGELOPOULOS, N. & FOTOPOULOS, S. 2002 Stochastic incipient motion criterion for spheres under various bed packing conditions. *J. Hydraul. Eng.* **128** (4), 369–380.

PARKER, G. 1975 Sediment inertia as cause of river antidunes. *J. Hydraul. Div.* **101** (2), 211–221.

PARKER, G., PAOLA, C. & LECLAIR, S. 2000 Probabilistic exner sediment continuity equation for mixtures with no active layer. *J. Hydraul. Eng.* **126** (11), 818–826.

QUARTIER, L., ANDREOTTI, B., DOUADY, S. & DAERR, A. 2000 Dynamics of a grain on a sandpile model. *Phys. Rev. E* **62**, 8299–8307.

RADICE, ALESSIO, BALLIO, FRANCESCO & NIKORA, VLADIMIR 2010 Statistics and characteristic scales for bed load in a channel flow with sidewall effects. *Acta Geophys* **58** (6), 1072–1093.

RADICE, A., MALAVASI, S. & BALLIO, F. 2006 Solid transport measurements through image processing. *Exp Fluids* **41** (5), 721–734.

RADICE, A., NIKORA, V., CAMPAGNOL, J. & BALLIO, F. 2013 Active interactions between turbulence and bed load: Conceptual picture and experimental evidence. *Water Resour. Res.* **49** (1), 90–99.

RECKING, A., LIÉBAULT, F., PETEUIL, C. & JOLIMET, T. 2012 Testing bedload transport equations with consideration of time scales. *Earth Surf. Processes* **37** (7), 774–789.

RICKENMANN, DIETER, TUROWSKI, JENS M., FRITSCHI, BRUNO, KLAIBER, ANGELA & LUDWIG, ANDREAS 2012 Bedload transport measurements at the Erlenbach stream with geophones and automated basket samplers. *Earth Surf. Processes* **37** (9), 1000–1011.

RIGUIDEL, F.X., JULLIEN, R., RISTOW, G.H., HANSEN, A. & BIDEAU, D. 1994 Behaviour of a sphere on a rough inclined plane. *J. Phys. I France* **4** (2), 261–272.

RIPLEY, B.D. 1976 The second order analysis of stationary point processes. *J. Appl. Probab.* **13**, 255–266.

ROSEBERRY, J.C., SCHMEECKLE, M.W. & FURBISH, D.J. 2012 A probabilistic description of the bed load sediment flux: 2. particle activity and motions. *J. Geophys. Res.-earth* **117** (F3), F03032.

ROSS, S.M. 2006 *Introduction to Probability Models, Ninth Edition*. Orlando, FL, USA: Academic Press, Inc.

SACERDOTE, L. 1990 On the solution of the Fokker-Planck equation for a Feller process. *Adv. Appl. Probab.* **22** (1), pp. 101–110.

SCHMEECKLE, M.W., NELSON, J.M., PITLICK, J. & BENNETT, J.P. 2001 Interparticle collision of natural sediment grains in water. *Water Resour. Res.* **37** (9), 2377–2391.

SCHMEECKLE, M.W., NELSON, J. M. & SHREVE, R.L. 2007 Forces on stationary particles in near-bed turbulent flows. *J. Geophys. Res.-earth* **112** (F2), F02003.

SEIZILLES, G., LAJEUNESSE, E., DEVAUCHELLE, O. & BAK, M. 2014 Cross-stream diffusion in bedload transport. *Phys. Fluids* **26** (1), 013302.

SEKINE, M. & KIKKAWA, H. 1992 Mechanics of saltating grains. ii **118** (4), 536–558.

SHIELDS, A. 1936 Anwendung der aehnlichkeitsmechanik und der turbulenzforschung auf die geschiebebewegung. *Mitteilungen der Preußischen Versuchsanstalt für Wasserbau, Berlin* **26**.

SINGH, A., FIENBERG, K., JEROLMACK, D. J., MARR, J. & FOUFOULA-GEORGIOU, E. 2009 Experimental evidence for statistical scaling and intermittency in sediment transport rates. *J. Geophys. Res.* **114** (F1), F01025.

STARON, L., RADJAI, F. & VILOTTE, J.P. 2006 Granular micro-structure and avalanche precursors. *J. Stat. Mech.-theory E.* **2006** (07), P07014.

SUN, Z. & DONAHUE, J. 2000 Statistically derived bedload formula for any fraction of nonuniform sediment. *J. Hydraul. Eng.* **126** (2), 105–111.

TUROWSKI, J. M. 2010 Probability distributions of bed load transport rates: A new derivation and comparison with field data. *Water Resour. Res.* **46** (8), W08501.

UHLENBECK, G. E. & ORNSTEIN, L. S. 1930 On the theory of the Brownian motion. *Phys. Rev.* **36**, 823–841.

VALYRAKIS, M., DIPLAS, P. & DANCEY, C.L. 2011 Entrainment of coarse grains in turbulent flows: An extreme value theory approach. *Water Resour. Res.* **47** (9), W09512.

VALYRAKIS, M., DIPLAS, P., DANCEY, C.L., GREER, K. & CELIK, A.O. 2010 Role of instantaneous force magnitude and duration on particle entrainment. *J. Geophys. Res.* **115** (F2), F02006.

VAN PROOIJEN, B. C. & WINTERWERP, J. C. 2010 A stochastic formulation for erosion of cohesive sediments. *Journal of Geophysical Research: Oceans* **115** (C1), C01005.

WU, F. & CHOU, Y. 2003 Rolling and lifting probabilities for sediment entrainment. *J. Hydraul. Eng.* **129** (2), 110–119.

WU, F.C. & YANG, K.H. 2004 A stochastic partial transport model for mixed-size sediment: Application to assessment of fractional mobility. *Water Resour. Res.* **40** (4), W04501.

YILMAZ, A., JAVED, O. & SHAH, M. 2006 Object tracking: A survey. *ACM Comput. Surv.* **38** (4).

Avenue de France, 20
1004 Lausanne (Switzerland)
Tél : +41 (0)77 474 49 40
Mail : joris.heyman@epfl.ch

Né le 03 août 1987 (26 ans)
Nationalité française

Joris HEYMAN

Education

2005	BACCALAURÉAT SÉRIE S (OPTION MATHÉMATHIQUES), MENTION TB. ▷ *Lycée Île de France, Rennes (35).*
2005-2010 (5 ans)	INGÉNIEUR GÉNIE CIVIL. (INSTITUT NATIONAL DES SCIENCES APPLIQUÉES, INSA RENNES). ▷ *Mécanique (sol, solide, fluide), résistance des matériaux, thermo-mécanique.*
2009 (1 ans)	M1 BUDAPEST UNIVERSITY OF TECHNOLOGY AND ECONOMICS (BME, HONGRIE). ▷ *Mechanics and dynamics, differential equations, analytical mechanics.* ▷ *Bourse EGIDE études/recherche.*
2010 (1 ans)	MASTER 2 (MSC) RECHERCHE, MÉCANIQUE (INSA/UNIVERSITÉ DE RENNES 1). ▷ *Elasticité non-linéaire, écoulement turbulents, méthodes numériques, rhéologie.*
2011- (4 ans)	ECOLE POLYTECHNIQUE FÉDÉRALE DE LAUSANNE (EPFL), SWITZERLAND, LABORATOIRE D'HYDRAULIQUE ENVIRONNEMENTALE. THÈSE DE DOCTORAT (PHD). ▷ *Modèles probabilistiques pour le transport de sédiment par charriage.*

Expèriences

2006 (2 mois)	LABORATOIRE VERRES ET CÉRAMIQUES (RENNES 1). STAGE L1.. Fibres optiques de verres de calcogénures transmettant dans l'infra-rouge
2007 (2 mois)	INTÉRIMAIRE CHEZ TNT. Tri postal nocturne.
2008 (3 mois)	LABORATOIRE DE MÉCANIQUE DES SOLS DE L'ÉCOLE CENTRALE (NANTES). STAGE L3.. Analyse inverse des essais triaxiaux de sols par algorithmes génétiques
2009 (3 mois)	SOGREAH (NANTES). STAGE M1. Effet du ralentissement dynamique des crues sur l'Oust et la Vilaine, Modélisation hydrologique HEC-HMS
2010 (3 mois)	LABORATOIRE D'INGÉNIERIE DES MATÉRIAUX DE BRETAGNE (UNIVERSITÉ BRETAGNE SUD). STAGE M2 RECHERCHE. Méthodes asymptotiques numériques pour la recherche de point de bifurcation dans les écoulements fluides
2010-	TÂCHES D'ENSEIGNEMENT (20%). Enseignement de mécanique des fluides, gestion des risques hydrologiques ainsi que hydraulique des crues et ruptures de barrage

Outils numériques

Programation	Très bonne maitrise des languages Matlab, Mathematica, Python, Fortran, C++, Unix, Latex, et autres pingouins..

Langues

Anglais	Fluent, TOEIC 2010 960/995. Bases d'allemand et de russe

Publications

2014	Ancey, C. & Heyman, J. *A microstructural approach to bed load transport : mean behaviour and fluctuations of particle transport rates*, J. Fluid Mech., 2014, **744**, 129–168
2013	Heyman, J. ; Mettra, F. ; Ma, H. B. & Ancey, C. *Statistics of bedload transport over steep slopes : Separation of time scales and collective motion*, Geophys. Res. Lett., 2013, **40(1)**, 128–133
2013	Heyman, J. ; Girault,G. ; Guevel, Y. ; Allery, C. ; Hamdouni, A. & Cadou, J.M., *Computation of Hopf bifurcations coupling reduced order models and the Asymptotic Numerical Method*, Computers & Fluids, 2013, **76**, 73–85